UNIVERSITÀ DI SIENA 1240

Department of Physical Sciences, Earth and Environment

PhD in Experimental Physics

XXXIII Cycle

Coordinator: Prof. Riccardo Paoletti

Search for signal from self-annihilation of Dark Matter particles from the globular cluster M15 through MAGIC observations

Disciplinary Scientific Sector: FIS/01

PhD Student:	Supervisor:
Lorenzo Bellizzi	Dr. Giacomo Bonnoli
Digitally signed by BELLIZZI LORENZO C=IT	Tutor:
	Prof. Riccardo Paoletti

2019/2020

Abstract

Physics can explain a lot of natural phenomena from the infinitely small to the infinitely large. But despite all our progresses, the phenomena we are able to explain consider the matter we know, made up of atoms and described by a theory called *standard model* (*SM*). From state-of-the-art cosmological measurements, we know that this known matter represents only $\sim 5\%$ of the whole energy budget of the Universe while the remaining $\sim 95\%$ is still unknown because we can not see it: we call this amount *dark universe.* The dark universe is widely considered to be split into two components: the first is *dark energy* (DE) and represents $\sim 70\%$ of the Universe, the second is *dark matter* (DM) and represent $\sim 25\%$ of the total energy budget.

The existence of dark matter is indirectly confirmed by observational data and theoretical predicted within N-body cosmological simulations: without dark matter we can not explain the structure and the evolution of the Universe.

One of the best candidates for DM is the class of particles called *Weakly Interacting Massive Particles (WIMPs).* This class includes massive particles with an expected mass range between few GeV and few hundreds of TeV. WIMPs are expected to interact with the baryonic matter through gravitation and weak nuclear force, and are stable or unstable but with decay time scale of the order of the Hubble time.

WIMPs can annihilate and decay producing particles of the standard model like electron-positron pairs, neutrinos and $\gamma-$rays. One of the ways to investigate DM is the indirect search signals produced by DM annihilation or decay. Neutrinos and photons travel along straight paths from the source to the Earth, preserving information about the source. $\gamma-$rays which are produced by DM particles can bring energies higher than 100 GeV. This range of energy is called *Very High Energy (VHE)* $\gamma-$ray and the photons with this feature can be detected by ground based telescopes through Cherenkov light emitted by charged particles which are produced when a $\gamma-$ray interact with the atoms of the atmosphere producing an electromagnetic shower.

In this PhD thesis I investigate on the presence of dark matter inside a peculiar globular cluster (GC), M15 (also known NGC 7078), analysing the

data collected by the MAGIC telescopes along 2015 and 2016 for a total of $\sim$ 170 hours of integrated observation. M15 is one of the oldest object of the galaxy, located at 10.4 kpc from Earth and shows a very compact core, consequence of an initial phase of core collapse. It is likely that during this early phase the dark matter budget of M15 was concentrated inside the core. M15 is also one of the most studied GC of the Milk Way and from observations of star velocities we know that the center of the GC has to be dominated by massive dark objects, like stellar remnants, or dark matter or some their combination [1]. Unfortunately we know the profiles of the total density of the cluster and the mass to light ratio (M/L) in the inner part but we do not know the relative amount of dark objects in the core. Some studies on other globular clusters (Tuc47, $\omega-$Cen and NGC 6266) take in consideration some combination between dark matter and dark objects to explain the flux and the expected flux at VHE $\gamma-$ray [2, 3].

First Whipple telescope and later the High Energy Stereoscopic System (H.E.S.S.) have studied M15 in the VHE $\gamma-$ray range but the instruments did not find any signal attributable to annihilating dark matter particles.

The MAGIC telescopes observed M15 in search for a VHE $\gamma-$rays excess due to pulsars. Data were collected for 173 hours and no significant excess was found. This same data set was then used in this work for a dark matter search in correlation with the new measurements on the density profile and mass to luminosity ratio in the inner parts of M15.

The expected signal is given by the astrophysical factor, *J-factor*, and the spectrum of particles emitted from annihilation. The spectrum depends by the annihilation model and I have chosen 100% branching ratio into different SM particle pairs. J-factor describes the dark matter distribution inside the source and I derived its value from optical measurements of the star velocities. An important contribution of this thesis was to provide a method for computing the uncertainty of the J-factor, based on Monte Carlo techniques.

As a mere starting point, I assumed that all the missing matter was made up of dark matter. Obviously such as assumption, leads easily to unrealistic limits. The actual contribution of dark matter component to the missing mass depends on the model assumed, and should be better constrained with further work. Tentatively, I computed upper limits under the assumption that the amount of dark matter is a tiny percentage of the entire missing matter inside the core. A realistic evaluation of the amount of dark matter requires the construction of models which must take into consideration different processes that may have occurred during the evolution of the cluster.

No significant excess γ-ray signal from annihilating particles was found in the MAGIC data set. I computed the upper limits on the cross-section as a function of several particles masses and for different channels of annihilation ($b\bar{b}$, $\tau^+\tau^-$, $\mu^+\mu^-$ and W^+W^-).

Assuming that the DM represents only 1% of the the total missing matter inside M15, applying the full likelihood (FL) method on the dataset, with an astrophysical factor $J_{ann} = 4.3 \times 10^{19}$ GeV^2 cm^{-5}, the upper limits for each channel are: $\langle \sigma v \rangle_{b\bar{b}} = 3.07 \times 10^{-24}$ cm^3 s^{-1}, $\langle \sigma v \rangle_{\tau^+\tau^-} = 4.62 \times 10^{-25}$ cm^3 s^{-1}, $\langle \sigma v \rangle_{\mu^+\mu^-} = 1.82 \times 10^{-24}$ cm^3 s^{-1}, $\langle \sigma v \rangle_{W^+W^-} = 1.70 \times 10^{-24}$ cm^3 s^{-1}.

The results have the same order of magnitude of other upper limits which were computed during the observation of dwarf galaxies by MAGIC Telescopes [4, 5, 6, 7] and are few lower than limit of H.E.S.S. which is $\sim 5 \times 10^{-24}$ cm^3 s^{-1} for WIMPs with mass equal to 2 TeV.

The work is structured in six chapters. In chapter 1 a brief introduction on dark matter is given: why its presence is necessary to explain observational data, some clues on its role in the evolution of the Universe, and possible particle candidates for DM. The GC features, the environment where these are created and their evolution are described in the chapter 2 with a special consideration on M15. In chapter 3 are described both the general spectrum of the photons and the relative sources, in particular it is shown by which process DM can produce photons and the expected flux on the Earth, and the technique called *Imaging Air Cherenkov technique (IACT)* used to observe very high energy $\gamma-$rays and search for signals. chapter 4 focuses on the main features of *Major Atmospheric Gamma Imaging Cherenkov (MAGIC)* telescopes and both the standard and DM analysis. The chapter 5 is opened with a brief section dedicated to the method used by the Whipple and H.E.S.S. teams to compute the amount of dark matter inside the cluster from data collected with IACTs. Their studies are the precursors of current work. This is then illustrated, step by step: first the estimate of the J-factor from new measurements and the associated error, then the FL method and the estimate of the 95% CL upper limits on thermally-averaged cross-section $\langle \sigma v \rangle_{ann}$ are shown. Eventually the results will be commented in chapter 6 where future developments are shown on new models of distribution of DM inside the cluster, needed to improve the study on DM in M15.

Contents

Chapter 1

Dark Matter

Dark matter (DM) is a kind of non-baryonic matter permeating the Universe; from last estimates it amounts to $\geq 85\%$ of the matter inside the Universe and $\sim 25\%$ of the total energy of the Universe [8]. In this chapter I will give an introduction to the DM concept and the possible particles candidates.

1.1 Why Dark Matter

In the last century astrophysicists have tried to understand the laws that rule the Universe as a whole. At the same time nuclear physicists have tried to understand the laws ruling the infinitely small universe in order to write a law describing all the particles and fields.

Nowadays dark matter research is an important goal for the physicist because its discovery opened a door on the unknown physics. In one hand it is important to explain the data collected by the observation of the Universe, in the other hand it is important to find the answers on the questions arisen from the nuclear physics. As we will see in the next section, the *standard model* (SM) is not sufficient to explain the features of the particles and their interactions: in this context a theory of dark matter particles could be derived by a more complete nuclear theory including both SM and some exotic particles like DM particle. For this reason the dark matter is investigated in three main ways:

- **indirect detection**: inside clusters of galaxies, around galaxies themselves and inside other bodies, there are high quantities of dark matter. Some theories predict that the particles of dark matter can annihilate themselves or decay in other particles that we know and can detect. This method is called *indirect detection* because only the secondary particles are detected and from their information we can reconstruct the initial scattering [9];

- **direct detection**: this approach tries to measure the recoil energy when one particle of dark matter interacts with an atomic nucleus of the detector: the energy released is very low and produces a weak signal. It is necessary to reduce the noise, especially the noise generated by the interaction of deep baryonic particles. For this reason the experiments are located underground and covered by thick shield capable of stopping the most penetrating particles produced by cosmic rays [10];

- **production in the collider**: the last method to look for DM relies on producing it inside the collider. DM particles could be created in a collider whose luminosity and center-of-mass energy are sufficiently large. In colliders like the LHC [11] very high energetic beams of protons are scattered and a lot of particles are produced. The particles are recorded by the detectors around the point of the impact. Neutrinos escape all the detectors, without being identified by any of them. Therefore, they look like missing momentum: the sum of the transverse momenta of detected particles in the event is not zero if a neutrino is produced. DM particles would be invisible as well inside the detector so one their signal has to be looked for in two ways. The first is called mono-X searches where dark matter mediator is produced by the annihilation of a pair of quarks or gluons and then decays to a pair of WIMPs, which escapes the experimental device undetected. In this case we should see an imbalance in the momentum measured a missing transverse momentum ($\not{p}_T$). The second method is called mediator searches and in this case a dark matter mediator decays to a pair of quarks or leptons, producing a localized excess of events in the invariant mass spectrum or in specifically chosen angular distributions [12, 13].

The three methods, which are described above, can be summarized as in figure 1.1: the physical process observed by a method is described by the scatter plot according to the direction in which the graph is read.

1.2 The brief history of the DM

The term *dark matter* was coined by Fritz Zwicky during a study of Coma cluster [14] in 1933. From the measurement of the velocity of eight galaxies inside the Coma cluster, Zwicky computed that the mean density is 400 times greater

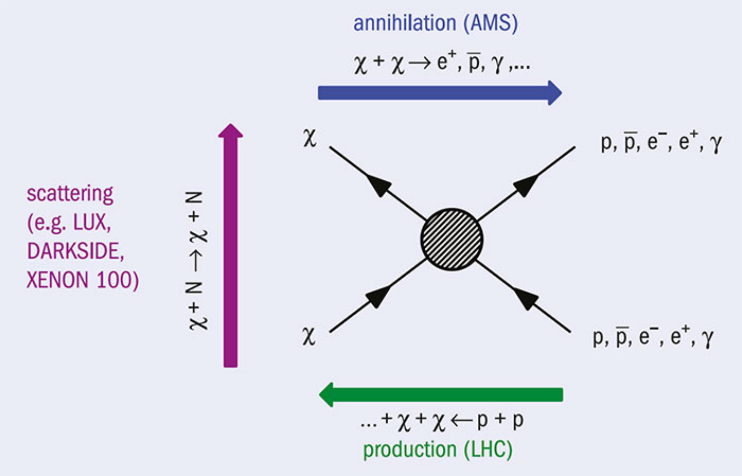

Figure 1.1: The plot shows the three several methods in an unique scattering plots. From right to left the plot describes the production of DM inside the colliders; from bottom to top it is described the *direct methods* where one DM particle scatters with one particle of the SM; from left to right is described the annihilation of DM particles into SM particles.

than that which is derived from luminous matter. He called this unknown mass with the name ***dark matter***. Three years later, another astronomer, Smith, discovered that also Virgo cluster showed the same problem: the total mass had to be greater than the luminosity mass [15]. Zwicky thought that the missing matter was in form of cold macroscopic and microscopic solid bodies like black holes and planets, and gases.

In 1939 Horace Babcock presented the rotation curve of the Galaxy M31 in his PhD thesis. He found very high values for the tangential velocity at large radii. Theoretically the velocity of rotation of a star should go down following the Keplerian motion which is $\propto r^{-1/2}$. Instead Babcock showed that the velocity of the stars was constant at each distance from the center. In figure **??** we can see the incoherence between the data and the theory. Later studies, confermed the Babcock's results.

In 1951 the 21 cm line from the spontaneous emission by the neutral hydrogen was detected in M31. This discover was very important because made possible to extend the study of galaxy rotation, beyond the optical disk. These observations clearly showed that the rotation curve of M 31 did not exhibit a Keplerian drop-off. In fact, its rotational velocity remained constant over radial distances of 16 - 30 Kpc [17, 18].

Another point of view was given by the cosmology branch. Its development imposed important limits on the nature and the amount of the dark matter in

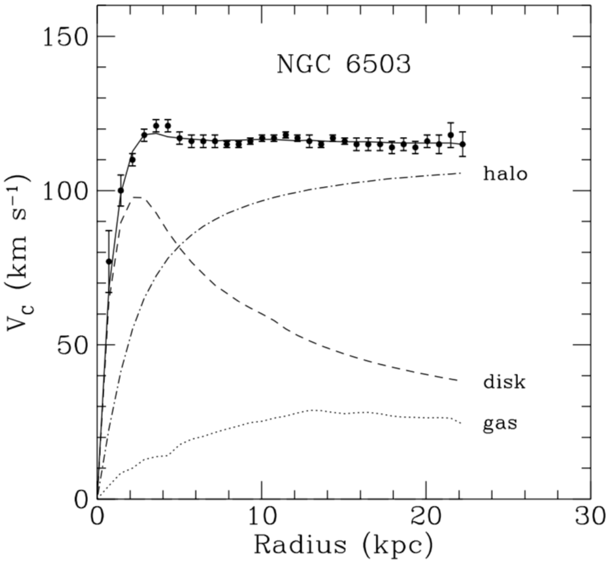

Figure 1.2: Rotation curve of NGC 6503. The different lines show the rotation curves for each component: the dotted line represent the gas, dashed is the disk and dash-dotted lines is dark matter component [16].

the universe. Inside it two different fields are joint: astrophysics and physics of the particles, concerned with the very largest and the very smallest constituents of our universe respectively.

Zeldovich was one of the first nuclear physicist who connected the particle physics with the problems of the cosmology. In the early 1960s Zeldovich and Gershetein computed the mass of the ν_e and ν_μ from the newly discovered *Cosmic Microwave Background (CMB)* [19]. It was the first step towards connecting particle physics, cosmology and astronomy.

In the following decade, 1980s years, numerical simulations were the new tool which could be used to predict how large numbers of DM particles would evolve gravitationally in an expanding Universe. In this way it was easy to see the impact of the dark matter on the formation of large scale structure. Simulations allowed to observe that a dark matter composed by non relativistic particles could form the structures of the Universe in agreement with the observation through a "bottom-up" scenario.

At the end of the 1980s, the conclusion that most of the mass in Universe consists of cold and non baryonic particles was accepted by many astrophysicists and even particle physicists, but this meant extending the standard model with the introduction of new particles.

The ***sterile neutrino***, which was introduced to integrate the neutrino family in the standard model, could be a kind of particle constituting the dark matter. Simon White, Carlos Frenk and Marc Davis [20] showed that neutrino could not provide an explanation for the missing mass of the Universe and in 1993 Scott Dodelson and Widrow proposed a simple scenario with other different neutrino species interacting only via gravity and extending the standard model [21].

A part from the neutrino, in the 1970s many physicist began to search the new symmetries relating fermions to bosons. ***Supersymmetry*** connects every fermion with a boson and vice versa, and predicts the existence of several new new electrically neutral and non-strongly interacting particles. *Gravitino* [22], *neutralino* [23, 24] are some particles that are good candidates as constituents of dark matter.

At the same time that the supersymmetry was born, particle physicists observed one problem called charge-parity (CP) violation. To explain this phenomenon, Roberto Peccei and Helen Quinn proposed a solution introducing a new global U(1) symmetry that is spontaneously broken [25]. Each spontaneous global symmetry breaking corresponds to the existence of a Nambu-Goldstone boson. In this case the boson is called ***axion***. The theory was born in another search field, which is far from the cosmology, but axions could constitute the dark matter because they have all the required features: are stable over cosmological timescales and can be cold dark matter particles.

1.3 Evidence for Dark Matter

Many Observations made in the last century show inconsistencies with the physical laws that we know. We find these incompatible data at different scales: from galactic to cosmological distance. Moreover the presence of dark matter is necessary to match the evolution of the Universe with the observational data. One parameter is the *Mass to Light ratio* (M/L) which indicates the ratio between the mass contained in a volume (typically on the scales of a galaxy or a cluster) and the emitted brightness. The ratio is computed using two independents values: the mass M comes from the study of dynamics, using gravitational lens or *virial theorem*, while the luminosity L comes from the measurement of the radiation produced by the components inside the volume. So, the M/L ratio is a proxy of the relative distribution of dark (invisible) mass to the standard, visible one.

1.3.1 Dark matter in the Solar System neighborhood

It is important to know the M/L in the region close to the Sun, where high precision observations are possible. All the experiment which use the direct detection (e.g. XENON1T, CRESST or PICO-60) are interested to know the density of dark matter around the Earth and also the experiments searching signals from the Sun. The Solar neighborhood is the space associated with a cylinder centered at the Sun and perpendicular to the Milky Way disk. This Solar Cylinder is located at ~ 8 Kpc from the Galactic center, with a radius of 1 Kpc and contains stars of different masses, planets, interstellar medium and HII regions. The local mass density of dark matter can be determined by subtracting the surface density of baryons from the total surface density of matter determined from an analysis of stellar kinematics. The density of dark matter is $\rho_{DM} = 0.013 \pm 0.003$ $\mathrm{M}_{\odot}$ pc^{-3} [26] and there are no evidences about the presence of a *dark disk (DD)* corotating with the baryonic matter [27, 28].

1.3.2 Rotational curves of galaxies

A galaxy is a gravitational bound system composed by planets, stars, dust, stellar remnants, interstellar gas and dark matter. All components own an angular momentum respect to the center of the galaxy so that they can rotate around it.

The rotation velocity profile of stars and gas should follow a Keplerian motion where the velocity decreases in proportion of the square of the radii instead the data show that at large radii the velocity is constant even though moves away from the center [16].

One possible solution of this disagreement is supposed the presence of a dark matter halo which extends for large radii around the galaxy and this last is located in the center of it.

For our galaxy Milk-Way the rotation curves can be only traced as far as there is light or neutral hydrogen (21 cm), namely to distances of tens of Kpc, while the dark matter halo shows its presence through gravitational effects till satellite dwarf galaxies.

How it is possible to see in figure 1.2 it is possible to see that the objects of the galaxies follow a flat rotational velocity distribution moving away from the center.

This behaviour is possible to see in every galaxies and it is possible to fit the curves by a formula called *universal rotation curve* (URC), which is a function of total luminosity and radius, comprising both disk and halo components [29, 30].

It is also interesting that the *dwarf spheroidal galaxies* (dSph), which are gas-poor, low-luminosity, low surface brightness satellite galaxies of our Milky-Way, are the objects with most amount of DM: for example Draco shows a M/L$\sim$ 440, so it is composed almost entirely of dark matter [30, 31, 32] and therefore is a preferential target for DM searches, also with the MAGIC telescopes.

1.3.3 Galaxy clusters

Galaxy cluster are the largest and most massive gravitational bound systems in the Universe, with radii of a few Mpc and total masses $M \sim (10^{14}\text{–}10^{15})$ $M_\odot$, made up by $\sim 5\%$ galaxies, $\sim 15\%$ gas, and $\sim 80\%$ dark matter. Even using alternative theories of gravity, it is difficult to explain the cluster observations without dark matter dominating the overall mass. Observations of galaxy clusters have long indicated that the velocity dispersion of galaxies in the cluster remains relatively constant with distance from the cluster center, implying a presence of an underlying mass. The last surveys of distant clusters find values for both number of baryons Ω_b and the total mass (baryonic and DM) Ω_M fully consistent with ΛCDM cosmological model [33, 34], and the hierarchical process of structure formation in the ΛCDM Universe is confirmed by the numerical simulations [35].

Signal from self-annihilation of DM particles is proportional to the integrated squared DM density along the line of sight but inversely proportional to the distance. So galaxy clusters contain a lot of DM but are located at much larger distances than other potential DM candidates: for example Perseus Cluster is located $\sim$ 1000 times farther than Milky Way satellites dwarf, but it contains $\sim 10^6$ more DM than dSph [36].

1.3.4 Gravitational lensing

The path of photons through spacetime in principle is affected by all the matter between the light source and the observer. The mass which is located between the source and the observer is capable of bending the light from the source as it travels towards the observer. For a point-like lens, there will always be (at least) two images S1 and S2 of the source, like it is shown in Figure1.3.

The equation of the angle β which is the angle between the lines of sight of lens and the real position of the source S, is given by the equation:

$$\beta(\theta) = \theta - \frac{D_{LS}}{D_S D_L}\frac{4GM}{c^2\theta} \tag{1.1}$$

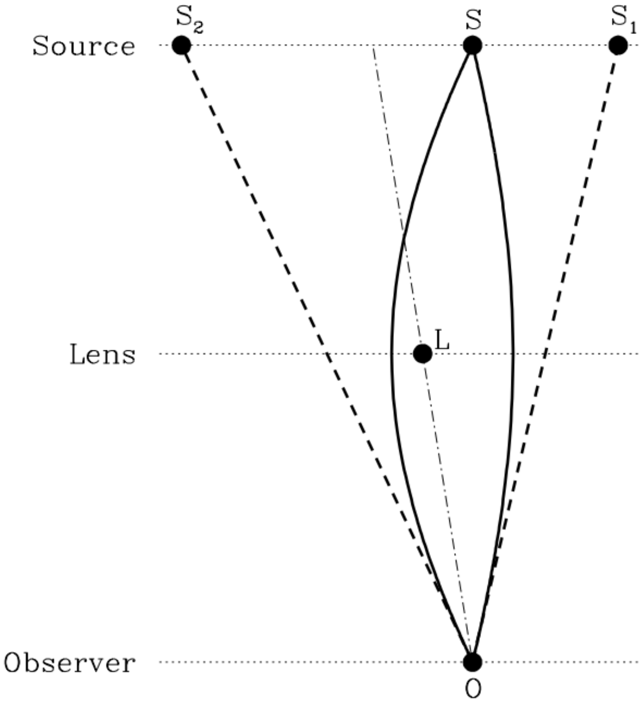

Figure 1.3: The point-like lens L located between source S and observer O produces two images S1 and S2 of the background source [37].

where D_S, D_L and D_{LS} are respectively the distances between observer and the source, observer and the lens, the lens and the source; the angle θ is the angle between the observer and the point S1 [37]. If the amount of mass inferred through this effect of the general relativity is larger than the one inferred through the measurements of the emitted radiation, it means that matter that does not emit light is present. Using the lens it is possible map the dark matter inside the galaxy cluster: limits to the DM distribution can be set by studying the distribution of image distortions, relative to the cluster center, of background galaxies [38].

1.3.5 The Bullet Cluster

The *bullet cluster* (also known as $1E0657-56$) is a cluster formed out of a collision of two smaller clusters of galaxies and it is one of the most intriguing evidences for DM existence. This structure was observed in X-ray, optical (near infrared) and radio frequencies, to obtain the highest possible amount of information because it represents an extremely rare system in a ΛCDM

Figure 1.4: Two clusters of galaxies showing the phenomenon of gravitational lensing. On the left the cluster $MACSJ0416.1 - 2403$ is showed. The picture is taken by *phys.org*. On the right there is a picture of the galaxy cluster *Abell* 370. The last image was taken by *esahubble.org*.

universe. It is interesting to see that the dark matter surface density peaks, the X-ray, and the centroids of the Sunyaev-Zeldovich (SZ) [1] signal do not coincide. Offsets between them are generated by the different behavior of the collisionless component, the dark matter, and the collisional gas during the merging process: the dark matter responds only to gravity, and therefore the core of the infalling cluster passes through that of the main cluster relatively unchanged, but the gas is subject to hydrodynamical effects, which cause large disturbances, shocks and contact discontinuities. For this reason the gas overheats and emits radiation in X range. In figure 1.5 is shown 1E0657-56 joining different picture that are taken in X-ray and optical range. The first ray was detected by Chandra X-ray Observatory satellite and shown the presence of two areas (two pink clumps in the image) where is contained most of the baryonic matter (essentially gas). From optical measurements the astronomer using the gravitational lens and discovered that most of the matter in the clusters (blue area) is clearly separate from the normal matter (pink). Similarly using offsets between bright central galaxies and the centroids of the DM mass surface density in dense cores of galaxy clusters can also be used to study dark matter cross section [39, 40].

---

[1] The SZ effect happens when the photons of the CMB scatter through inverse-Compton with the electrons of the intercluster gas (ICG) and this causes a variation of the brightness on the spectrum of CMB.

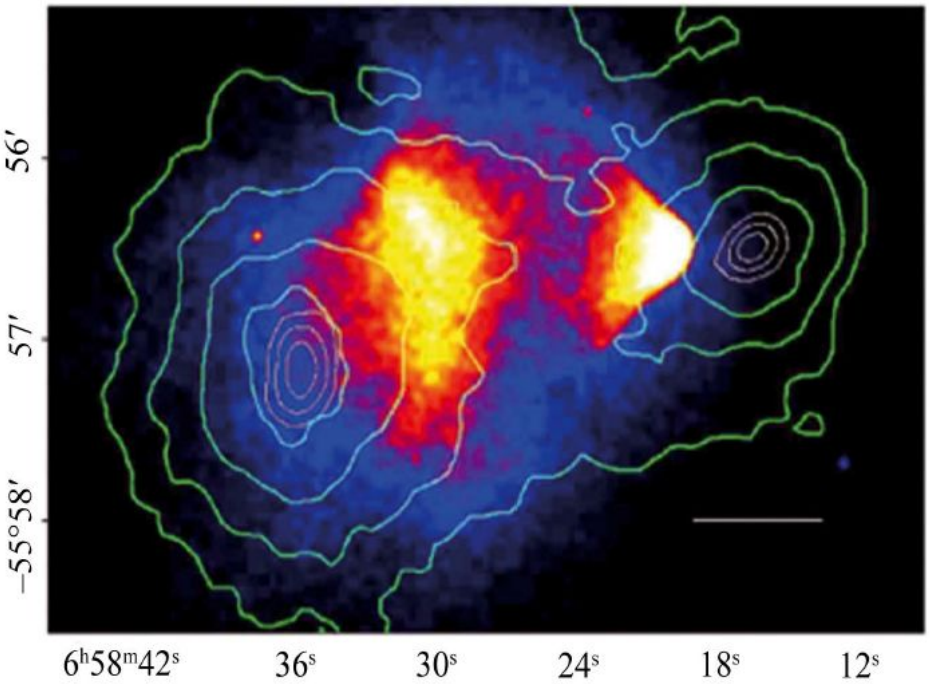

Figure 1.5: Chandra image in X range of the *1E0657-56* and shown the area where the X-ray was emitted. The green countours showing the projected total mass distribution from gravitational lensing observations. The X-ray area is associated at hot gas while using the gravitation lens was discovered that the center of the mass is located far from two peaks of gas [39]

1.4 Standard Model

During the last century a wealth discoveries in the subatomic and theoretical physics, led to a theory able to describe every known particle, their mutual interactions and hence every phenomenon associated. This theory is called "standard model" (SM) and it describes very well the physics at low energy and several experiments verified this model. The SM is composed by leptons, quarks, and bosons.

The *leptons* derive from Greek and mean "thin", "small" particles. They are the elementary particles with half-integer spin (1/2) and interact with electroweak force but not with strong interaction. The leptons are of six kinds: three particles have the charge $Q = -1$ and are the ***electron***(e^-), ***muon*** (μ^-) and ***tau*** (τ^-) and they are associeted with their *antiparticles* which have charge $Q = +1$ (e^+, μ^+ and τ^+). There are other three particles without charge and called *neutrinos*. The name of each neutrino derives from the associated particle: ***electron neutrino*** (υ_e), ***muon neutrino*** (υ_μ), ***tau***

neutrino (υ_τ). For this reason the leptons are divided in three families, each one contains one electric particle and the neutral particle associated.

The *quarks* have the same spin like the leptons (half-integer spin 1/2), and they interact with strong interaction. There are six quarks: ***up*** (u), ***down*** (d), ***charm*** (c), ***strange*** (s), ***top*** (t), ***bottom*** (b). Every quark has a different mass, a fractionary charge but the same spin. The *top* quark is the biggest particle of the SM: its mass is $173.1 GeV/c^2$.

The two features that distinguish the quarks by the other particles are the fractionary charge (for example $+2/3$ or $-1/3$) and the *colour* which can be *red*, *blue* and *green*. This is a new quantic number that only quarks can have it. Each quark can have one of the three colours and interacts with another quark with different colour.

Quarks and leptons are fermions and the name derives by the Fermi-Dirac statistic: they have half-integer spin so are subject to Pauli exclusion principle.

The remaining kind of particles are ***bosons***. The main to feature of the bosons is to have integer spin and follow the Bose-Einstein statistic. The SM bosons carries of the forces so each fundamental force has its own corresponding boson: there are the ***photon*** (γ), carries of the electromagnetic force, the bosons $W^\pm$ and Z^0, carry of the weak nuclear force, and the ***gluon*** (g) carries of the strong force. The ***Higgs*** is a boson which it does not carry a force but has spin equal to 0.

The gravitational interaction is not included in the SM and this is one of the main problems of the SM because it is the most known force and in spite of that it is not contemplated by SM. Photons and the other bosons have spin equal to 1, for this reason they are called vectorial boson. Instead the spin of the Higgs is 0 so it is scalar boson.

Mathematically, the SM is described by the gauge theory which is built on the groups $SU(3) \times SU(2) \times U(1)$ where $SU(3)$ is the gauge group for the strong interaction, $SU(2) \times U(1)$ is the gauge group for the electroweak force. At 100 GeV the weak nuclear and electromagnetic forces are unificated and it is called electroweak while at lower energies there is a spontaneous symmetry breaking (SSB) of the electroweak group to the electromagnetic $SU(3) \times U(1)$.

The standard model is a well-established theory as it provides results in perfect agreement with the experiments carried out in colliders: the discovery of the Higgs boson in 2012 allows us to say that up to a few hundred GeV the SM is correct [42]. Despite the precision of the measurements, there are a lot of motivations to think that the SM is not complete:

- there are a lot of values of parameters that are not justified;
- it is not explained why the particles are split in three families and in every family there are two leptons and two quarks;

Standard Model					
leptons			**quarks**		
Particle	q/ $\vert e\vert$	Mass	Particle	q/ $\vert e\vert$	Mass
e (electron)	-1	0.51 MeV	u (up)	+2/3	6 MeV
ν_e	0	$<$ 15 eV	d (down)	-1/3	10 MeV
μ (muon)	-1	0.106 GeV	s (strange)	-1/3	0.25 GeV
ν_μ	0	$<$ 0.17 MeV	c (charm)	2/3	1.2 GeV
τ (tau)	-1	1.777 GeV	b (bottom)	-1/3	4.3 GeV
ν_τ	0	$<$ 24 MeV	t (top)	2/3	180 GeV

Table 1.1: All the fermions of the standard model are shown with their charge and mass [41].

- gravity is not included although being one of the four fundamental forces;
- it is not clear why the charge of the quarks appears in multiples of $1/3e$;
- there is a problem with *hierarchy problem* with the energy scale;
- the asymmetry between matter and anti-matter in the Universe is not explained with the *CP violation* alone.

For these reasons the physicist are looking for new, more complete models which contain both at low energy the SM and in the same time could solve the open questions. The success of the unification of electromagnetic and weak interactions could lead to the unification also the electroweak and strong force in only one symmetry group (*Grand Unified Theories*, with the acronym *GUT*). In figure 1.6 all the fermions and bosons particles are displays; all together these compose the SM.

1.5 Standard Cosmology

Modern cosmology was born in the second decade of the XXth century after Albert Einstein published the general relativity in 1916, and when Edwin Hubble discovered the *red shift* of the faraway galaxies, in 1929.

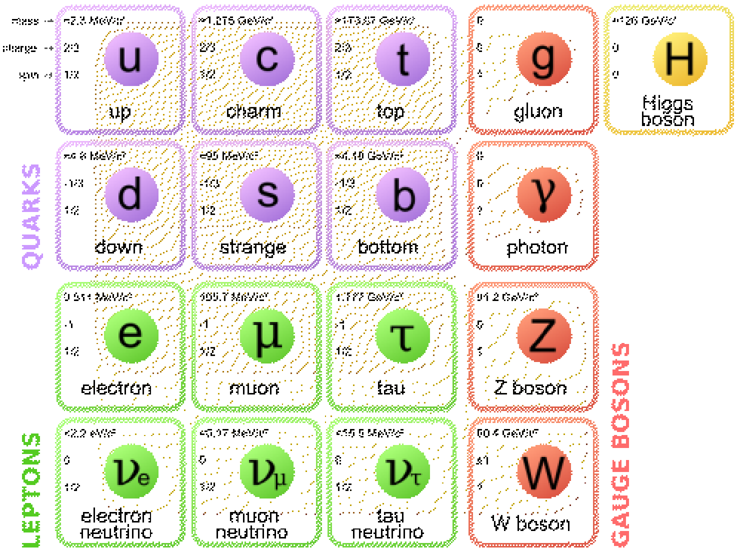

Figure 1.6: All the elementary particles of the standard model are shown in an unique scheme. In the standard model each quark and lepton owns its antiparticle but they are not shown in the figure. The image is taken from `https://www.modellinginvisible.org/standard-model/`.

The equation of general relativity links mass with the curvature of the space.

$$R_{\mu\nu} - \frac{1}{2}g_{\mu\nu}R = -\frac{8\pi G}{c^4}T_{\mu\nu} + \Lambda g_{\mu\nu} \tag{1.2}$$

where $R_{\mu\nu}$ and R are the Ricci tensor and scalar, $g_{\mu\nu}$ is the geometric tensor, G is the Newtonian costant, $T_{\mu\nu}$ is the tensor of the energy-momentum and Λ is the so called *cosmological constant*.

In cosmology volumes are so big that every force is suppressed by the great distance. The only force playining a crucial role over such distances is the gravitation force. The observation by the galaxies survey and the study of the CMB tell us that the Universe is isotropic and homogeneous at scales of $\sim 100Mpc$. This is so called *cosmological principle*.

These two properties, isotropic and homogeneity, imply a specific form of the metric in spheric coordinates:

$$ds^2 = -c^2dt^2 + a(t)^2\Big(\frac{dr^2}{1-kr^2} + r^2d\Omega^2\Big) \tag{1.3}$$

where $a(t)$ is called *scale factor* and k is the curvature of the space and it can take three values: +1, 0, -1. For the case k=0, the space has an Euclidean geometry and is called flat space. This metric is called *Robertson–Walker metric.*

With this metric we can solve the Einstein equation and the solution leads to Friedmann's equation:

$$\left(\frac{\dot{a}(t)}{a(t)}\right) + \frac{k}{a^2} = \frac{8\pi G}{3}\rho_{tot} \tag{1.4}$$

where ρ_{tot} is the total average density in the Universe. It is common to define the Hubble parameter as the ratio between the derivate of the scale factor and the scale factor itself like:

$$H = \left(\frac{\dot{a}(t)}{a(t)}\right) \tag{1.5}$$

The Hubble parameter is not a constant in time. The value of the Hubble parameter the present time for our Universe, $H(t_0) = H_0$ is 67 ± 3 km s^{-1} Mpc^{-1}, so from the equation 1.4, in a flat Universe (k=0) we can compute the value of the parameter called *critical density*:

$$\rho_{crit} = \frac{3H_0^2}{8\pi G} \tag{1.6}$$

We thus define the quantity called *density parameter* Ω_i of a substance of species i and density ρ_i as:

$$\Omega_i = \frac{\rho_i}{\rho_{crit}} \tag{1.7}$$

The $T_{\mu\nu}$ tensor of the energy momentum represents the density and pressure of a fluid. The relation between pressure and density is given by:

$$p = w\rho c^2 \tag{1.8}$$

where the parameter w is a costant in the range $0 \leq w \leq 1$. If the $w = 0$ we are speaking of *dust* and with this term we indicate every non relativistic particle. When $w = 1/3$ we speak about *radiative matter* and it indicates every relativistic particle. Instead the cosmological constant is rapresentated with $w = -1$ [43].

It is possible to compute the relative density for each kind of matter that we want to consider. The sum of every relative density must give the value of the total Ω:

$$\Omega = \sum_i \Omega_i = \sum_i \frac{\rho_i}{\rho_{crit}} \tag{1.9}$$

and the density parameter is connect with the Friedman equation by:

$$\Omega - 1 = \frac{k}{H^2 a^2} \tag{1.10}$$

The last measure of CMB and the data from the IA supernovae are coherent with a flat universe, so the parameter k is equal at 0 and this implies a value of $\Omega = 1$ [44].

The Ω_0 at present epoch is the sum of three contributors:

$$\Omega_0 = \Omega_R + \Omega_M + \Omega_\Lambda \tag{1.11}$$

where Ω_R is the relativity density of the relativity matter ($E \gg m$), Ω_M is the density about the non relativistic matter ($E < m$), and Ω_Λ is the density of the cosmological costant (or vacuum energy).

1.6 Epoches of the Universe

Using the equations from the general relativity and our knowledge on the nuclear physics, it is possible to describe the temporal evolution of one isotropic and homogeneous Universe. It is possible to describe the history of the Universe beginning from the Planck epoch when the Universe was only $t = 10^{-43}$ s old, or equivalently up to energies at which the gravitational interaction becomes considerable at quantum scale (of the order of the Planck mass, $M_{Pl} = 10^{19}$ GeV).

Planck Epoch The limit of validity of Einstein's theory in the Friedmann models is fixed by the Planck time which is of the order of 10^{43} s after the Big Bang. The temperature T at that time was around 10^{19} GeV.

GUT epoch As already mentioned, same theories expect that at high energy density the forces were unifed in an unique force. These theories are grouped under the class called *GUT (Grand Unified Theory)* and predict the existence of the new bosons which are responsible for mediating the unified force. The simplest version of a GUT is called *Minimal Supersymmetric Standard Model* and respects a symmetry group SU(5) which is spontaneously broken at an energy $E_{GUT} \simeq 10^{15}$ GeV, so that $SU(5) \rightarrow SU(3) \times SU(2) \times U(1)$ [45, 46] which correspond at time $t \sim 10^{-37}$ s.

Baryogenesis The baryon-antibaryon asymmetry is believed to be born when the Universe was described by the GUT because the degree of asymmetry that can be obtained within the standard model is much lower than that observed in the Universe. The baryogenesis started in the early Universe as a small baryon asymmetry if the following three conditions are satisfied: baryon number violation ($\Delta B \neq 0$), violation of charge and parity (*CP violation*), and *non-equilibrium conditions* (necessary in order not to erase the asymmetry). These three conditions are called **Sakarov's condition** [47, 48].

Neutrino decoupling Weak interactions maintain neutrinos in thermal equilibrium through elastic and inelastic interactions, mainly with the electrons and positrons. When the temperature arrives at ~ 1 MeV the neutrino become decoupled from the other components of the Universe. Because of missing the interaction with the other components, their number remains exactly constant at all times creating a *neutrino barrier* like the CMB.

Big Bang Nucleosynthesis At $T \sim 0.1$ MeV the first baryons bound to form the first atomic nuclei and this can explain the amount of helium and deuterium in the Universe. The standard Big Bang nucleosynthesis (BBN) provides by far the most stringent constraints to the Big Bang theory, and predictions remarkably agree with observations.

Recombination era After the nucleosynthesis the Universe was composed by plasma and the radiation and matter were coupled by the Compton scattering. When the temperature was around ~ 4000 K, the electrons and protons bound to form the first hydrogen atoms with the reaction

$$e^- + p \rightarrow H + \gamma \tag{1.12}$$

where the γ has the binding energy of the hydrogen = 13.6 eV. The recombination happened at $z \sim 1100$ and then matter was decoupled by radiation. In this circumstance was emitted the *CMBR (Cosmic Microwave Background Radiation*) and the Universe became optical thin.

Reionization era After the CMB the Universe was pervaded by neutral hydrogen and radiation. The time between CMB and the formation of the first structures is called *Dark age* because every photon was created after. The ultraviolet radiation from the first stars ionize regions around them and heated the surrounding *intergalactic medium (IGM).* After a sufficient number of ionizing sources have formed, the ionized fraction of the gas in the Universe rapidly increases until hydrogen becomes fully ionized. This period, during which the cosmic gas went from neutral to ionized, is known as the *Epoch of Reionization.*

1.7 Theoretical arguments in favor of dark matter

In addition to the data collected by observation of galaxies and cluster of galaxies, which could be explained with the presence of the dark matter, there are other indirect proofs of the cosmologic theories. Dark matter is necessary to describe different epoches of the universe and at the same time it is possible to compute the amount of dark matter necessary to describe the evolution of the Universe through the different epoches.

1.7.1 Big Bang Nucleosynthesis

The synthesis of the light elements is an important proof about the evolution of the Universe in the big bang model because the synthesis is very sensitive to physical conditions in the early radiation-dominated era. The Universe was homogeneous and isotropic at the time of nucleosynthesis, for $T > 1$ MeV the particles were in thermal equilibrium, the number of neutrino types is not high ($N_\nu \sim 3$), the magnetic field was very weak, there were not different area with only matter and other with antimatter, the density of any exotic particles was negligible respect to the particles of the SM [43].

At higher temperatures, weak interactions were in thermal equilibrium, thus the ratio between neutrons and protons was $n/p = e^{-Q/T}$, where Q is the difference in mass between the two particles.

$$n + \nu_e \rightleftharpoons p + e^- \quad \text{and} \quad n + e^+ \rightleftharpoons p + \bar{\nu_e}$$

It is possible to introduce a new parameter $X_n = n/(n+p)$ which represents the fraction of the neutrons on the total of the baryons. The neutron fraction at this time was $\sim 1/6 = 0.17$. The number of the neutrons is stable untill the reaction is balanced. Below the temperature $T \sim 1.3 \times 10^9$ K, the neutrons may decay in protons, positrons and antineutrinos, with an average time ~ 15 min.

The nucleosynthesis chain began via the formation of the deuterium and gradually with Helium and heavier elements. The rates of these reaction depend on the density of baryons which is usually expressed in function of the number of the photons as $\eta = n_b/n_\delta$. The chain of the nucleosynthesis begins with the formation of the lightest nucleus except H: the deuterium (^{2}H or D). The photons are distributed with an Maxwell-Boltzmann distribution and there are an high number of photons in tail which might dissociate the deuterium nuclei and other more heavier nuclei. Therefore is necessary to wait that the mean energy falls below $T \sim 0.1 MeV$. After that moment the chain of the nucleosynthesis can begin with the reaction:

$$p + n \rightarrow D + \gamma \quad , \quad D + p \rightarrow ^3He + \gamma \quad , \quad ^3He + D \rightarrow ^4He + p \tag{1.13}$$

Nuclei heavier than Helium have a stronger Coulumb barrier and there are not stable nuclei with mass number 5 or 8. The ^3He is unstable isotope and decays in 12.3 years but a small fraction of the litium could be produced with the reaction $^3He(^4He,\gamma)^7Li$. The other elements have been synthesized into the stars because the energy density at the epoch of the nucleosynthesis was not enough to exceed the Coulumb barrier proceding in the chain of the synthesis of elements.

The *Standard Big Bang Nucleosynthesis (SBBN)* predictions can be compared with observational determinations of the abundances of the light elements.

The abundance of $^4_2$He, usually indicated with the symbol Yp, predicts with an impressive precision, $Yp = 0.2486 \pm 0.0002$, where we use the most recent evaluation [49]. Deuterium and ^{3}He SBBN predictions are more sensitive both to nuclear physics and to η_b input. Reactions involving these elements are well measured, and with the current WMAP input SBBN is capable of making fairly precise predictions of these abundances: $D/H = 2.49 \pm 0.17 \times 10^{-5}$, $^3He/H = (1.00 \pm 0.07) \times 10^{-5}$. If we compare these values with observations, we can see that predicted values are very close to the measured ones.

Consistency between theory and observations leads to a conservative range of

$$5.1 \times 10^{-10} < \eta < 6.5 \times 10^{-10} \tag{1.14}$$

and the parameter η is related with the fraction of baryons: $\Omega_b = 3.66 \times 10^7 \eta h^{-2}$. From the Planck measurement the value of $\Omega_b h^2$ is ~ 0.022 and this value translates into a value of $\eta = 6.16 \pm 0.1$ [50]. This results can be used to predict the light element abundance which can in turn be compared with the observation.

The abundance of deuterium is the most important because it is more sensitive to the SBBN model than that of other elements and, starting from it, it is possible to compute the abundance of the other elements. The value of the ratio $\Omega_b h^2 \sim 0.022$ is in accordance with the same parameter $\Omega_b h^2$ computed

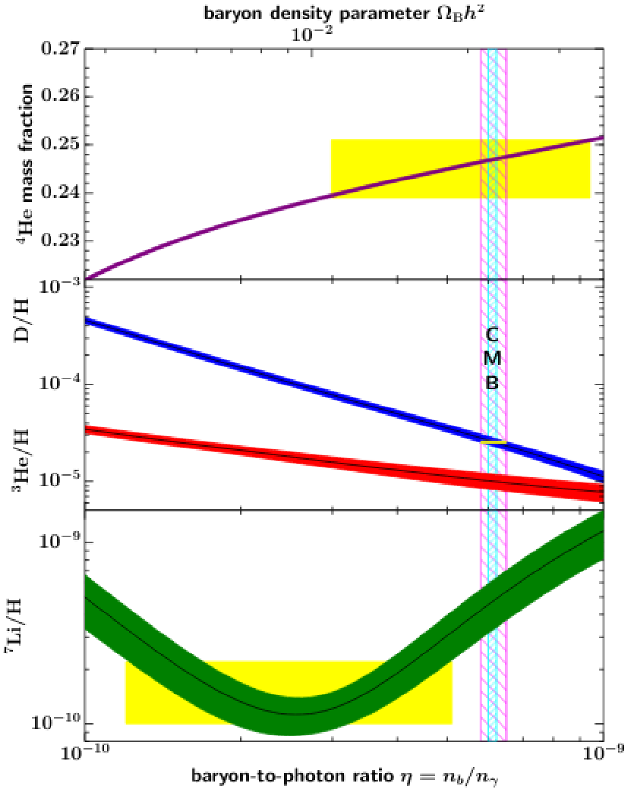

Figure 1.7: The primordial abundances of 4He, D, 3He, and 7Li as predicted by the standard model of Big-Bang nucleosynthesis. The bands show the 95% confidence range. The yellow boxes indicate the observed light element abundances. The vertical magenta lines indicate the BBN D+He concordance at 95% CL while the narrow vertical band indicates the CMB measure of the cosmic baryon density [49].

by the CMB.

The lastest measurements of Ω_0 set the ratio between matter and other components to 0.3 and the BBN puts a strong limit on the quantity of the baryonic matter: baryonic matter composes only the 0.02 the universe and around 0.27 is composed by non baryonic matter. So, a high quantity of dark matter is necessary if the Universe is flat.

1.7.2 Cosmic Microwave Background

The **Cosmic Microwave Background** (CMB) is an important ingredient of the universe until the recombination era.

The epoch of the recombination happened at $z \sim 1100$ when the plasma was cold enough to let to bind the electrons and the protons, in this way the first atoms of hydrogen were created. The CMB is also the border for the path of the photons: before the CMB release the plasma was optical thick and this separates the dark age of the universe from the universe which we may see with the telescopes. In this way we use the data from studies of the CMB and check with the different theoretical models and measure the cosmological parameters.

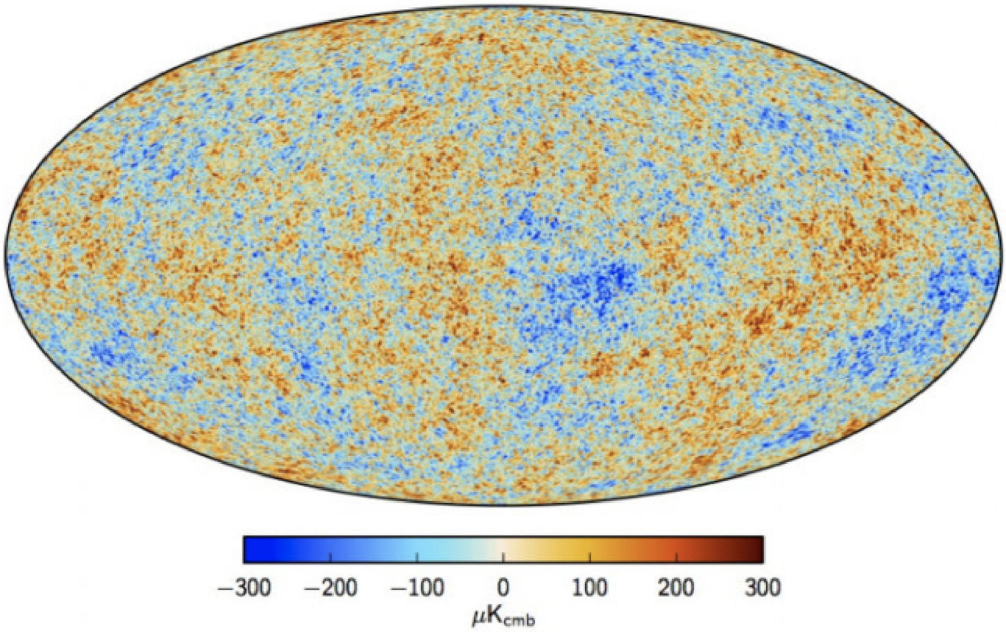

Figure 1.8: Maps of the tiny fluctations in the CMB radiation. Planck satellite scanned all the sky observing the CMB temperature anisotropies [**ade2014 k**].

The spectrum of the CMB today corresponds to a black-body at a temperature of $T_0 = 2.72548 \pm 0.00057$ K and it is showed in figure 1.8 [50, 51]. This temperature is not perfectly equal in all the directions but show anisotropies which are one of the most powerful probes what happened during the dark age.

These anisotropies are usually expanded in spherical harmonics series $Y_{lm}(\theta, \phi)$ such as:

$$\frac{\Delta T}{T}(\theta, \phi) = \sum_{l=2}^{+\infty} \sum_{m=-l}^{+l} a_{lm} Y_{lm}(\theta, \phi) \tag{1.15}$$

Each spherical harmonic has an angular resolution given by $\theta = \pi/l$, the coefficients a_{lm} provide an independent description of the amplitude of fluctuations on the angular scale defined by l and satisfy the condition:

$$\langle a^*_{lm} a_{lm} \rangle = C_l \delta_{ll'} \delta_{mm'}$$

and C_l is the *angular power spectrum* defined by the equation:

$$C_l = \frac{1}{2l+1} \sum_{m=-l}^{l} |a_{lm}|^2 \tag{1.16}$$

If the temperature fluctuations are assumed to be Gaussian, as appears to be the case, all of the information contained in CMB maps can be compressed into the power spectrum, essentially giving the behavior of C_l as a function of l. Usually is $l(l+1)C_l/2\pi$ is plotted as in figure 1.9 where the data collected by Planck satellite are shown.

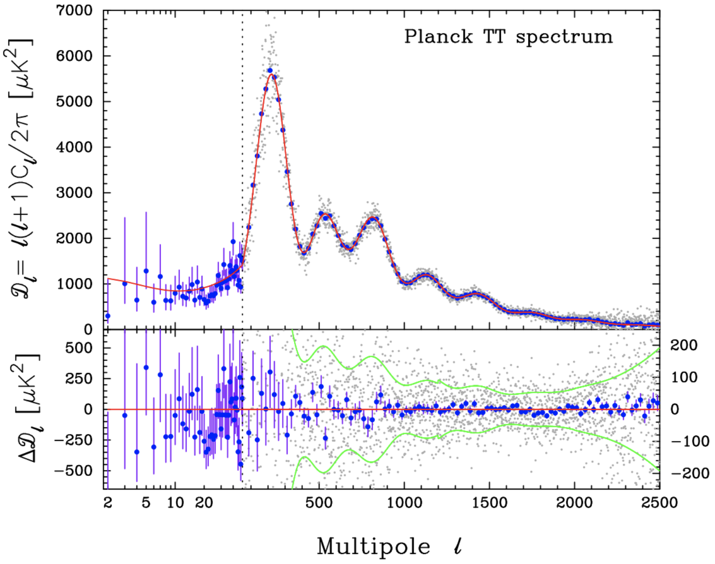

Figure 1.9: The power spectrum form Planck measurements of temperature variations in the CMB sky. Until the multipole $l = 49$ the power spectrum is plotted in logarithmic scale while the scale changes from the $50 \leq l \leq 2500$ and becomes linear. In the second scale the blue points show averages in bands of width $\Delta l = 25$ together with 1σ errors. The red line shows the temperature spectrum for the best-fit base ΛCDM cosmology. The lower panel shows the power spectrum residuals with respect to this theoretical model [50].

The PlancK satellite is dedicated to measurements of the CMB anisotropies and its results are in perfectly according with the ΛCDM model. I summarise some results in the Table 1.2 [50, 52].

Parameter	Value
k_s	0.9585 ± 0.0070
Ω_Λ	0.767 ± 0.028
Ω_{DM}	0.214 ± 0.028
Ω_b	0.046
$\sum m_\nu$	< 0.66 eV
N_ν	3.36 ± 0.34
$\Omega_\Lambda + \Omega_m$	~ 1

Table 1.2: Values of the cosmological parameters from analysis of Planck data [50].

In addition it is possible to understand also the role of the dark matter played during the dark age. If the dark matter particles could decay or annihilate, extra energy would be injected into the baryonic gas. This could delay the formation of stars and structures because an amount of energy flows from dark matter to baryonic matter [53].

1.7.3 Primordial perturbation

Small variations in the CMB temperature across the sky (as shown in figure 1.8), reflect spatial variations in the density of the primordial plasma, $\delta\rho(t, \bar{x}) = \rho(t, \bar{x}) - \bar{\rho}(t)$, and related perturbations of the spacetime geometry, $\delta g_{\nu\mu}(t, \bar{x}) = g_{\nu\mu} - \bar{g}_{\nu\mu}$.

The universe appears isotropic and homogeneous for large scales and the evolutionary models do not foresee the formation of structures except for the introduction of small perturbations. So it is therefore necessary to introduce a theory of perturbations capable of explaining the structure of the Universe today.

Perturbations were generated when the Universe was young by the quantum field fluctuations. The Inflation grew up the fluctations from an atomic scale to cosmological scale

Primordial inflation also allows us to put constrains on the origin and the statistical properties of the primordial perturbations. The tremendous inflationary expansion bridges the gap between the subatomic length scales, on which quantum fluctuations are generated, and astrophysical scales, relating the seeds of the structure we observe in the universe to quantum fluctuations originated some 10^{-35} seconds after the big bang. In other words, from CMB anisotropies, that are directly related to the primordial density fluctuations, we learn about physical processes occurring at extreme energies, unattainable in any conceivable accelerator on Earth. Thus studies of the CMB bring us to the deepest questions about the origin of the universe. Although the inflationary scenario provides an impressive set of answers, the underlying physics is not well understood, and we need to dig more deeply into the extraordinary wealth of information contained in CMB maps.

1.8 Possible candidates

A lot of evidences support the presence of dark matter and they emerge both from observation data and from theoretical evolutionary models of the Universe. The best model to explain all the data describes the Universe in the ΛCDM (where CDM is the acronym of *cold dark matter*) although the nature of both dark energy and dark matter is still unknown.

In the meanwhile, some limits have been placed on dark matter:

- dark matter should be composed by not baryonic matter and its amount is $\sim 82\%$ of the matter in the Universe;
- DM particles do not have electric charge;
- interact only weakly and gravitationally;
- play a leading role in the structure formation in the Universe, as the fluctuations in the DM density are dominating the evolution of the perturbations in the matter dominated era;
- be consistent with the BBN and not contradict the observed abundances of light elements;

A particle is considered a good candidate for constituting dark matter if it satisfies all the above points at the same time.

1.8.1 Candidate in SM

The only electrically neutral and long-lived particles in the Standard Model (SM) of particle physics are the neutrinos. Several experiments have shown that neutrinos have mass so they could play a DM role in the Universe. Measurements of the electron spectrum of $\beta-$*decay* put the combination of neutrino masses below 2 eV while from cosmological data one can infer an upper bound of the sum of neutrino masses between 0.58 eV and 0.12 eV. Neutrino could be the DM if its mass is around 11.5 eV. Moreover, neutrinos decouple like relativistic particles and represent a form of *Hot Dark Matter*. In this case the history of structure formation would be very different and the Universe would look rather differently nowadays.

To explain the composition of the halo and solve the problems of the rotation curve in the Milk Way, one idea was to search the astronomical object which did not emit light [54]. This objects are called *massive astrophysical compact halo object* (**MACHO**) and inside this class there are spheres of hydrogen and helium too light to initiate nuclear burning (jupiters at $0.001M_\odot$, brown dwarfs at $0.01M_\odot$, etc.), as well as the massive black hole remnants of an early generation of stars.

The MACHO [55] and EROS [56] experiments have attempted to find the dark matter of our Galactic Halo by monitoring millions of stars in the neighboring Large Magellanic Cloud (LMC). When a Macho crosses the line of sight between a star in the LMC and us, the Macho's gravity can magnify the light of the background stars. This effect is called *microlensing* and its duration is given by $\Delta t \propto \frac{\sqrt{m}}{v}$ where m is the mass of the Macho and v is the velocity perpendicular to the line of sight.

From the data and models the MACHOs could explain till 30% of mass of the halo and no models can cover all the halo mass. Hence there is evidence that a nonbaryonic component to the Halo of our Galaxy is required [57, 58].

1.8.2 Non Baryonic matter

It is expected from cosmology that the dark matter has to be composed by exotic particles. It is possible to adds "hypothetical" particles if the new particles can satisfy all the issue that I describe before.

In the past a lot of particles have been proposed as good candidates but in this thesis I want to take in consideration only the most popular candidates so I will do a brief explanation of the particles arisen from supersymmetry, Kaluza Klein DM particles and axions.

WIMP

WIMP is the acronym of ***Weakly Interact Massive Particle*** and with this name are indicated particles with mass in range from $\sim$ GeV to TeV and could interact with W and Z bosons but not with gluons and photons. If WIMPs exist and are stable (or however with a mean life as long as Hubble time) are naturally produced in the early Universe and are present nowadays with a relic density consistent with that required of dark matter.

In the early Universe WIMPs and baryonic particles interact. After *freeze* *out*, the interactions that change the number of dark matter particles become negligible, but interactions that mediate energy exchange between dark matter and other particles may remain efficient.

The number of the particles is described by the Boltzmann equation:

$$\frac{dn}{dt} = -3Hn - \langle \sigma v \rangle (n^2 - n_{eq}^2) \tag{1.17}$$

where n is the number density of dark matter particles, H is the Hubble parameter, $\langle \sigma v \rangle$ is the thermally averaged annihilation cross section, n indicates the number density of DM particles, generally are denoted with χ, and n_{eq} is the dark matter number density in thermal equilibrium. The thermal relic density is given by:

$$\Omega_\chi = \frac{x_f T_0^3}{\rho_c M_{PI}} \langle \sigma v \rangle^{-1} \tag{1.18}$$

where x_f is the ratio m_χ / T_f, the subscripts 0 denotes present-day quantities and M_{PI} is the Planck mass. We see that the thermal relic density is insensitive to the dark matter mass m_χ but is inversely proportional to the annihilation cross section $\langle \sigma v \rangle$ [59]. It is possible to use another parametrization and showing that the cross section is a function of the mass of the particle m_χ and the constant $g_{weak} = 0.65$ that is the weak interaction gauge coupling. In this parametrization the equation 1.18 is as function of the mass particles as shown in Figure1.10.

A thermal cross section $\langle \sigma v \rangle \sim 3 \times 10^{-26}$ is the value needed to obtain $\Omega_M = 0.28$. It is interesting to note that a particle which has mass in the range $m_\chi \sim 100$ GeV to ~ 1 TeV can make up for all the needed DM. The resulting relic number density of $\chi-$particles then depends only on the ratio of the annihilation cross section of χ and the Hubble scale near the freeze-out temperature. This ratio is in good agreement with that deduced from astrophysical and cosmological experiments; this is called the ***WIMPs miracle***.

The WIMP miracle not only provides a model-independent motivation for dark matter at the weak scale, but it also has strong implications for how dark matter might be detected. χ particles must annihilate to other particles. It is not possible to know which particles are generated after the first annihilation, but we can consider that in the last scattering SM particles are produced. The physical process is described by $\chi\chi \rightarrow$ SM SM and this interactions suggests three promising strategies for dark matter detection: indirect detection, direct detection, produced in the collider, how I described in section 1.1.

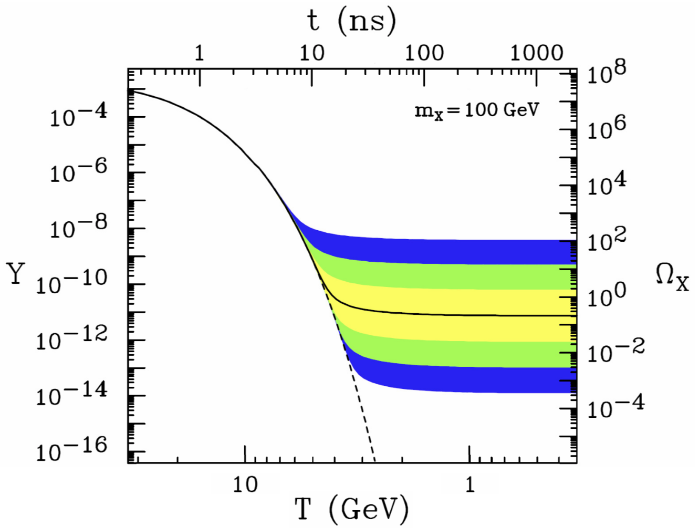

Figure 1.10: The comoving number density Y (left) axis and resulting thermal relic density (right) axis of a 100 GeV DM particle. The colored areas represent cross section which difference by 10, 100 and 1000 from the correct value [59]

Who are the WIMPs?

With the acronym WIMP we are representing a generic particle which owns great mass and interacts only by weak nuclear force. Every particle which satisfies all these properties is a good candidate to be a WIMP. Moreover new possible candidates have to be included a theory which expands the SM (for istance *supersymmetry* or *Kaluza-Klein dark matter*).

Neutralino These particles arise from the supersymmetry and are the lighest supersymmetric particles (LSP).

SUperSYmmetry (SUSY) is an elegant way to solve the gauge hierarchy problem and appears like a natural extension of the SM. In fact SUSY implies that all the SM particles have a new partner particle, which has the same quantum numbers and gauge interactions, but differs in spin by 1/2. The supersymmetry transformations turn bosons into fermions and vice versa, so that the members of supermultiplets have different spins. The partner of the leptons are called *sparticles* and are bosons (for example $e \to$ *selectron* or the partner of $\nu \to$ *sneutrino*), the partner of the bosons are called with the same name but with add the suffix *-ino* (for instance fotone → *fotino*, $Z^0 \to$ *zino*) [60]. The *Minimal Supersymmetric Standard Model (MSSM)* is the SUSY model which owns the minimal particle content compatible with known physics. In this model the neutralino is a linear combination of photino

($\tilde{\gamma}$), zino ($\tilde{Z}$) and also the neutral higgsino doublets $\tilde{H}_u^0$, $\tilde{H}_d^0$. Therefore, SUSY predicts the existence of a new stable elementary particle having a mass less than a few TeV and having weak interactions with ordinary matter. In addition neutralino has spin 1/2 and is its own antiparticle (Majorana fermions) so it is a perfect candidate to represent WIMP class [61].

Kaluza-Klein particle An alternative to SUSY is the existence of extra spatial dimension where the partner of the SM particles live. The idea was proposed by Kaluza in 1921 and then by Klein in 1926 and from there many theories were born from that idea. Scenarios in which all fields are allowed to propagate in the bulk are called *Universal Extra Dimensions (UED)*. In UED, all particles propagate in flat, compact extra dimensions of size 10^{-18} m or smaller. Every SM particle has an infinite number of partner particles, with one at every Kaluza-Klein (KK) level n with mass $\sim nR^{-1}$ where R is the compactification radius, in other words the size of the extra-dimension [59]. Such models provide, in the form of stable Kaluza-Klein (KK) partners, the only specific dark matter candidate to emerge from theories with extra dimensions. The Lightest Kaluza-Klein Particle (LKP) is a candidate to compose dark mater while the heavier KK modes cascade decay to the LKP by emitting soft standard model particles [62].

Tipically in the minimal UED, the dark matter candidate is in general a vector particle, B^1, the KK first level of the $U(1)$ gauge boson. The mass of the LKP is between 600 GeV and 1.3 TeV, heavier then the predicted mass of the neutralino [63, 64].

Candidates from SUSY

Other particles could satisfy the DM requests and arise from SUSY theory.

- *Sneutrino* is the supersymmetric partner of the neutrino with spin equal to 0. We find that the sneutrino relic density is cosmologically interesting in the mass region 550 GeV $\leq m_\nu \leq$ 2300 GeV [65].

- *Gravitino* is a superpartner of the graviton with a spin equal to 3/2. In some supersymmetric scenarios is the gravitino the lightest supersymmetric particle instead of the neutralino. Gravitino decoupled at temperatures of order the Planck scale. If they behave as standard stable thermal relics then they must have a mass less than a few keV. With only gravitational interactions, however, gravitinos are very difficult to observe

- *Axino* is the superpartner of the axion (other candidate particle to compose the DM) and it is arises from axion (see §1.8.2) and supersymmetric theory. When the axino is the lightest supersymmetric particle, a mass of a few keV implies that it can be warm dark matter.

Sterile Neutrino

One of the few still open problems of the Standard Model of particle physics is the fact that neutrinos are not massless. It is possible to create new models adding new particles and a very simple extension of the SM is to add sterile neutrinos to the SM Lagrangian. This model is called *Neutrino Minimal Standard Model* (νMSM).

Neutrinos in principle were a very natural DM candidate but a mass $m_\nu \sim 11.5$ eV was required. This is in conflict with the existing experimental bounds: measurements of the electron spectrum of β-decay put the combination of neutrino masses below 2 eV.

The mass of the sterile neutrino is between 2 and 5 KeV. The minimal number of sterile neutrinos, which can explain the dark matter in the universe, is N = 3. In this case only one sterile neutrino can be the dark matter. A sterile neutrino is an example of decaying dark matter. Through its mixing with the ordinary neutrinos, it can decay (via Z boson exchange) into three (anti)neutrino [66].

In this scenario, dark matter sterile neutrinos are produced in the early Universe due to their coupling to active neutrinos. Sterile neutrinos are neutral, massive and, while unstable, can have a lifetime longer than the age of the Universe. One difference from WIMPs is that sterile neutrinos were never in thermal equilibrium in the early Universe. There are many ways to produce sterile neutrinos. Their masses are in keV range, so sterile neutrino particles are born relativistic and represent a candidate of warm dark matter (WDM) but it could be also possible to consider them as cold candidates if there is a very small lepton asymmetry, in which case they are produced resonantly with a non-thermal spectrum [66, 67].

Superheavy Dark Matter

While a thermal origin for WIMPs is the most common assumption, it is not the simplest possibility. It has been recently pointed out that DM particles might have never experienced local chemical equilibrium during the evolution of the universe, and that their mass may be in the range 10^{12} to 10^{19} GeV, much larger than the mass of thermal WIMPs. Superheavy DM particles have been called *wimpzillas* [68, 69]. These particles have extremely low interaction rates, and are assumed be stable on cosmological timescales, but may annihilate or decay to SM particles which could be detected as UHECRs.

Axions

In a first moment the *axions* was introduced in an attempt to solve the problem of CP violation in Quantum Chromodynamics (QCD) in particle physics by Peccei and Quinn (PQ) [70], and they have also often been discussed as dark matter candidates. If the WIMPs is a class composed by massive particles, other extensions of the SM predict another class of particles called **WISPs** (Weakly Interacting Subelectronvolt Particles). The axions and the more general family of axion-like particles (ALPs) are the best candidates to constitute WISPs and they often arise as Nambu-Goldstone bosons associated with the breakdown of global symmetries.

The QCD theory is a non-Abelian gauge theory which describes strong interactions through the Lagrangian ($\mathcal{L}_{QCD}$) and describes also the CP-violation:

$$\mathcal{L}_{CP-viol} = \frac{\theta}{32\pi^2}\epsilon^{\mu\nu\rho\sigma}G_{\mu\nu}G_{\rho\sigma} \tag{1.19}$$

where $G_{\mu\nu}$ and $G_{\rho\sigma}$ are the gauge-field (the gluon) tensor, $\epsilon^{\mu\nu\rho\sigma}$ is the Levi-Civita symbol while θ is the term of the coupling and it has to be determined experimentally. Θ gives rise to an electric dipole moment (EDM) for the neutron and it is constrained to $|d_n| < 2.9 \times 10^{-26}$ e cm ($90\% C.L.$), implying $\theta \leq 10^{-10}$. The problem to explain so small values of θ is precisely the strong CP-problem and a solution does not exist inside the Standard Model.

Peccei and Quinn solved the problem proposing a dynamical pseudoscalar field coupling with the gauge field tensor, so setting the $\theta = 0$ via QCD non-perturbative effects.

The axions arise when the global (quasi-)symmetry $U(1)$ is spontaneously broken at a scale f_a and they have a very tiny mass given by:

$$m_a \simeq \frac{\lambda_{QCD}^2}{f_a} \simeq 6 \times 10^{-6}\text{eV}\Big(\frac{10^{12}\text{GeV}}{f_a}\Big) \tag{1.20}$$

for this reason they are pseudo-Nambu-Goldstone boson, stable and with a range of mass $\sim 10^{-6} - 10^{-2}$ eV. In equation 1.20 the term $\Lambda_{QCD} \sim 200$ MeV is the QCD energy scale.

They can couple with photons and the Lagrangian of the coupling is:

$$\mathcal{L}_{a\gamma\gamma} = \frac{1}{4} g a F_{\mu\nu} \tilde{F}^{\mu\nu} = g a \bar{E} \cdot \bar{B} \tag{1.21}$$

The Peccei-Quinn's idea is motivated to provide a solution of the strong CP problem but this concept can be generalized for the breaking of other global symmetries creating other pseudo Nambu-Goldostone bosons, called ALPs.

Axions can act as dark matter if they do not decay in the lifetime of the Universe. The main decay channel of the light axion is the decay into two photons and these photons can detected by MAGIC telescopes. The cosmology of the axion depends crucially on the ordering of PQ symmetry breaking and inflation. For this there are different scenarios to explain the production of axions in early Universe and each one depends to the initial conditions.

Chapter 2

Dark Matter halo and Globular Clusters

Modern cosmology is based on the **cosmological principle**: at the largest scale the Universe is the same in every direction that one observes (*isotropy*) and has the same physical properties everywhere (*homogeneous*). But at the small scale the Universe is not homogeneous and it is possible to recognize the presence of several structure. The parameter $\Delta = \Delta\rho/\rho_c$ is called *density contrast*: above $\Delta \sim 1$ the evolution of perturbations is not linear and bound structures are created. The values of the density contrast at time t_0 are showed in the table 2.1 [71].

Scale	Structure	Mean density
30 kpc	galaxy	$10^6 \times \rho_c$
1 Mpc	galaxies cluster	$10^3 \times \rho_c$
30 Mpc	Supercluster	$1 - 10 \times \rho_c$

Table 2.1: Density contrast for different scale and $\rho_c = 10^{-30}$ g cm^{-3} [71].

In 1902 Jeans showed that in a self-gravitating and non-relativistic system[1] an instability rises and it is called *gravitational Jeans instability* [72], then this theory was extended in general relativity by Lifshitz and now this model is now the fundamentals of the standard model for the origin of galaxies and

---

[1] Jeans studied the evolution of a nebula to understand the mechanism to arise the stars and planetary system.

large-scale structures.

Jeans demonstrated that a small fluctuation $\delta\rho$ (with $|\delta| << 1$) in an homogeneous fluid with mean density ρ and velocity of the particles v, could evolve with time. In particular if the pressure forces are less than the force of gravity then the instability will tend to increase. The threshold determining if the cloud will collapse or the pressure forces will prevent it is defined by the *Jeans lenght*, λ_J, coherently is also defined the *Jeans mass*, M_J the mass inside a sphere with radius $\lambda_J/2$. If the mass of the overdensity (or the perturbation) is above that limit the perturbation will grow and when the $|\delta| \simeq 1$ the evolution of the perturbation becomes not linear and the Jeans theory cannot be applied on it. In non-linear regime computer simulations are needed to follow the evolution of the object in detail.

The current model of the structure formation is founded on the presence of the quantum perturbation in the early Universe. The inflation expanded those perturbation which continued to evolve in a more diluted and ever expanding Universe. The study about the spectrum of perturbations and the correlation function indicate that the structures were formed following an hierarchical model called *bottom−up*: small structures were created first, then these merged creating bigger structures [73].

2.1 Theory of the structure formation

The inflation was introduced as possible solution to the cosmological dilemmas known as the horizon, flatness, monopole and entropy problems. But the inflation is necessary also to explain the formation of the structures.

Inflation expanded the Universe ~ 30 times so both quantum fluctuations and the perturbations connected to the metric were stretched to cosmological scales. Before this event the Universe was homogeneous and isotropic while after the violent expansion started shown some small density fluctuations.

When a perturbation is small, $\delta << 1$, the evolution is linear and it is possible to describe it through Jeans analysis. The Jeans analysis in linear evolution of the perturbations shows that one Universe composed by relativistic matter and non-relativistic matter of the standard model cannot produce what we observe mainly because the perturbations evolved too late and there is not the time to conglomerate the matter to build the structures.

Baryonic models fail to describe the structure of Universe today because there is not the compatibility between ρ/ρ predicted and the fluctuations observed in the CMB [74, 75]. Moreover the nucleosynthesis requires that the $\Omega_b h^2 = 0.02$ so the majority of the matter of the Universe must be not baryonic [49]. I denote with the suffix X some generic particle produced in the early Universe and not being part of the standard model. The abundance of this kind of particles nowadays is called *cosmic relics*. The cosmic relics could be divided in two different classes: *hot relics*, if the particles were relativistic when they decoupled from the Universe and in this case they are denoted as *hot dark matter* (HDM) particles, and *cold relics*, if the particles were non-relativistic at the time of decoupling and in this case they are denoted as *cold dark matter* (CDM) particles.

This characteristic also implies a different evolution of the perturbations according to the chosen particle model. HDM particles tend to escape from the potential wells and consequently the smallest perturbations are damped and the larger ones remain. The first objects formed have the size of clusters of galaxies ($\sim M_J = 10^{14}\ M_\odot$) and the other objects form afterwards from their fragmentation: it is called *top-down* scenario.

For CDM particles the situation is different: the perturbations which are smaller than $M_J \simeq 10^5$ M$\odot$ are obliterated while the perturbations that are greater than $M_J \simeq 10^5$ M$\odot$ grown. In this way first the small structures are formed and from their merge the bigger structures. This scenario is called *"bottom-up"* and it is the best model fitting the observations of the Universe as seen in figure 2.1 [76, 75].

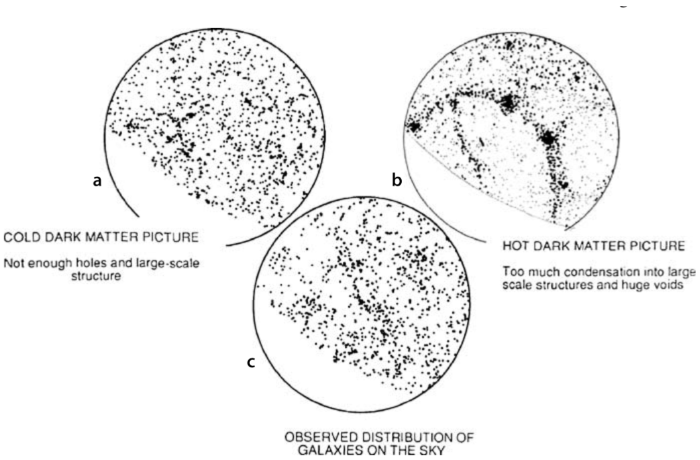

Figure 2.1: Inside the bottom circle is reproduced observed galaxies distribution. Early simulations of CDM on the left-top and HDM on the right-top compared with the observed galaxy distribution on the sky. The CDM model fits the distribution of galaxies better than the HDM [76]

The ΛCDM is the model that best fits the data with the theory and including the cosmological costant Λ and the *Cold Dark Matter*. However N-bodies simulations show two important considerations at small scales:

1) CDM collapse leads to cuspy dark matter halos whose central density profiles rise as $r^{-\beta}$, where β could assume values between $\sim 1 - 1/5$, but the rotational curves of the galaxies show a constant density core in the dark matter distribution [77, 78];

2) inside the halos would be created a large number of other small structures, called subhalo. This prediction is in contrast with the number of the Milk Way satellites which are ~ 10 [79, 80].

These two problems are often called *"cusp-core problem"* (point 1 figure 2.2(a)) and *"missing satellites problem"* (point 2 figure 2.2(b)) and this show that a small scales the CDM theory loses its strength.

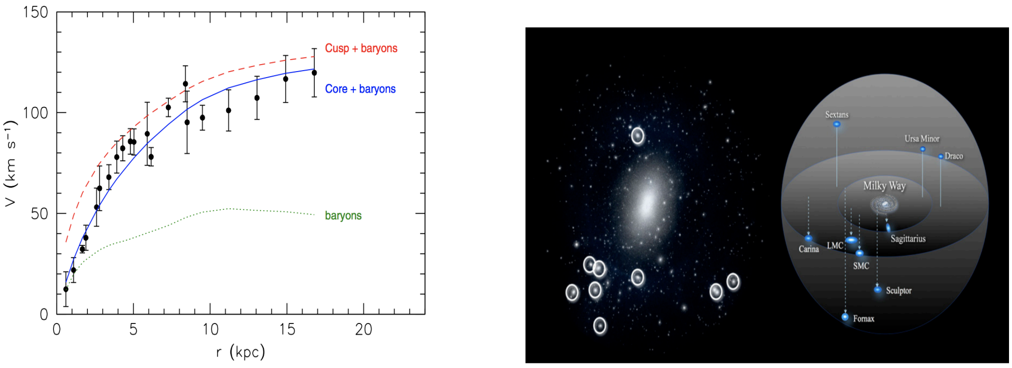

(a) cusp core problem

(b) Missing satellites

Figure 2.2: (a) Tangential velocity plot of galaxies as in function of the distance. The points are the measured rotation curve of F568-3. They are compared with the model fits assuming a cored dark matter halo (blue solid curve) or a cuspy dark matter halo (red solid curve). (b) A simulation (left imagine) compared to Milk Way's satellites. In the simulations there are more subhaloes and satellites than in the our galaxy, and the white circles mark the nine most massive subhaloes but their central densities are too high to host the dwarf galaxies [81].

2.1.1 Dark matter halo

In hierarchical cosmologies, dark matter halos arise from the gravitational collapse of density peaks in a random perturbation field. It is likely that the shape of dark matter halos may be of triaxial ellipsoids and typically host substructures which show like overdensity volumes.

The spiral rotation curves have revealed the presence of a dark mass component in galaxies which embeds all that. Moreover other observational probes, like stellar kinematics, gas rings, motion of globular clusters, planetary nebulae, gravitational lensing and satellite galaxies, can be used as tracker to map halo mass distributions.

To know the distribution of the dark matter is also the key input to the indirect detection for predicting and interpreting event rates, for instance in $\gamma-$ray observations.

In consequence it is necessary to find a theoretical model to describe the halo and subhaloes. The presence of the dark halo is also predicted from the N-body simulations in a ΛCDM model, which show that a two-parameter model describes the density profile of dark matter halos over a range of halo masses [82].

It is not easy to define the border of the haloes because of their dynamic nature and their absence of spherical symmetry, so it is common to refer to *virial mass*, $\Delta = 200$, as the condition that separates the region of the halo that is in dynamical equilibrium from the surrounding region that is still collapsing. From this definition we also define the virial radius, r_{200}, is the radius with overdensity 200 times the critical value, and the enclosed mass M_{200}.

The halo mass function is the number density of haloes of different mass and was studied with the N-body simulations. The range of the mass of the haloes is between $10^8\ M_\odot$ (dwarf-size haloes) and $10^{15}\ M_\odot$ (cluster-size haloes).

The density distribution of haloes could be found through N-body simulations and match with observational data.

N-body simulations showed that the haloes, which are in equilibrium, have a nearly universal form, independently from halo mass, initial conditions and cosmological parameters. This density profile could fit with different density distribution.

In this way just two parameters are sufficient to describe the inner profile of the halo.

The most common profile is called Navarro-Frank-White (NFW profile) which is given by:

$$\frac{\rho(r)}{\rho_{crit}} = \frac{\delta_c}{(\frac{r}{r_s})(1+\frac{r}{r_s})^2} \tag{2.1}$$

where r_s is a scale radius, δ_c is a characteristic (dimensionless) density, $\rho_{crit} = 3H^2/8\pi G$ is the critical density. The parameters are equivalent to $M_{200} \propto \rho_s r_s^3$, the virial mass of the halo, and $c = r_{200}/r_s$, the concentration parameter.

Other profiles include supernovae mechanism and interactions between an active galactic nucleus and the interstellar medium which ejects gas; this mechanism could lead to a flattening of the central cusp and general equation to describe is:

$$\rho_{GNFW}(r) = \frac{\rho_0}{(\frac{r}{r_s})^{\gamma}(1+\frac{r}{r_s})^{3-\gamma}} \tag{2.2}$$

when $\gamma = 1$ we obtain equation 2.1.

One other profile uses three parameters and it is called Einasto profile:

$$\rho_{Ein} = \rho_0 exp\Big\{-\Big(\frac{2}{\alpha}\Big)\Big[\Big(\frac{r}{r_s}\Big)^{\alpha} - 1\Big]\Big\} \tag{2.3}$$

where α is the additional parameter with respect to NFW. The Einasto profile describes better than NFW profile the density distribution in a halo [83].

From some observation of dwarf galaxies and low-surface brightness galaxies it has been found that some objects are better described by flatter density profiles like the Burkert profile:

$$\rho_{Burk} = \frac{\rho_0}{\Big(1+\frac{r}{r_s}\Big)\Big(1+\frac{r^2}{r_s^2}\Big)} \tag{2.4}$$

The Burkert profile exhibits constant density for radii much smaller than the scale radius r_s.

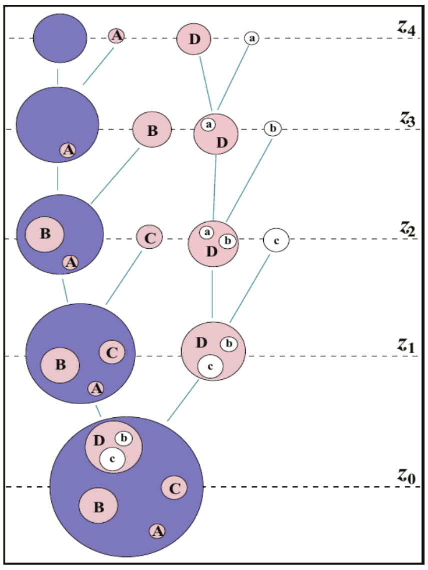

Figure 2.3: The tree scheme is a way to see the evolution of halo and the subhaloes.

We define a subhalo as a halo that has crossed the virial radius of a larger halo at some point in the past. In hierarchical model one halo can increase its mass merger other haloes like it is shown in the figure 2.3 [84].

The Aquarius project investigated on small scale the evolution of the halo carrying out high resolution dark matter simulations of Milky Way sized haloes in the ΛCDM cosmology [85].

Their resolution allows to identify region r_{50}[2] so it is possible to identify also substructures and substructures within the substructures themselves. Figure 2.4 shows different different generation of subhaloes: given a dark matter distribution in a cubic

---

[2] r_{50} is the radius with mean enclosed overdensity 50 times the critical value. It is common to use r_{200} which is the radius with overdensity 200 times the critical value.

region of side $2.5 \times r_{50}$ centered on the main halo it is possible to distinguish 6 subhaloes. Some of these subhaloes display other substructure of different generation. One of them shows subhaloes of fourth generation.

As we will see §2.2.1 the subhaloes with mass around $M^8\ M_\odot$ could be the first collapsed structures forming the oldest globular clusters.

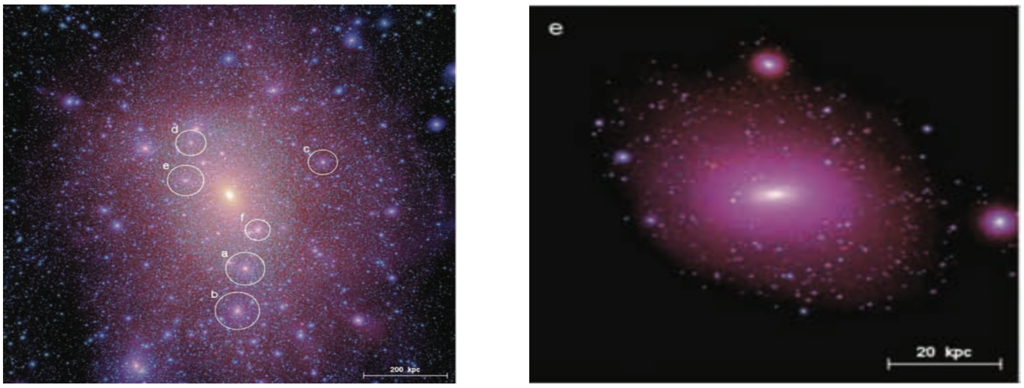

(a) DM Halo (b) Subhalo E

Figure 2.4: Images of substructures within substructure. (a) The DM distribution in a cubic region of side $2.5 \times r_{50}$ centred on the main halo is shown. The white circles mark the six subhaloes and they represent the first generation of substructures. (b) A zoom of the subhalo *e*. These subhaloes show inside a second generation of subhaloes: sub-subhaloes [85].

2.2 Globular clusters

A **globular cluster** (GC) is a spherical collection of stars that orbits a galactic core as a satellite. The system is gravitationally bound: this gives them their spherical shapes and relatively high stellar density towards their centers. The name of this category of star cluster is derived from the latin *globulus*, a small sphere.

The Milky Way has nearly 150 globular clusters (GCs) which are located following a roughly spheroidal distribution around the Galaxy and the space density of clusters is strongly concentrated toward the Galactic center: for radius $R < 10$ kpc the distribution decrease as R^{-3}, for $R > 10$ kpc as R^{-4}. However the majority of the GCs lie at low latitudes in the inner Galaxy within ~ 20 kpc from the Galactic center.

Although it appears that globular clusters contain some of the first stars to be produced in the galaxy, their origins and their role in galactic evolution are still unclear [86, 87]. GCs differ strongly from each other both in absolute magnitude and total mass: for example ω Centaury (NGC 5139) is the largest GC known inside the Milky-Way and shows an absolute integrated magnitude $M_V = -10.40$ and a total mass $M_{tot} = 5.1 \times 10^6 M_\odot$ [88], on the other side the faintest globular cluster $AM4$ has a $M_V = -1.82$ and a mass around (or less) $M_{tot} \sim 1000 M_\odot$ [89].

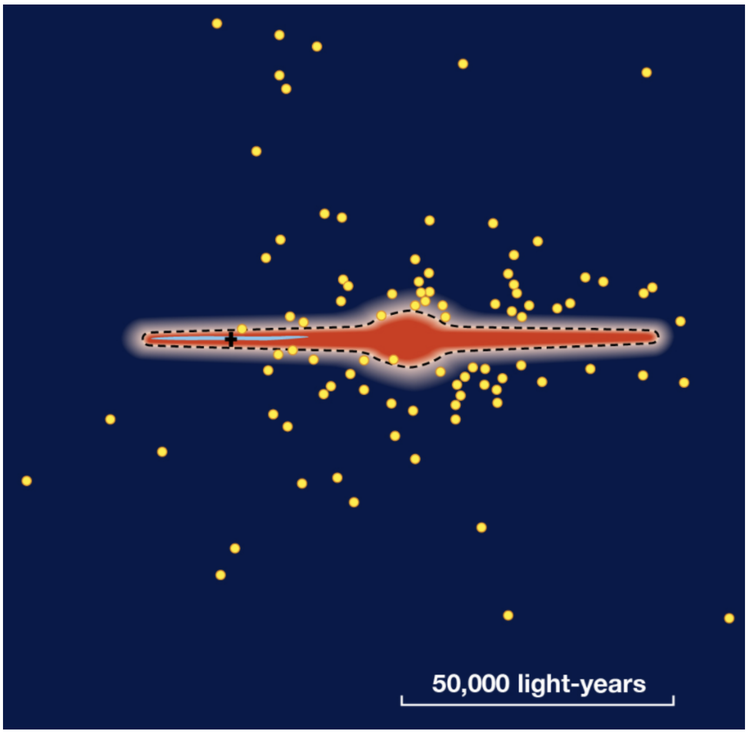

Figure 2.5: The region surrounded by the dotted line includes the Milky-Way disk and bulge structures. The cross on the left side of the galaxy shows the position of the Sun. The yellow small circle rapresents where the GCs are located. The image was taken from `https://www.britannica.com/science/globular-cluster`.

The first classification of GCs was done by Shapley, Swope and Helen Battles Sawyer. In 1927–29, Shapley and Sawyer categorized clusters according to the degree of concentration that each system has toward its core [90]. The GCs are classified in twelve classes which are indicated with Roman numerals [Class I-XII] and is known as the *Shapley–Sawyer Concentration Class.*

This classification is based on the morphology of the cluster but there are other parameters to distinguish the GCs and understand their properties. From the spectrometer is it possible to separate the GCs in two different groups based on the chemical composition of the stars. Generally GCs are constituted by stars of Population II which have a low ratio of elements other than hydrogen and helium when compared to Population I stars such as the Sun. As written §1.7.1 H and He have cosmological origin while the other elements are created inside the stars during their evolution, and by *slow processes* (s-process) and *rapid processes* (r-process) in supernovae and other cataclismic events. The proportion of metals (every element heavier than He) can be an indicator of the age of a star, with older stars typically having a lower metallicity. The astronomer Pieter Oosterhoff observed that there appear to be two populations of GC which are called *Oosterhoff groups*: both groups have weak lines of metallic elements but the type I (OoI) cluster is not quite as weak as those in type II (OoII). Hence, type I are referred to as "metal-rich" (MR) ($\langle[Fe/H]\rangle \sim -0.5$) while type II are "metal-poor" (MP) ($\langle[Fe/H]\rangle \sim -1.5$).

From the colour of the stars it is also possible to place them on the Hertzsprung-Russell diagram (HR-diagram). As the position of each star in the HR diagram varies with age, the shape of the curve for a globular cluster can be used to measure the overall age of the star population. The standard candles to compute the distance and age are red giant branch stars, horizontal-branch stars, RR Lyrae variables, main-sequence subdwarfs, white dwarfs [91]. The last evaluations indicate that the MR GCs mean ages of 11.5 Gyr and it means that they are formed at $z_{form} = 2.9$ and the MP ages of 12.5-12.8 Gyr, is equivalent to say that they are formed at $z_{form} = 4.8 - 5.9$. This would place GC formation around the time of the reionization, and continuing after the epoch of reionizaton (§1.6).

The present-day appearance of a GC is a complicated convolution of the initial conditions of its formation with subsequent internal and external dynamical effects. Indeed, the original mass may be largely different from the current mass. Baumgardt et al. [92] exploited the Gaia DR2 data to estimate both distances and 3-d motion of the clusters, and then they compared the observational data of the surface luminosity and internal velocity distribution and N-body computations. Baumgardt et al. studied 154 GCs, including M15, and they showed that the fraction of FG stars depend on the initial mass of the cluster.

It is possible to define the internal spherical structure of the GCs defining some standard *radii*. These are the *core radius* (r_c), the *half-light radius* (r_h), and the *tidal* (or *Jacobi*) *radius* (r_t). The radius r_c is the distance at which the apparent surface luminosity has dropped by half. The radius r_h is the only one of these three radii that is relatively unaffected by dynamical evolution and can serve as a probe of GC formation conditions. The radius r_t is the distance from the center of a cluster where the gravitational acceleration due to the cluster equals the tidal acceleration of the parent Galaxy [93]. This radius depend where the GC is located and the equation is

$$r_t = R\left(\frac{M}{2M_g}\right)^{1/3}$$

.

At the end it is necessary to define the parameter *concentration ratio* like $c = r_t/r_c$. This is the case for the empirical King profiles and dynamical King models (see §2.2.2).

2.2.1 Globular Cluster Formation

How globular clusters were formed is still under discussion. In many globular clusters, most of the stars are at approximately the same stage in stellar evolution, suggesting that they formed at about the same time.

Where the globular clusters were created is an open question because the presence of two classes, MR and MP GCs and their different spatial distribution, suggests that each class was formed in a different place under different conditions. The current idea on the formation of the galaxies is that the galaxies passed through two phases: an initial *in-situ* phase of formation followed by mass growth via an *ex-situ* (or accretion) phase [94]. The galaxies should contain contributions from both in-situ and ex-situ formed GCs depending on the galaxy's assembly history. Although there is not a clear separation between the two phases, nowadays it is common to believe that the MR GCs were formed in-situ in a massive galaxy, while the metal-poor GCs were acquired in the dissipationless accretion of neighboring lower-mass galaxies [95, 96].

It is possible to divide the formation of the GCs in two different class: classical scenarios and cosmological scenario.

Classical scenario In this scenario the GCs are the natural outcome of star formation in high red shift galaxies.

The young massive clusters (YMCs) with masses and radii very similar to GCs are observed to form in gas-rich environments of high star formation rate and gas pressure. The common hypothesis is that the GCs may be the high-redshift equivalent to the YMCs forming in the local Universe that have survived for a Hubble time [97]. The conditions in gas-rich galaxies at high red-shift are favourable to GCs formation because the high turbulent preassure leads to a high fraction of star formation in gravitationally bound systems and, also to increase the mass scale for gravitational collapse, forming globular massive clusters (GMCs). The merger mechanism leads to the formation of new MR GCs.

At high redshift ($z > 1$) the rate of the galaxies merger is higher than now ($z = 0$) and this process could facilitate the assembly of very large GMCs.

Cosmological formation The analysis of the perturbations using the Jeans theory shows that the first bound structures have the dimensions given by Jeans length (λ_l) and Jeans mass (λ_M) $\simeq 10^6 M_\odot$), like the dimension and characteristic of the globular clusters [98]. The recent studies focused on the formation of the GCs within DM minihalos characteristic virial mass $M_{DM} \simeq 10^8 M_\odot$ [99, 100]. There are a lot of models and all those models are based on fundamental physical process which happened in the early Universe, at a time when the conditions for star formation were substantial different compared at low red shift, in a ΛCDM environment.

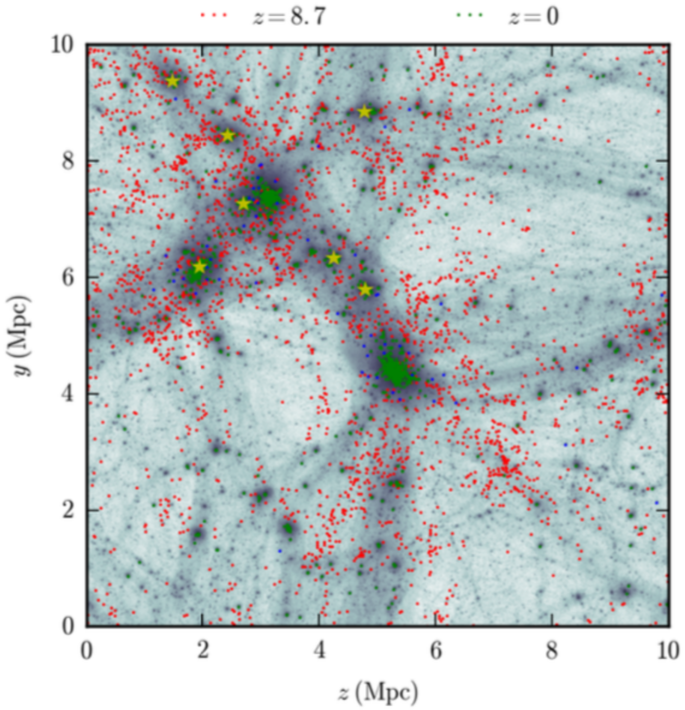

Figure 2.6: From N-body simulation it is showed both the GCs candidates positions at $z = 8.7$, marked in red dots, and the most bound particles at $z = 0$, marked in green dots. The blue dots denote structures that are still the most massive in their host halo, the yellow stars indicate the selected halos of the MW and the background shading indicates the density of the DM at $z = 0$ [99].

Unfortunately in a system composed with galaxy host, dark matter halo and sub halos, and the globular cluster and stars present in the halo, the tidal force is able to destroy both the dark matter substructure and sub halo around the galaxy and the GCs which are close the center. The tidal force is a function of the radial distance so the majority of the halos containing GC formation sites merge with the central halo by present day but some could survive in separate haloes at a range of distance [101, 102]. When a GC with a dark matter halo evolves in a tidal field, their simulations indicated that it loses either most (for an NFW halo) or nearly all (for a Burkert halo) of its dark matter [103, 104].

For in situ GC streams, the resulting phase-space distribution of stars (inside the host galaxy) will depend only on the gravitational potential of the host, the initial mass and core radius of the GC, and its orbit inside the Galaxy.

2.2.2 Dynamics of Globular cluster

Globular clusters are in equilibrium with a spherical star cluster configuration, bound by its gravity. Even though the number of the stars inside the core is high, their orbits change slowly. One important timescale is *crossing time* which is defined as the time an object needs to cross all the system and in an uniform sphere with mass M and radius R it is given by:

$$t_{cross} = \sqrt{\frac{3}{4\pi G\rho}} \tag{2.5}$$

We define the *relaxation time* as the measures of the time necessary for stars in a system to lose completely the memory of their initial velocity. Suppose that we have a cluster of radius R and mass M, made up of N stars with mass m, moving with a mean velocity V

$$t_{relax} = \left(\frac{R^3 N}{Gm}\right)^2 \frac{1}{8 ln\Lambda} \tag{2.6}$$

where the term Λ is defined as the ratio between the radius R and the radius r_{min} and the term $ln\Lambda$ is called **Coulomb logarithm**. In the classical scattering theory the term r_{min} is plays the role of the impact parameter b_{min} for 90° scattering between particles 1 and 2. It is possible to demonstrate that for a great number of stars the term Λ tends to the number of stars N. Given the number of the objects inside a system and the dimension of the system self, it is possible to compute both the t_{cross} and t_{relax} and the two timescales are linked through:

$$t_{relax} = \frac{0.1N}{lnN} t_{cross} \qquad (2.7)$$

For a galaxy with number of stars $N = 10^{11}$ the $t_{relax} = 10^9 t_{cross}$. The age of the galaxies is around $t_{age} = 10^{10}$ years while the $t_{relax} >> t_{age}$ so the galaxies can be treated as *collisionless* system.

Vice versa the system like globular clusters or dense young star clusters have the $t_{relax} \sim t_{age}$ and in that case we should treat that system like *collisional* system. Since the t_{relax} tends to delete the initial conditions so the hypothesis about of the globular clusters formation are modeled in a range of different initial conditions, like as explained before [105, 106].

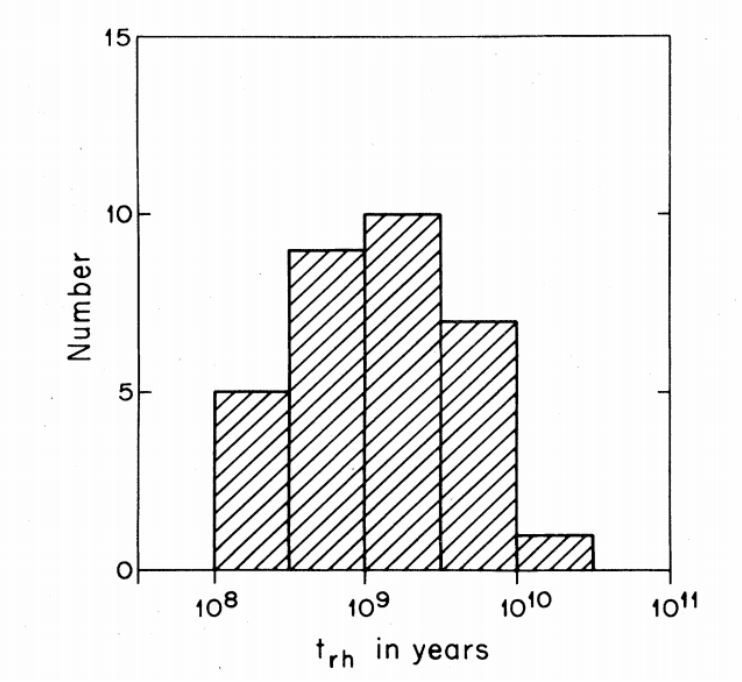

Figure 2.7: This histogram shows the t_{relax} computed for 32 GCs [105]

The first stage of the dynamics of the GC is called *violent relaxation* and this occurs when the potential changes on timescales are comparable to dynamical timescale. In this phase the cluster is not in equilibrium, the energy of a single star is not conserved, and it will undergo macroscopic oscillations on a rapid dynamical timescale t_d [107]. Lynden–Bell [108] used the statistic to describe this process and showed that, during the collapse, the random velocities of the stars in the inner parts of the cluster may achieve a nearly Maxwellian distribution. The stars which are located in the tail of that distribution, the stars with major velocity, could to escape in other spheres, defined in the phase space, in a time t_d. It is important that the violent relaxation changes the energy of the stars independently of their masses.

After this phase with fluctations with period $P \sim t_d$, the system goes towards a statistically probable state and there is an equipartition of energy per unit mass.

So the system tends to equilibrium and this leads to energy equipartition among the different stellar groups:

$$\frac{1}{2}m_1v_1^2 = \frac{1}{2}m_2v_2^2 = ... = cost \tag{2.8}$$

where the subscripts (1,2,...) correspond the different star populations, each one with an own mass. Two-body encounters tend to equalize the random energies between stars, transferring energy from massive stars to light stars. If the total mass of the heavy stars is smaller than the total mass of the light stars, the heavy stars settle to the center of the cluster, but the central potential is still dominated by the light stars, and the two populations reach equipartition. But if the central potential becomes dominated by heavy stars before equipartition between the two popolation of stars, the density of heavy stars in the core continues to increase. Eventually all but a few of the light stars are expelled from the core, and energy transfer ceases. This process should be accomplished in one relaxation time.

Some light stars which have gained enough kinetic energy can to be ejected from the cluster entirely. This process is called *evaporation* and can be more emphasized if the GC is under the tidal effects by the Galaxy.

A self-gravitating isothermal gas sphere, contained by a rigid shell, may attain a stable hydrostatic equilibrium. If the ratio of central to outer densities $D = \rho_c/\rho_e$ is greater than ~ 710 the system goes towards the **gravothermal collapse** in less time of the t_{relax} [109]. When this gravothermal instability occurs, the central region of the cluster becomes densely crowded with stars and the surface brightness of the cluster forms a power-law cusp. The gravothermal collapse is similar at the core collapse in the stars: the core is in isothermal configuration and its mass grows until the *Atonov limit*, so called because originally Anotnov was the first to discover this instability. The collapse will stop when it will create the binary sistem [107].

The core density determines the interaction rate in the core. The system binary-single (BS) and binary-binary (BB) generate energy in the core and could stop the contraction [110].

The GCs can split into two groups: the GCs which show a "core collapse", in general, can describe a power-law slope in their density profiles near the center; the GCs that show a non core-collapsed are well described by a King profile and show a clear flat part near the center.

The core collapse leads to increase the density of stars and their interactions. Since a massive black hole, with mass $\sim 10^3 M_\odot$ may form as the end product of core collapse in spherical stellar systems and also in this case the profile of density can show a cusp like in figure 2.8 [105, 111].

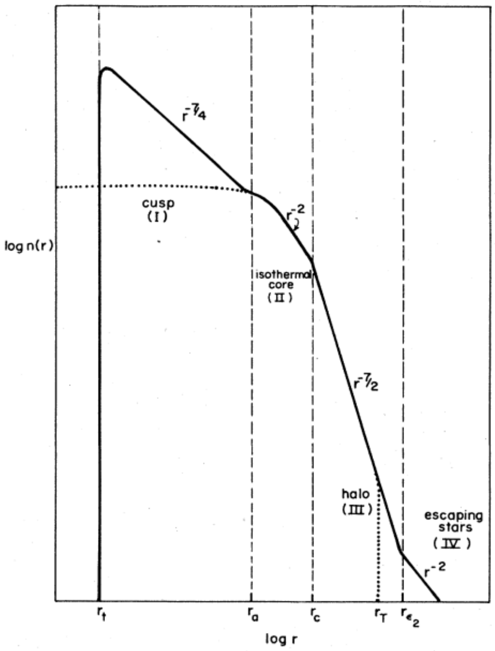

Figure 2.8: In an isolated spherical cluster, the stellar density as a function of the radius in presence of a massive black hole which is located in the center of the GC. Without it the isothermal core extends from $r = 0$ to the r_c with a $\sim$ flat profile, so no cusp is shown (dotted line) [105].

The presence of an IMBH modifies the distribution of baryonic matter but also the dark matter because the IMBH could induce an overdensity called *spike*, or lighter overdensities, called *mini-spikes* and the density of the spike follows that equation:

$$\rho_{DM}(r) \begin{cases} 0 & r < 2R_S \\ \frac{\rho_{sp}(r)\rho_{sat}}{\rho_{sp}(r)+\rho_{sat}} & 2R_S \leq r < R_{sp} \\ \rho_0 \left(\frac{r}{R_{sp}}\right)^{-5} & r \geq R_{sp} \end{cases} \tag{2.9}$$

where R_S is the Schwarzschild radius, R_{sp} is the radius of the spike, ρ_{sat} is called saturation density and it is the maximum density for DM considering the self-annihilation, ρ_{sp} is the profile density of the spike, normalized at ρ_0 and their distribution is given by:

$$\rho_{sat} = \frac{m_{DM}}{\langle \sigma v \rangle t_{BH}} \qquad \rho_{sp} = \rho_0 \left(\frac{r}{R_{sp}} \right)^{-3/2} \tag{2.10}$$

Inside the equation 2.10 appear the masses of the DM particles and their cross section. Those profiles were computed simulating the dark matter density profile in the region where the black hole dominates the gravitational potential [112] and also to understand the $\gamma-$ray signal coming from the GC 47 Tuc [2].

Some attempts try to associate the signal in X-ray and radio band with the presence of IMBH but until today there is no conclusive evidence for their existence [3].

2.3 One particular globular cluster: M15

M15 is the perfect prototype of core collapse globular cluster. Until now around 20% of the globular clusters show a core collapse profile [113].

M15 was the subject of one of the first CCD studies of globular cluster stars. Since the first works on the color-magnitude diagrams (CMD) on its population of stars, M15 appears with a steep giant branch and heavily populated blue horizontal branch (HB): this means that this GC is very metal poor with a ratio $[Fe/H \sim -2.1]$.

The core of M15 has been resolved by the Hubble Space Telescope (HST) and also the Canada-France-Hawaii Telescope (CFHT) taking B and V CCD images. Durrell and Harris [114] analysed the CMD of the stars from CCD data. They used isochrone fitting, the main-sequence subdwarf sequence, and HB models and obtained a distance equal to

$$d = (10.4 \pm 0.8) \quad \text{kpc} \tag{2.11}$$

N-body simulations produce IMBHs from core-collapsing high-mass stars during the early stages and it is possible that in some other GCs there have been kinematic detections of IMBHs like in $\omega-$Centauri [115], in NGC6624 [116], or 47 Tucanae [117].

Gersen et al [118] using the Space Telescope Imaging Spectrograph (STIS) on HST obtained high spatial resolution spectroscopy of the central region of the dense globular cluster M15. They studied the motion of the stars in very few arcsecond and obtained a higher σ_{rms} than in previous work, where rms is the root mean square velocity averaged over rings on the projected plane of the sky. This can be explained with a high concentration of dark remnants (neutron stars, white dwarfs) inside the core.

Astronomers explained that the velocity could be radially anisotropic near the center contradicting the predictions from Fokker-Planck equation and the N-body simulations. The presence of an intermediate-mass black hole which has a mass equal to $M_{BH} = (3.9 \pm 2.2) \times 10^3 M_\odot$ in M15 appears to be the most plausible explanation of the data.

The same authors quote also that dynamical models that have been constructed for M15 remain idealized: Jeans models are based on exact hydrostatic equilibrium while the results of Fokker-Planck equation are influenced by the stellar evolution.

Successively van den Bosch et al [119] studied the ratio M/L in the core of M15. They use Martin Schwarzschild's method [120]. This method is divided in four steps: choice the density of the object from the data dividing the space in N cells which are sign with the letter J, computing the potential for each cells through Poisson's equation, given a potential it is possible to compute the orbits of the stars signed with I inside that cell defining a number $B(I, J)$; then it is possible to add effective integrals if the orbit crosses other orbits in other cells and, at the last step, it is necessary to reproduce the density distributions using the model of density in the first step. This method was used by van den Bosch to estimate the density profile of M15. The model is a function of the distance, inclination, the M/L ratio in different bins, and central dark mass M_{DM}.

The best fit for their results given the value of those parameters:

- $d = (10.4 \pm 0.4)$ kpc (68.3% confidence), in good agreement with the Durrell and Harris' work;
- the best-fitting inclination is $60° \pm 15°$ (68.3% confidence);
- the best fit about the ratio M/L is shown in the figure 2.9. Error bars mark the 68.3% confidence;
- given the M/L profile it can be deduced a $500^{+2500}_{-500} M_\odot$ of dark mass in the core. Inside the inner $1''$ the central M/L peak and the dark central mass together represent a mass of $3400 M_\odot$.

Successively den Brok et al [1] examined the same data set but with a different approach: their fitting method maximizes the likelihood for individual stars and, as such, does not suffer the same loss of spatial and velocity information incurred when spatially binning data or measuring velocity moments.

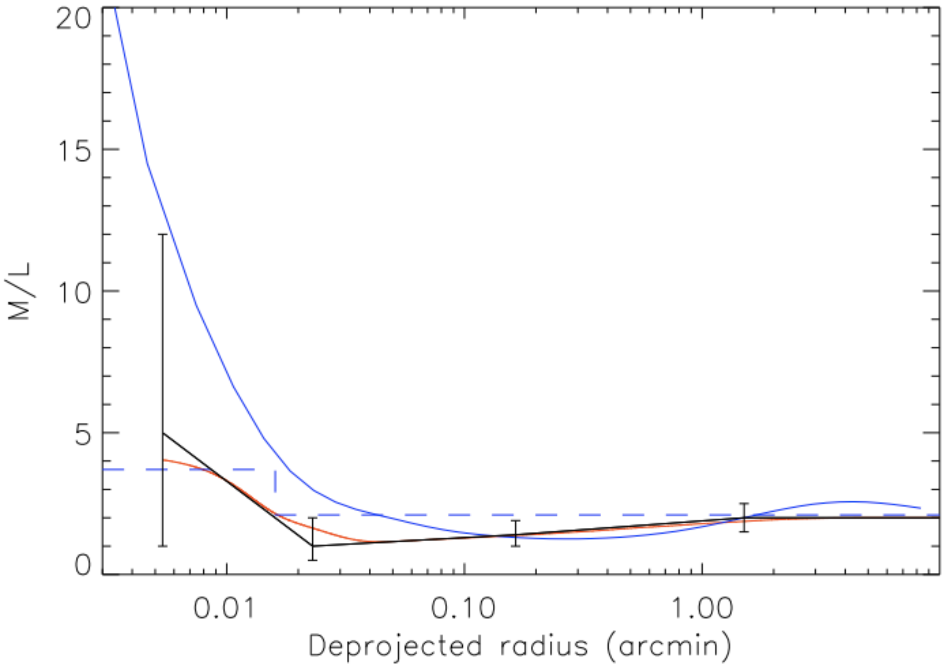

Figure 2.9: Radial M/L Profiles. The black line with the error bars is the best V.Bosch's fit. The red line is the best-fit of deprojected M/L profile. The blue solid line is the deprojected M/L profile from H. Baumgardt and the dashed line shows the Pasquali's profile [119].

Indeed they do not divide that quadrant into radial shells, they use the likelihood for every single star compared on the second moment of the velocity from Jeans model.

Considering N stars, indicated with the subscript i, every star has coordinates $\bar{x_i'} = (x_i, y_i)$ and velocity $\bar{v_i} = (v_x \pm \sigma_{xi}, v_y \pm \sigma_{yi}, v_x \pm \sigma_{yi})$ where x is the coordinate of the projected major axis of the porbit, y is the coordinate of the projected minor axis and z is the direction of the line of sight [121].

Given a set of models the quest it is to know which is the best model to describe the data set. For the model j the likelihood is:

$$\mathcal{L}_{ij} = p(v_i | x_i', S_i, \Theta_j)$$

where S_i is the error matrix and Θ_j is the parameters of the model j. In this way the likelihood is a convolving the distribution predicted by the cluster model with a Gaussian distribution representing the observed velocity and its uncertainty, as shown in the figure 2.10.

The likelihood is given by:

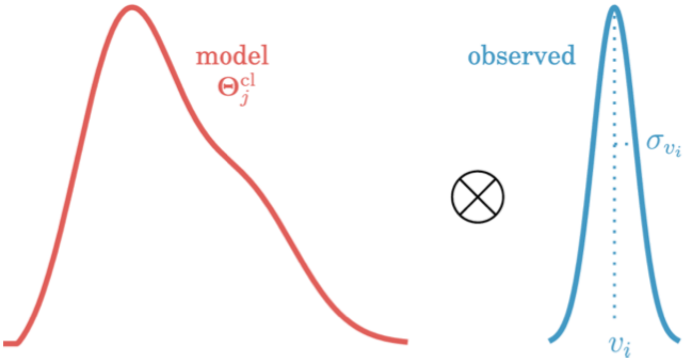

Figure 2.10: On the left the red line shows the velocity distribution generated by model with parameters Θ at the position of the i star. The blue line on the right is the measurement of the same star: the gaussian distribution has $\mu = v_i$ and uncertainty $\sigma = \sigma_{v_i}$. The likelihood must convolve both the distributions [121].

$$\mathcal{L} = \frac{1}{\sqrt{2\pi(\overline{v_{i,mod}} + \delta v_i)}} exp\left(-\frac{1}{2} \frac{v_i}{\overline{v_{i,mod}}^2 + \delta v_i^2} \right) \tag{2.12}$$

where the $v_i \pm \delta v_i$ is the observed velocity for a star togheter with the uncertainty, $\overline{v_{i,mod}}$ is the second velocity moment derived from the Jeans model.

This method gains in the spatial resolution towards the center of the cluster. The team used two independent data sets: one contain the measured line-of-sight (LOS) and the other use the proper motion (PM) of 1764 stars from HST images. The LOS data indicate that $> 80\%$ of the mass is located within the central 1.5 arcmin, considering that the data extend till 15 arcmin, while the PM data cover the central 0.3 arcmin.

The dynamical M/L profile, which is measured in the V bands, is shown in figure 2.11

The increase of M/L towards the centre confirms the idea that the centre of the cluster is dominated by relatively dark object like neutron stars, black holes, white dwarfs, dark matter or a IMBH, or combinations of those. The best model fitting with the data considers the presence of a dark central mass with $M_{DC} = 2367 \pm 987 M_\odot$. If this mass is constituted by one intermediate black hole, it is necessary to take measures of few Schwarzschild radii from the black hole. The sphere of influence of a black hole is given by:

$$r_{BH} = \frac{GM_{BH}}{\sigma^2} \simeq 0.07\text{pc} \quad \simeq 0.023\text{arcmin}$$

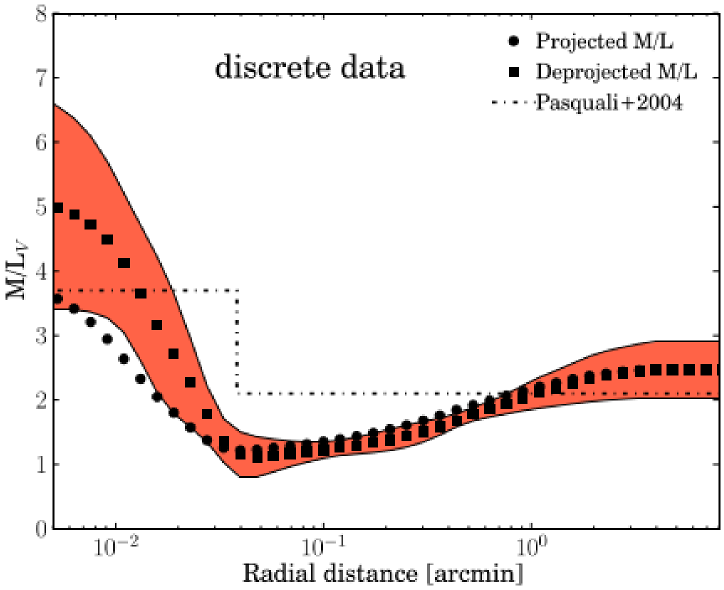

Figure 2.11: The mass-to-light (M/L) profile of M15 as a function of radial distance from its centre from the discrete data. The red area indicates the 1σ confidence interval for the deprojected profile while the black circles represent the data of projected M/L [1].

where M_{BH} is the mass of the black hole and σ is the stellar velocity dispersion and G is gravitational constant. the models that take into account the black hole decouple from those that do not take it into account approximately at $r = 0.015$ arcmin (as shown in figure 2.12).

At that range of radius it is not possible to resolve far enough inside to distinguish between a point-like mass and a smooth mass distribution. In figure 2.13 is shown the inferred density profile. In the same figure there are displayed both the density of stellar remnants profile from N-body simulations, indicated in dashed line, and the inferred density which derives from the best fit model. The two profile have the same slope and fit very well until $\sim 10^{-2}$ arcomin. In the outskirts region the main contribute to the mass density is given by main-sequence stars. In the center the black hole is assumed to be a point source, it does not show up in the density plot. The current resolution in the centre is too low and suggests that the inferred black hole mass might be a consequence of poor sampling of the density profile in the central parts. The high peak of mass density in the central region, which is in an agreement with theoretical predictions, does not provide evidence for the presence of an IMBH in M15.

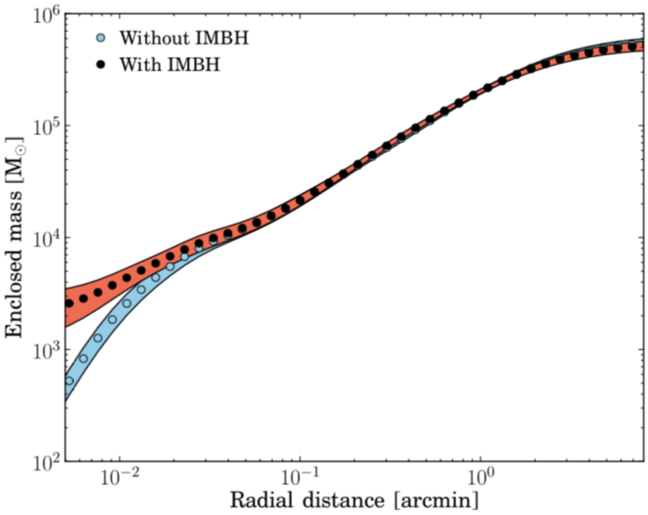

Figure 2.12: Enclosed mass of M15 both with the black hole (closed circles and red area), and without black hole (open circles and blu area). The two models do not differ beyond 0.015 arcmin [1].

2.4 M15 in high energy range

The high number of stars positioned in a small volume of a few parsecs is a sufficient condition for interactions and collisions between them to occur often.

Due to these chance encounters, some exotic classes of stars, such as blue stragglers, millisecond pulsars and low-mass X-ray binaries, are much more common in globular clusters.

M15 was observed in different ranges of energy: from radio to γ-rays. Especially in radio waves and X-ray ranges was discovered that M15 hosts eight known pulsars and two low mass X-ray binaries [123]. Four of the other seven pulsars are located in close proximity to the cluster core, within < 4.5 arcsec (corresponding at 0.2 pc).

It is important to highlight that the presence of a IMBH could detect both in the radio waves and also in each electromagnetic band. The absence of the X-ray from the center allows us to put an upper limit on the mass of the black hole [3].

The last works on the electromagnetic emission from M15 could put an upper limits on the mass of the IMBH equal to $500M_\odot$ within the 3σ of detection.

---

[3] The presence of the X-rays, which are emitted from a black hole, indicates that there is a hot plasma around of the black hole.

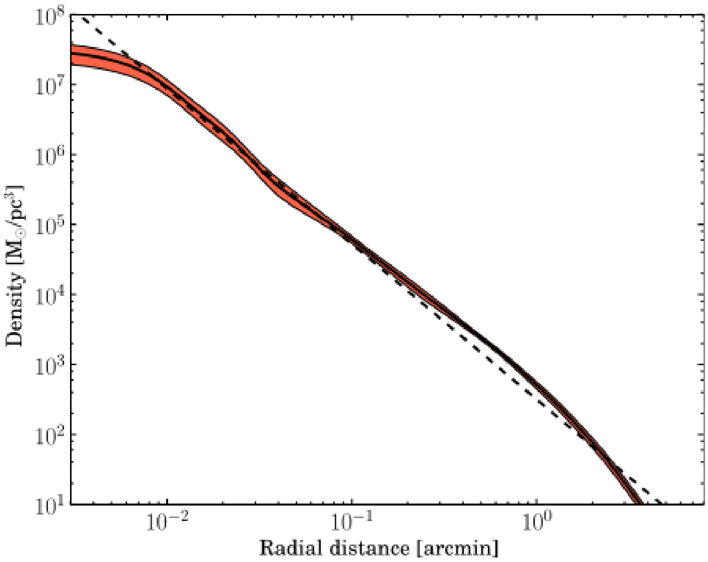

Figure 2.13: The inferred density profile of M15 as a function of the radial distance from the center of the source. The solid black line is the density profile while the red region is 1σ errors. The dashed line is the expected density profile of stellar remnants from Baumgardt et al.[122]. The picture is taken from [1].

In the range of γ-rays, M15 was studied from Fermi LAT, Whipple and successively H.E.S.S, and MAGIC.

Fermi-LAT The Fermi Gamma-ray Space Telescope was launched on 2008 June 11. The Large Area Telescope (LAT) is modular, consisting of a 4 × 4 array of identical towers and every tower is composed by tracker, calorimeter and data acquisition system. The goal of the telescope is to collect γ-rays in the energy range from about 20 MeV to above 500 GeV. The third Fermi-LAT source catalog (3FGL) includes 3033 sources above 4σ significance in the 100 MeV–300 GeV range [124]. A high fraction of the pulsar which were detected by Fermi are located inside the GCs.

M15 was observed with the Fermi-LAT and the Zhang P.F. et al [125] analyzed the data taken in 7 years. The results on the analysis on M15 is reported in figure 2.14: the best fitting model is a power-law model with an index $\Gamma = 2.84 \pm 0.18$, the maximum value on the TS maps is equal to 49 and corresponds to a detection significance of 7.0 σ, the integrated photon flux above 100 MeV is $F = (11.84 \pm 2.48) \times 10^{-9}$ cm^{-2} s^{-1} and the energy flux is $E = (4.15 \pm 0.65) \times 10^{-12}$ erg cm^{-2} s^{-1}.

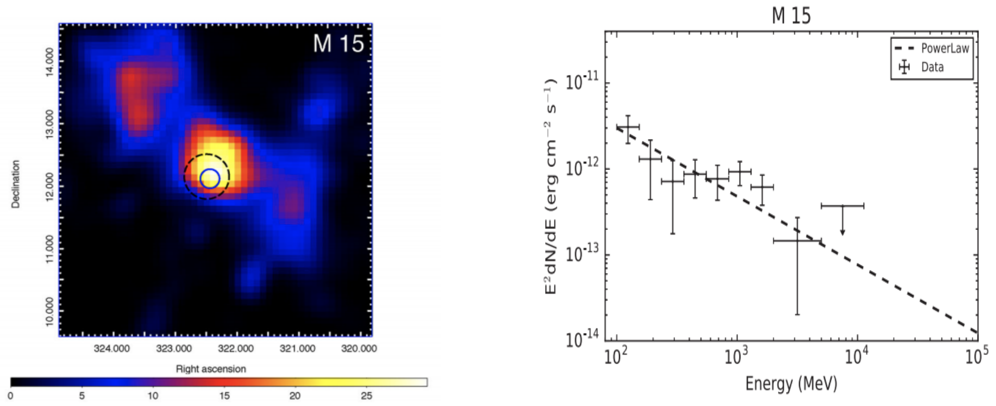

(a) Sky map

(b) Spectral Energy Distribution

Figure 2.14: (a) TS maps of dimension 5° × 5° of M15. The blue solid circles is the best fit and its radius at 1σ level of confidence. The dashed circle is the tidal radius. (b) Spectral energy distribution of M15: the dashed line indicate the best-fit spectral model [125].

MAGIC observation M15 is the only GC discovered by Fermi-LAT at energies up GeV $\gamma-$rays, located in north hemisphere where it is possible to observed at low zenith angles from La Palma. The data were collected in two years (2015 and 2016) in the period from June to September for each year.

In that period MAGIC collected data for 173 h of observation at low Zenith distance (the mean is $Zd = 20.81°$) to ensure a low energy threshold. MAGIC collaboration analysed the data with the standard MAGIC analysis and the results were reported in a paper [126]. About one third of the selected data set was taken under non-perfect atmospheric conditions (mostly due to *calima*, a dust wind from the Sahara desert, which affects part of the MAGIC data taken during summer). That part of the data set has been corrected using simultaneous LIDAR measurements. In this way 165.20 h were good to be analysed and the results are shown in figure 2.15(a) and figure 2.15(b).

The obtained upper limit on the integral flux above 300 GeV is equal to 3.2×10^{-13} cm^{-2} s^{-1}, which corresponds to $< 0.26\%$ of the Crab Nebula flux. The results by the MAGIC observation showed that there are not signal at very high energy and the collaboration used that limits to compare with the predictions of the model in the article [127].

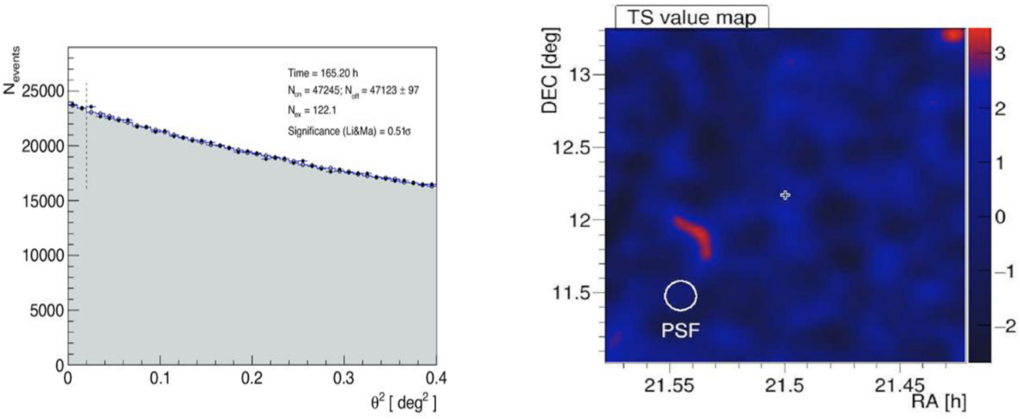

(a) M15 θ^2 plot

(b) M15 Sky map

Figure 2.15: (a) The θ^2 plot for the MAGIC observations of M15, taken from [126]. The source is located at 0 on the *x-axis*, the fill dots are the ON events while the grey area is the background. (b) TS sky maps of M15. The TS value is applied on the background and corresponds to a significance of an excess at a given location in the sky. The cross in the center indicate where is the source M15 [126].

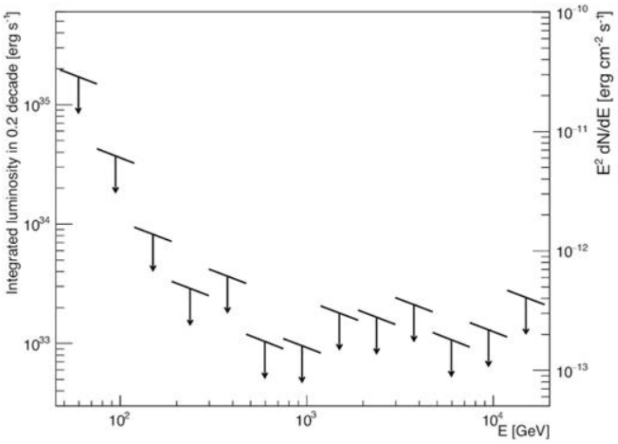

Figure 2.16: In this plot are shown the upper limits both on the $\gamma-$ray luminosity density from the GC M15 (*y-axis* on left) and on the $\gamma-$ray flux density (*y-axis* on right), the *x-axis* is the energy in the log scale [126].

Chapter 3

Cosmic rays and gamma-rays

The term *cosmic rays* (*CRs*) was coined by the American physicist Millikan in the 1920's, and refers to all the particles of extraterrestrial origin that constantly hit the Earth.

Cosmic rays were discovered by Victor Hess in 1912. He performed a lot flies with balloons and electroscopes so he could measure the radiation at altitudes up to 5.3 km and the level of radiation detected at 5 km was about twice that at sea level [128].

In the early twentieth century it was commonly believed that the radiation came from the ground. However, conflicting results to this common hypothesis emerged first from physicists Wulf and later Pacini. Hess' experiments demonstrated the existence of radiation from the sky, and explained the anomalies in the results of the two previous physicists. Furthermore, Hess' balloon flights made during solar eclipses showed that the radiation flux did not vary significantly, thus indicating that the Sun could not be the primary source of this radiation but, on the contrary, it must have come from space. From this revelation the term **cosmic ray** was coined.

Thanks to the discovery of the existence of cosmic rays, Victor Hess won the Nobel Prize in 1936, together with Carl David Anderson. Carl David Anderson, who studied the tracks of cosmic ray particles in a cloud chamber, in 1932 discovered a positively-charged particle with a mass seemingly equal to that of an electron. Anderson's particle was the first antiparticle proven by experiment and was named a ”positron”.

With the discovery of cosmic rays, the physics of elementary particles was born. This made possible to reach energies, until then inaccessible, which allowed the study of particles that were created during interactions. Hence, around 1950, the first particle accelerators were built. These accelerators allowed a ”cosmic ray”, with the configuration required by the study that had to be carried out. The most powerful accelerator today, which manages to supply the largest energy to the particles is the Large Hadron Collider, located at CERN in Ginevra. In spite of this, its maximum energy is still much lower than the energy of the most energetic cosmic rays.

With the most powerful cosmic rays it is possible to study the physics at extreme energies and to expand our knowledge in physics at highest energy.

Even if we have expanded our knowledge and made progressive advances in physics, some of the best questions remaining without answer are:

- are the supernovae shocks the mechanism of acceleration inside our Galaxy?
- Are galactic mechanisms able to accelerate the CR till 10^{20} eV?
- What are the extragalactic mechanisms able to accelerate the CR at 10^{20} eV?
- Is the antimatter produced in secondary rays only or are there the primary rays composed by antimatter?
- Is it possible to detect, directly or indirectly, dark matter and understand its nature?
- Is the proton really stable?

Nowadays, analyses of different fields have crossed over giving a global vision of the various cosmic sources. Since 14 September 2015, when the LIGO experiment detected the first gravitational wave, it added a new kind of messenger to complete the painting of the events [129].

3.0.1 Cosmic ray spectrum

The energy of CRs covers a wide spectrum: it starts at few MeV and reaches up to 10^{20} eV. It is possible to draw the flow of particles arriving on Earth with the energy they possess. The result is shown in figure 3.1 and is called the *cosmic ray spectrum*. The flux of cosmic rays depends on their energy: the more the energy of the particles increases, the more the flux decreases.

It has been observed that the flux decreases following an empirical power law:

$$\frac{d\phi}{dE} = A \cdot E^{-\alpha} \tag{3.1}$$

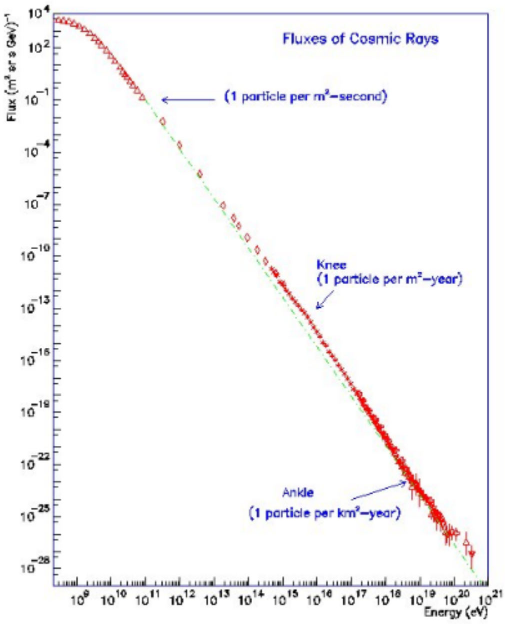

Figure 3.1: Flux of the cosmic ray as function of the energy.

In a double-logarithmic representation, the power law in equation 3.1 is represented by straight lines:

$$log\left[\frac{d\phi}{dE}\right] = log[A] - \alpha \cdot log[E] \tag{3.2}$$

where the constant A determines the intercept between the flux and the $y-axis$ and the spectral index α is the *slope* of the line. By following the line it is possible to recognize changes in slope and each bending point is possibly due to a variation in the production characteristics of the primary cosmic rays.

The solar magnetic field blocks most of the particles coming from outside the solar system below 1 GeV, therefore CRs below this energy are of solar origin. At this energy, the flux is influenced by the solar cycle; in the period with high solar activity the flux of low energy particles decreases while the flux is at maximum during the phase of low solar activity. This variation of the flux is called *solar modulation* [130, 131]. For this reason it is usually assumed that the cosmic ray spectrum starts above 1 GeV.

The first energy range that we consider covers the energy from around 1 GeV to $\sim 10^{15}$ eV. At that energy, the slope changes and this point is called *knee*. So, in the range until *knee* the spectral index α has a value equal to 2.7

and the equation of the flux becomes:

$$\frac{d\phi}{dE} = 1.8 \times 10^4 \cdot E^{-2.7} \tag{3.3}$$

It is important to notice that there are some differences between the energy spectra of different elements. The flux moves down and right for heavier and heavier cosmic rays, as it is shown in figure 3.2.

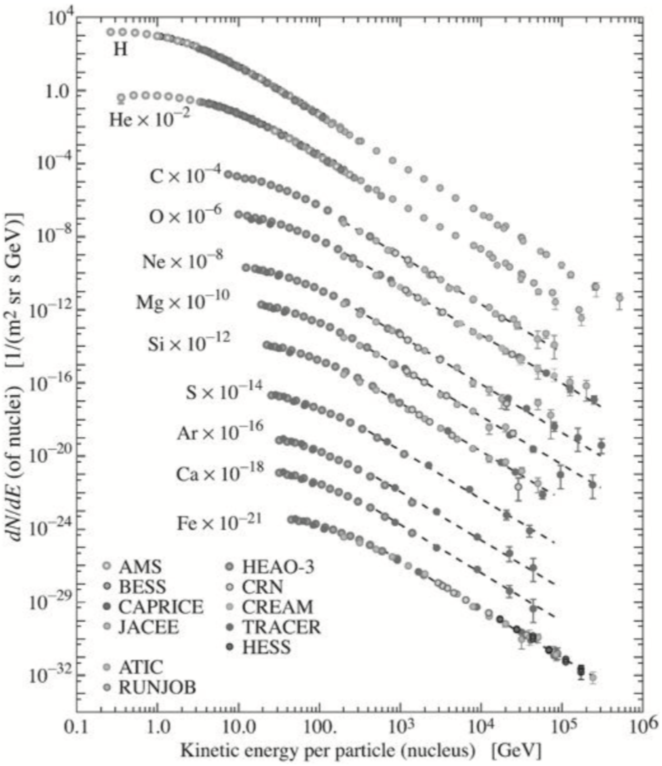

Figure 3.2: The differential energy spectra of different cosmic ray species as a function of kinetic energy [131].

It is possible to notice that the spectrum index has the same value for every kind of nuclei ($\propto E^{-2.7}$) but the value of the constant A changes for each element. The spectrum of cosmic rays is constituted of electrons and positrons as well, however these are not reported in figure 3.2 because their behaviour is different; in this case until $\sim$ 10 GeV the spectrum is strongly influenced by the effects of solar modulation. Over that energy the electrons are free from these effects and the spectrum is described by:

$$N(E)dE = 700E^{-3.3}dE \quad \text{particles m}^{-2}\text{ s}^{-1}\text{ sr}^{-1} \tag{3.4}$$

Figure 3.3 shows the spectrum by the experiment Dark Matter Particle Explorer (DAMPE) and other experiments. The electrons lose their energy with different processes: ionization in the interstellar gas, bremsstrahlung energy losses, synchrotron and inverse Compton [132, 133]. The spectrum covers a range which starts at a few GeV and extends up ≈ 2 TeV.

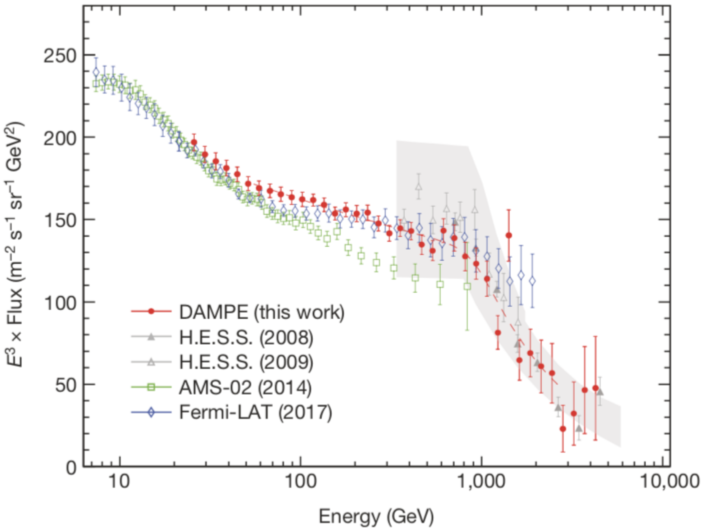

Figure 3.3: The cosmic ray electron spectrum (multiplied by E^3) measured by DAMPE. The red dashed line represents a smoothly broken power-law model that best fits the DAMPE data in the range 55 GeV to 2.63 TeV. Also shown are the direct measurements from the space-borne experiments AMS and Fermi-LAT, and the indirect measurement by the H.E.S.S. [133]

In order to explain the observations shown by data collected from the different experiments, it is necessary to find the probable sources which could accelerate the particles until that energy. In this first range, the **supernova remnant** (SNR) is one of the best candidates. Fermi's mechanism of the first order requires shock waves and a magnetic field. In this environment, the particles crossing various wave fronts are accelerated until they reach the energies detected in cosmic rays. Furthermore, the spectrum of the emitted particles would follow a power spectrum with a spectral index similar to that of cosmic rays.

It is not yet sure why the change in the value of the spectral index occurs. A part of the cosmic rays produced in the Galaxy has sufficient energy to be able to escape from its magnetic confinement. Furthermore, simulations of spherical shocks have shown a variation in the spectrum of the emitted particles similar to that detected in cosmic rays [134]

At the PeV energy, the CR energy spectrum changes the spectral index from $\propto E^{-2.7}$ to $\propto E^{-3.1}$, and this steepening seems to be accompanied by a change in chemical composition, with the latter becoming heavier. So the *knee* is explained with the different "rigidity" for each element; the nuclei, which are heavier than the protons, show the knee in different position. The SNR can explain the spectrum over the knee [135].

The sources which are able to produce cosmic rays with energy $\geq 10^{18}$ eV, instead, are not known. At this energy the cosmic rays are called *Ultra-High-Energy-Cosmic-Rays* (UHECRs) and the flux is very low (1 particles at km^2 every 100 year), but their directions are not significantly affected by galactic magnetic field. The energy possessed by the UHECR corresponds to about 20 J concentrated in a single particle. The problem is which astrophysical sources and how can efficiently transfer this enormous quantity of energy to a single particle. The maximum energy available in a source is described by the Hillas law:

$$E^{max} \simeq Z\beta c \cdot (\frac{B}{\mu G}) \cdot (\frac{L}{kpc}) \tag{3.5}$$

so the maximum energy depends from atomic number of the particle (Z), the characteristic velocity of scattering center (βc), the magnetic field (B) and the characteristic dimension of the region of acceleration (L). The two last terms depend on morphology of the source so in figure 3.4 is reported which sources are able to accelerate the particles until 10^{20} GeV[136].

This scenario predicting the increase of particles energy inside a magnetic field is called **Bottom-Up** scenario. In opposite of this there is another scenario called the **Top-Down** model. This last scenario predicts the existence of super massive particles in the Universe not included in the standard model: their annihilation or decay could produce the standard model particles with energies up 10^{20} eV [137]. These particles behave like cold dark matter and could constitute a fair fraction of the halo of our Galaxy and their arrival directions should correlate with the dark matter distribution.

3.0.2 Production mechanism of $\gamma-$rays

The most violent not thermal processes in the Universe can produce photons at very high energy. Photons with energies in the range from some tens of MeV up are called *gamma rays* and they are the most energetic photons in the Universe. They can be called in different ways based on the energy they

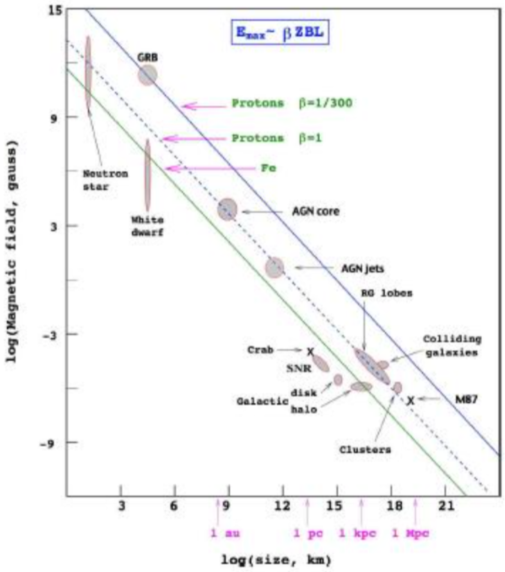

Figure 3.4: The Hillas diagram. Magnetic field strength sand size of possible sites of particles acceleration. The dashed line corresponds to the condition for the magnetic field and source dimension, to accelerate protons at 10^{20} eV. The object below the diagonal line cannot accelerate protons at that energy [130].

possess as shown in the table 3.1.

The most important physical processes to produce γ-rays are four and each one covers a particular range in energy: at low energy Bremssrahlung, when the CR travels inside a magnetic field via synchrotron, via collisions between cosmic rays with production and subsequent decay of mesons π^0, via Compton and inverse Compton.

Space experiments cover a very broad γ-ray energy passband, extending from few MeV to tens of GeV. Like for cosmic rays, the more the flux increases, the more the flux of photons decreases. So, for to study the γ-rays with energy from VHE it is necessary to use Cherenkov telescopes and ground-based experiments.

The spectrum of the photons is shown in figure 3.5. The specific name of this plot is *Spectral Energy Distribution (SED)* and on the abscissa axis is reported the energy of the photons from radio frequency to TeV $\gamma-$rays, while on the *y-axis* is reported the flux density.

Bremsstrahlung

High energy electrons are produced in the sources and travel inside the interstellar gas. They can lose energy through ionization or Bremsstrahlung pro-

Name (Abbreviation)	Energy	Traditional detection tecnique
Low Energy (LE)	1-30 MeV	Satellite based Compton telescope
High Energy (HE)	30 MeV to 50 GeV	Satellite-based tracking detector
Very-High Energy (VHE)	50 GeV to 100 TeV	ground-based atmospheric Cerenkov
Ultra-High Energy (UHE)	100 TeV to 100 PeV	ground-based air-shower particle detector
Extremly-High Energy (EHE)	> 100 PeV	ground-based air fluorescence detector

Table 3.1: Energy intervals of the $\gamma-$ray range is divided.

cesses with the interstellar gas. Moreover the Bremsstrahlung is main mechanism to produce photons in atmospheric when the electrons and positrons have energy over the *critical energy* ξ_{crit}. Below ξ_{crit} radiative energy loss becomes less than collisional energy loss and $e^{\pm}$ do not produce photons via Bremsstrahlung [138].

The characteristic spectrum of Bremsstrahlung is proportional to $1/E$, where E is the energy of the emitted photon and in average the γ-rays produced in this way have the energy from few Mev to around 100 GeV [139].

Synchrotron radiation

When an ultra-relativistic charged particle is moving in a magnetic field, it undergoes an acceleration along the curved path or orbits and emits electromagnetic radiation, as seen in figure 3.6 [140]. The power loss for a particle with mass M and charge Ze, which moves in the magnetic field of intensity B can expressed as:

$$P = \frac{4}{3}\sigma_T c\beta^2\gamma^2 U_B \tag{3.6}$$

where $\sigma_T = 8\pi r_0^2/3$ is the Thompson cross section and U_B is the magnetic energy density, $U_B = B^2/8\pi$.

The equation 3.6 can be applied to every electric particle but, because of the power it is inversely proportional to the mass of the particle (which is

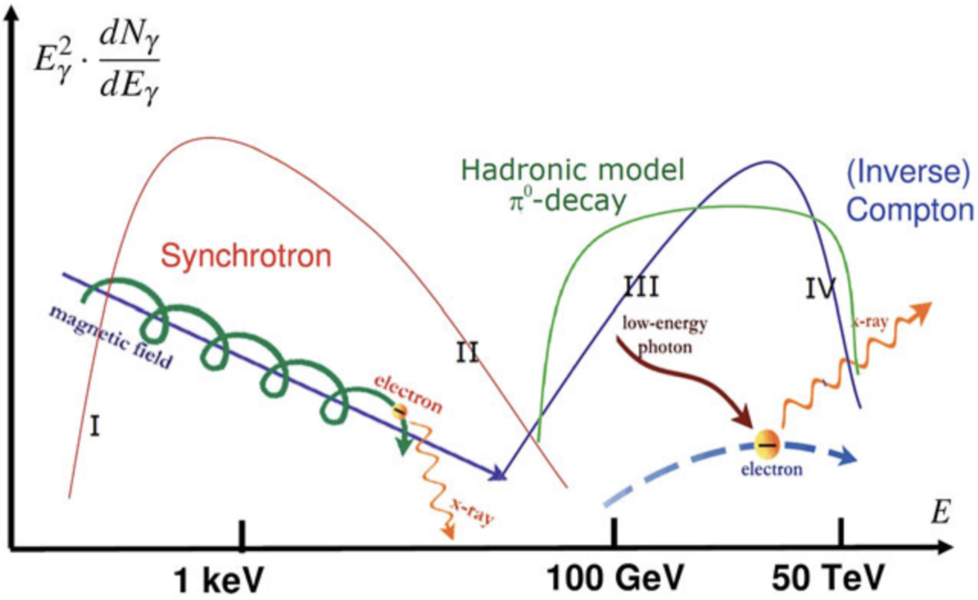

Figure 3.5: Spectral energy distribution of photons where are reported the different contributes from different physics process in leptonic/hadronic models [130].

included inside the definition of $r_0 \equiv e^2/mc^2$), it is not hard to understand that this mechanism is more efficient with a population of electrons which have a mass lower than the other particles.

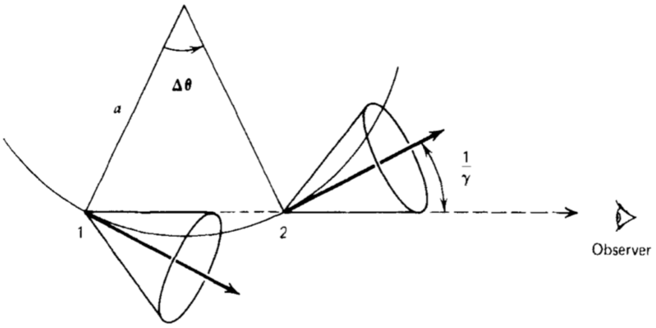

Figure 3.6: Emission cones at various points of an accelerated particle's trajectory [140].

π^0 decay

This process is the main mechanism of $\gamma-$ray production in *hadronic models* of sources. The beam of cosmic rays originated from a source travel in the

Universe and can collide with target nucleons, for example molecular clouds or the Interstellar Medium (ISM), or with photons. From this collision is created an hadronic shower.

$$p + p \to \pi^{\pm}, \pi^{0}, K^{\pm}, K^{0}, p, n, ... \tag{3.7}$$

and a lot of mesons and baryons. For computing the flux of γ-rays it is necessary to include the contribution of every mesons [141].

The $\pi^{\pm}$ mesons are unstable and decay in $l^{\pm}\nu$ where the l is a generic lepton and ν is a neutrino. Instead the π^{0} mesons decay in a pair of $\gamma\gamma$ with electromagnetic decay. In the frame the π^{0} the photons have the energy $E_{\gamma} = m_{\pi}c^{2}/2 = 67.5$ MeV and momentum one opposite to each other. In the frame of the laboratory it is possible to see a spectrum of the π^{0}-decay which rises steeply below ~ 200 MeV and it is called *pion-decay bump*.

Inverse Compton scattering

In the *Inverse Compton* (IC) scattering the ultra-relativistic electrons gives the energy photons so that the photons gain energy at the expense of the kinetic energy of the electron. In the frame of the laboratory the maximum energy that a photon can gain is on the head to head-on collision and can be determined using the kinematics of the Compton effect [140]. If the photon has energy ε and the electron is relativistic with $\beta \approx v/c$ and relativistic Lorentz factor γ, after the collision the maximum energy available for the photon is:

$$E_{\gamma}^{max} = \varepsilon\gamma^{2}(1 + v/c)^{2} \simeq 4\varepsilon\gamma^{2} \tag{3.8}$$

This process can happen in two different regimes. If we denote E_{γ} the energy of the photon the regimes are [142]:

- **Thomson regime**: when the $E_{\gamma} \ll m_{e}c^{2}$ and the recoil of the electron is small, and can be neglected.
- **Klein-Nishina regime**: the $E_{\gamma} \gg m_{e}c^{2}$ and it is not possible to reject the electron recoil.

If we are in a magnetic field region with a population of electrons whose have a Lorentz factor like $\gamma \sim 10^{4-5}$, they will produce photons through synchroton process like we saw in the last section. So, in the same region there will be electrons, that have a differential spectral index q it is possible that such photons can interact with the same parent electrons which generated. Then this pure leptonic mechanism is called *Self-Synchrotron Compton (SSC)* and it is shown in 3.7.

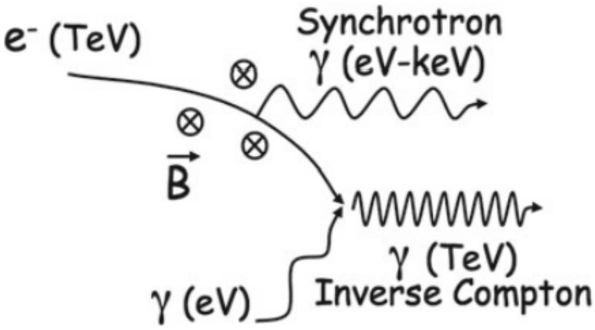

Figure 3.7: Scheme of the synchrotron self Compton mechanism: an ultra-relativistic electron produces photons through the synchrotron mechanism. The same photons scatter with the ultra-relativistic electrons and through the inverse Compton they gain energy up the TeV range [143].

The mean energy in both regimes is:

$$\langle E_\gamma \rangle \simeq \begin{cases} \frac{4}{3}\gamma^2 \langle \varepsilon \rangle & \text{in Thomson limit} \\ \frac{4}{3}\langle E_e \rangle & \text{in Klein-Nishina limit} \end{cases}$$

and the energy distributions is:

$$\frac{dN_\gamma}{dE_\gamma} \propto \begin{cases} E_\gamma^{-\frac{q+1}{2}} & \text{in Thomson limit} \\ E_\gamma^{-q+1} ln(E_\gamma) & \text{in Klein-Nishina limit} \end{cases}$$

where E_γ is the energy of the photons after the scattering, E_e denotes the energy of the electrons, and ε denotes the energy of the photon before the scattering. The Compton component can peak at GeV–TeV energies [143].

3.1 $\gamma-$rays from Dark Matter

The models just mentioned are classified under the *Bottom-Up* model where the particles are accelerated and from the energy they produce gamma rays through different physical phenomena. A different approach, however, is provided by *Top-Down* models in which the decays or annihilations or supermassive particles or topological defects [144]. In this case the particles produced are injected with very high energy. In the VHE region, photons might come from the decay of heavier particles (dark matter particles for example), or from the annihilation of pairs of such particles.

The annihilation of WIMPs can produce SM particles which may have very high energy and we can detect. All final states, except neutrinos, produce gamma rays either directly or as secondary particles. Quarks and gluons hadronize, producing pions and thus photons via $\pi^0 \rightarrow \gamma\gamma$, while $W^\pm$, and Z^0 also produce π^0 via their decays. The emission from these particles is called *soft* channel while $e^\pm$, $\mu^\pm$ and $\tau^\pm$ represents the *hard* channel of production photons [9]. These photons show an energy spectrum which cuts off at the mass of the WIMP, but not knowing where the cut off is, it is not easy to identify the range of the spectrum.

$$\chi\chi \rightarrow b\bar{b}, \quad c\bar{c}, \quad t\bar{t}, \quad \tau^+\tau^-, \quad W^+W^-, \quad ZZ, \quad hh, ... \tag{3.9}$$

It is possible that the self-annihilation of WIMPs could produce γ and other neutral particles like *Z-boson* or *Higgs-boson*. When the WIMPs annihilate producing directly two photons $\gamma\gamma$ the expected signal is a monochromatic line where the energy of the $\gamma-$ray photons is equal to the mass of the WIMP

$$\chi\chi \rightarrow \gamma\gamma \tag{3.10}$$

or into

$$\chi\chi \rightarrow \gamma Z \tag{3.11}$$

where Z is the boson and the energy of the photon is given by $E_\gamma = (m_\chi - m_Z)^2/4m_\chi$ [145]. The ratio of the two process is a function of the mixing angle of CP-violation.

The third way to product γ-rays is called *internal Bremsstrahlung* [146] and some possible processes are shown in figure 3.8. This process involves the annihilation of two dark matter particles with generation of two fermions and a photon:

$$\chi\chi \rightarrow \bar{f}f\gamma \tag{3.12}$$

Also in this case the γ-rays have low energy and the signal is just over the background.

Figure 3.9 shows how the signal should be in self-annihilation of WIMPs particles.

3.2 Flux of signal towards Earth

In the previous section 3.1 I described the different way in which dark matter particles can produce γ-rays. Indirect dark matter searches scan the sky for any excess SM particles or antiparticles produced from annihilation or decay

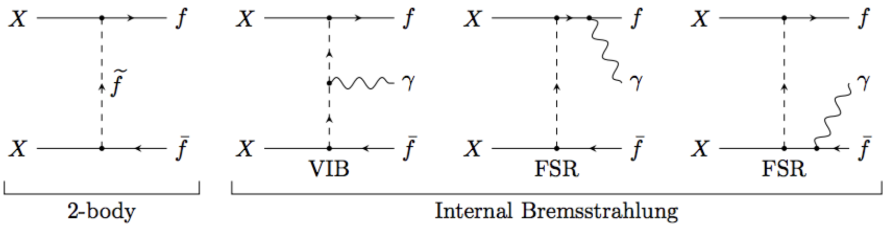

Figure 3.8: The Feymann diagrams for the annihilation of two dark matter particles through Internal Bremsstrahlung [146].

dark matter particles.

The expected flux is given by the combination both process of annihilation or decay DM particles and the amount of *J-factor* [9, 147]. The number of particles per time per energy per solid angle and per area observed in the direction ϕ is:

$$\frac{dN_{ann}}{dEdAdtd\Omega} = \frac{\langle\sigma v\rangle}{2m_\chi^2}\frac{dN_x}{dE}\frac{1}{4\pi} \times J_{ann} \tag{3.13}$$

where $\langle\sigma v\rangle$ is the velocity-averaged cross section. The number of particles from decay is:

$$\frac{dN_{dec}}{dEdAdtd\Omega} = \frac{1}{m_\chi \tau}\frac{dN_x}{dE}\frac{1}{4\pi} \times J_{dec} \tag{3.14}$$

where τ is the lifetime of the dark matter particle. The ratio dN_x/dE is the differential spectrum of x particles emitted per annihilation or decay and can be written like the sum of every spectrum produced for all the possible states f:

$$\frac{dN_x}{dE} = \sum_f B_f \frac{dN_{x,f}}{dE} \tag{3.15}$$

B_f is the branching ratio to final state f and $\frac{dN_{x,f}}{dE}$ is the spectrum of x particles produced for final state f.

The *J-factor*, the second terms of the equation 3.13, is determined by the dark matter distribution and for the annihilation of particles is given by:

$$J_{ann} = \int_{los} \rho^2(\phi, l)dl \tag{3.16}$$

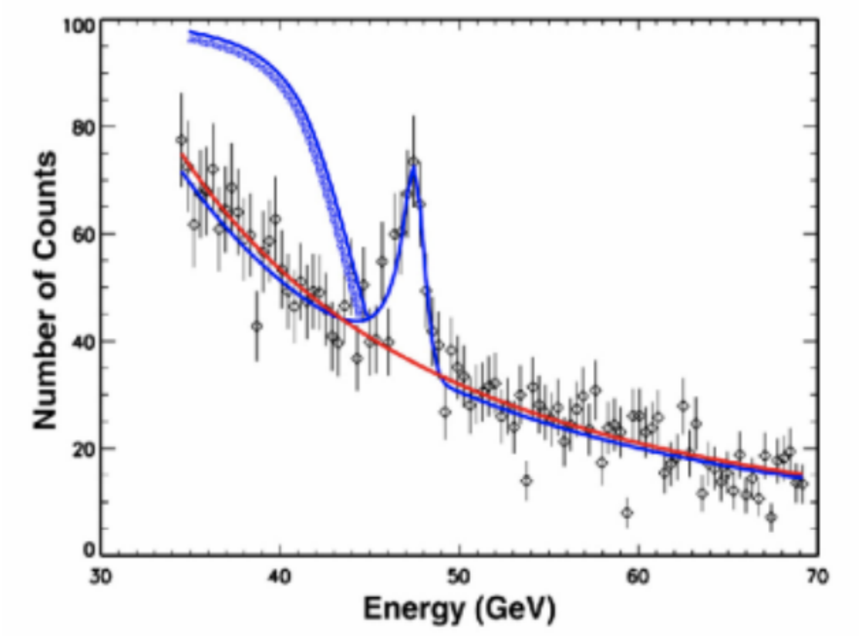

Figure 3.9: Simulated signal from self-annihilation of WIMPs: the signal can show like a peak or a continuum below the mass of the WIMP [143].

while for particle decay the J-factor is given by:

$$J_{ann} = \int_{los} \rho(\phi, l) dl \tag{3.17}$$

In both the equation ϕ is a sky direction, l is a distance along the line-of-sight (los), and ρ is the dark matter density.

3.3 Astrophysical Sources of VHE $\gamma-$ rays

High energy photons are classified in different ranges which have rather arbitrary borders. It is quite common indicate the class of photons with energy from $\sim$ 50 GeV to $\sim$ 100 TeV as Very-High Energy γ-rays.

3.3.1 Galactic Sources

Some sources are located inside our galaxy and for this reason they are referred to as *Galactic sources*. The objects belong to different classes:

Supernova Remnants

Previously it was said that the SNRs are really good sources where the cosmic rays with energy up 10^{15} eV are produced. The last stage of stars with a great mass is an explosion called "Supernova" and it is one of the most energetic events in the Universe. The shocks and magnetic field allow the acceleration of the protons and particles to a very high energy. The collisions of the protons with other particles in the environment can produce hadronic shower π^0 and successively TeV γ-rays from π^0 decay [148].

Pulsar and Pulsar Wind Nebulae

The name *pulsar* is derived from *PULSAting Radio-source* and it means a highly magnetized rotating compact object, usually found in a neutron star (NSs). The first pulsar was discovered in 1967 by their radio waves pulsating and nowadays Fermi-LAT has discovered more than 200 pulsars so far [149]. However only two of them, the **Crab Pulsar** and **Vela Pulsar**, are the only pulsars detected so far by ground via Cherenkov telescopes. The spectrum of pulsars normally show a cut-off at a few GeV, as seen with Fermi-LAT. Two main radiation processes are considered to be responsible for the gamma-ray emission detected in pulsars: synchro-curvature radiation or Inverse Compton Scattering (ICS), or a combination of both [150].

Pulsar Wind Nebulae (PWNe) are pulsars located inside the SNR in which wind, composed of energetic particles which are ejected from the pulsar, interacts with the ISM and the SNR where it is contained. This phenomen originates non thermal radiation; the mean mechanism is synchrotron nebula in the range from radio to X-ray. The relativistic particles can interact with the ambient low energy photons (from the cosmic microwave background, the stellar radiation field, and emission from ambient dust) producing inverse-Compton (IC) emission in γ-ray band [151, 152].

Gamma-ray binaries

The new detectors discovered γ-rays from binary systems which emit both high energy (HE, $0.1 - 100$ GeV) and very high energy (VHE, 100 GeV) gamma rays. This class is composed of one compact object in orbit around a massive star and the peak of the non thermal emission is around 1 MeV. There is also a contribution from the luminous massive star but in this case the emission is thermal and follows the black body law.

The γ-ray binary comes from another class called *high-mass X-ray binaries.* In most of the cases the compact object is a neutron star but in few of them is a black hole. The companion star loses plasma from stellar wind or from a circunmstellar disc. The plasma follows the magnetic field lines close to the neutron star, accreting onto the magnetic poles, producing X-ray pulses as the poles cross the line-of-sight. There are several explanations for the observed VHE γ-ray emission. In the microquasar scenario, accretion into the compact object produces a jet where particles get accelerated (in the right position in figure 3.10). In the pulsar wind scenario, a pulsar orbits around the massive star, the pulsar wind interacts with the companion wind developing shocks where particles get accelerated (in left picture in figure 3.10) [153].

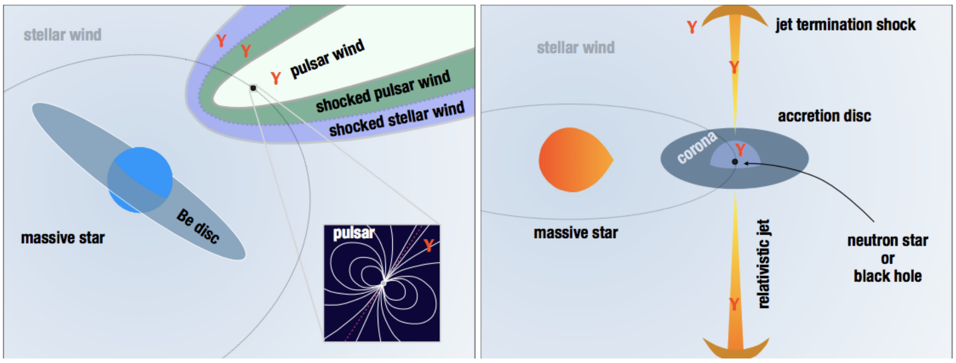

Figure 3.10: Different scenario where the γ-rays could generate. *Left*: the relativistic wind from a rotation-powered pulsar interacts with the stellar wind of its massive companion star. In the right it is shown the other mechanism: the compact object accretes matter from the stellar wind forming an accretion disk and jet. $\gamma-$ray emission can arise from the corona of the accretion disc, within the jet, or at the termination shock of the jet with the ISM [153].

3.3.2 Extra Galactic Sources

This term refers to all γ-ray sources located outside our Galaxy. The photons and neutrinos travel in the space on a straight line so they carry information from sources located very far from the Earth.

The sources are divided in different classes:

Active Galactic Nuclei

Every galaxy has a supermassive black hole located in their center. Those BHs have a mass in the range from $M \sim 3 \times 10^6 M_\odot$ to $M \sim 3 \times 10^9 M_\odot$. Around the 99% the BH are not shown the activity and the $\sim$ 1% of galaxies show activity from their center. Those galaxies take the name *Active Galactic Nuclei (AGN).*

Some of the AGNs have associated the presence of the *jets* which propagate for kpc to even Mpc: for the presence of an intense magnetic field, charged particles can be accelerated and expelled through these jets. Based on certain parameters, AGN are classified into different categories. The AGN that show jets aiming to our direction are called **blazars**.

The models for the production of high energy radiation in blazars can be divided in *hadronic* and *leptonic* models.

The leptonic model takes in consideration the IC scattering between soft photons and the same electrons responsible for the synchrotron emission. This mechanism can take place or inside the jets or outside:

- Synchrotron-self Compton (SSC) model;
- External Compton (EC) model.

It is possible that the soft photons generated with synchrotron emission could be reflected by the Broad Line region (BLR) and come back inside the jet. This model is called *mirror model*.

The hadronic models assume that there is a population of high energy protons which are accelerated in the jet and interacting with ambient soft photons initiating a cascade (Proton Initiated Cascade).

Gamma Ray Burst

The Gamma Ray Bursts (GRBs) are the most powerful energetic events in the Universe and fast flashes of the γ-rays. The energy output is average $\sim 10^{54}$ erg and they are divides in two categories based on the duration of the events. The time is measured with the parameter T_{90}, it is the time that 90% of the photons are detected. So, the categories are:

- **short GRB** if the $T_{90} < 0.3$ seconds and they are very difficult to associate a known sources;
- **long GRB** if the $T_{90} > 3$ seconds and probably they are associated with a formation of the Supernova.

Starburst galaxies

Starburst galaxies are characterized by a boosted formation rate of massive stars and an increased rate of supernovae in localized regions, which also exhibit very high densities of gas and of radiation fields. In this environment the SNRs are the engine to create cosmic rays with energy up $\sim 10^{15}$ eV. Cosmic-ray protons can produce gamma radiation by inelastic collisions with ambient gas particles and subsequent π^0-decay. Primary and secondary cosmic-ray electrons can also produce gamma radiation by Bremsstrahlung and up-scattering of low-energy photons from massive stars or from ambient radiation fields. Fermi-LAT detected γ-rays from M82 and NGC253 [154] while in the VHE range the telescopes H.E.S.S. and VERITAS discovered respectively NGC253 [155] and M82 [156].

3.4 IACT Tecnique

The IACT is an acronym of ***Imaging Atmospheric Cherenkov Telescope*** and, how says in the name, it uses the Cherenkov [1] light generated by charged particles in a transparent dieletric medium that move faster than light in the dieletric medium itself. The light moves in the direction with angle θ in relation of the direction of the particles, like in figure 3.11.

3.4.1 Air Showers and Atmospheric Cherenkov emission

The design of atmospheric Cherenkov γ-ray telescopes is driven by the characteristics of Cherenkov emission from air showers. Ultra-relativistic particles in the shower travel faster than the speed of light in the air. Coherent depolarization of the dielectric medium (of refractive index n) results in a forward-beamed emission called *Cherenkov Radiation*.

The light is emitted around the trajectory and forms a cone where the particle is at the top of the cone. The relations of the angle is:

$$\cos\theta = \frac{1}{n\beta} \quad \text{where } n \text{ is the } \textit{reflective index} \text{ and } \beta = v/c \tag{3.18}$$

and the number of the particles, the intensity, is given by the Frank-Tamm formula:

$$\frac{dN_\gamma}{dx} = 2\pi\alpha\left(1 - \frac{1}{\beta^2 n^2}\right) \cdot \left(\frac{1}{\lambda_{min}} - \frac{1}{\lambda_{max}}\right) \tag{3.19}$$

for $\lambda_{min} = 300$ nm $\leq \lambda \leq \lambda_{max} = 600$ nm [158].

The primary cosmic ray hit the atoms of the atmosphere and produce other particles meanly $\pi^\pm$, π^0, $K^\pm$, K^0, and other barions. These particles

---

[1] In 1958 P.A. Cherenkov won award the nobel prize for the discovery and the interpretation of the effect that carries his name.

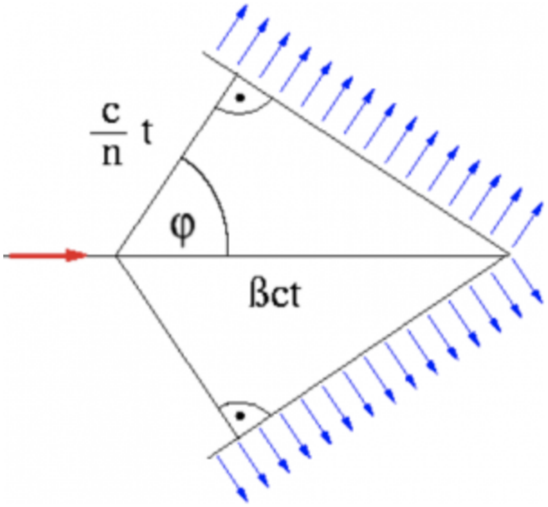

Figure 3.11: Geometry of Cherenkov radiation in ideal case. The particle travel on the straight line with velocity βct and polarize the material around it. The left corner of the triangle represents the location of the superluminal particle at some initial moment ($t = 0$). The right corner of the triangle is the location of the particle at some later time t. At time t it was emitted electromagnetic waves with wave vector represent with blue arrows [157].

decay in a small fraction of time into $\mu^{\pm}$, $e^{\pm}$, ν and γ. This kind of shower is called *hadronic shower* because the primary ray is composed by a proton or a nucleus of some elements and will produce a lot amount of mesons and hadrons. The component of the shower composed of electrons, positrons and photons is called *electromagnetic component*. When the primary cosmic ray is a photon or an electron the shower is called *electromagnetic shower* because is composed by only the electromagnetic component and the model that describes it is called *Heitler's model*. Heitler presented a very simple model of electromagnetic (EM) cascade development [159]: a single very high energetic photon could split into a pair $e^{-}e^{+}$ and themselves will produce photons through Bremsstrahlung, interacting with the atoms of the atmosphere like in figure 3.12. This process continues making a shower: after n interactions the number of the particles is 2^{n}. The model was very simply and could not replace fully detailed simulations but predicted accurately the most important features of electromagnetic showers.

Nowadays it is possible to make numerical simulations of air showers to infer the properties of the primary cosmic rays but it is not easy to describe the dynamics of the shower at high energy because of the large number of

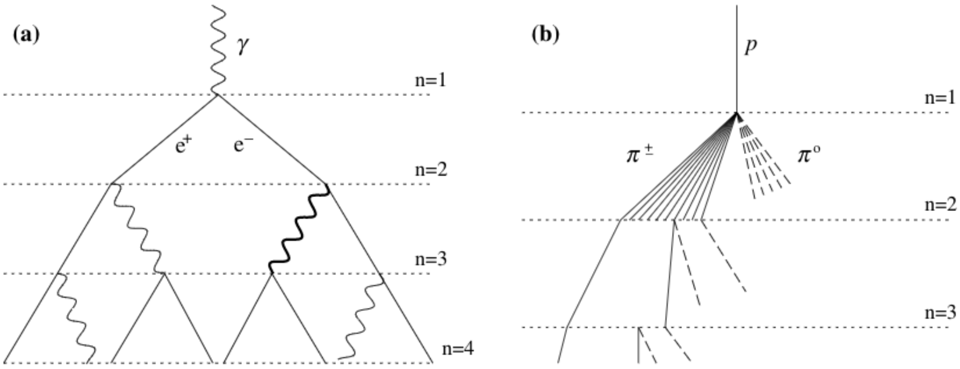

Figure 3.12: Schematic view of showers produced by an incident photon **(a)** and an incident hadron **(b)** following the Heitler's model [138].

particles created (around 10^{10}) [138].

The energy that each particle possesses decreases at each interaction and the density of the atmosphere grows with decreasing altitude . As a result the Cherenkov angle expands from $\sim 0.2°$ at ~ 30 km to $\sim 1.5°$ at sea level. For vertical incident gamma rays, the Cherenkov photon density is almost constant in a ring with radius ~ 120 m centered in the core of the shower and over the radius the density of particles decrease quickly. The inner region is known as the pool and it is described by the plots on the left and on the top right in the figure 3.13. The number of the density of the particles is proportional with the energy of the γ-ray primary and it is used to reconstruct the primary ray energy.

3.4.2 Ground telescopes

The space telescopes have some limitations in the VHE range, in particular over the 100 GeV. The flux at this energy is very low and it is hard to have a good statistic, and also there are no calorimeters light enough to be sent into orbit capable of containing all the shower inside it. So current satellites are too small to contain all the shower by VHE γ-rays, and, above all, fail to collect enough events. Fortunately, the Earth's atmosphere is thin enough so that the effects of the absorption of a VHE γ-ray in it are detectable from the ground and on a large area.

So when the $\gamma-$rays interact with the atmosphere, e^+ and e^- emit Cherenkov light which is collected by the telescopes: the mirrors reflects the photons on the camera, which is located at the prime focus of the dish, and the photomultipliers convert the light in electric signal [160]. In figure 3.14 is shown an

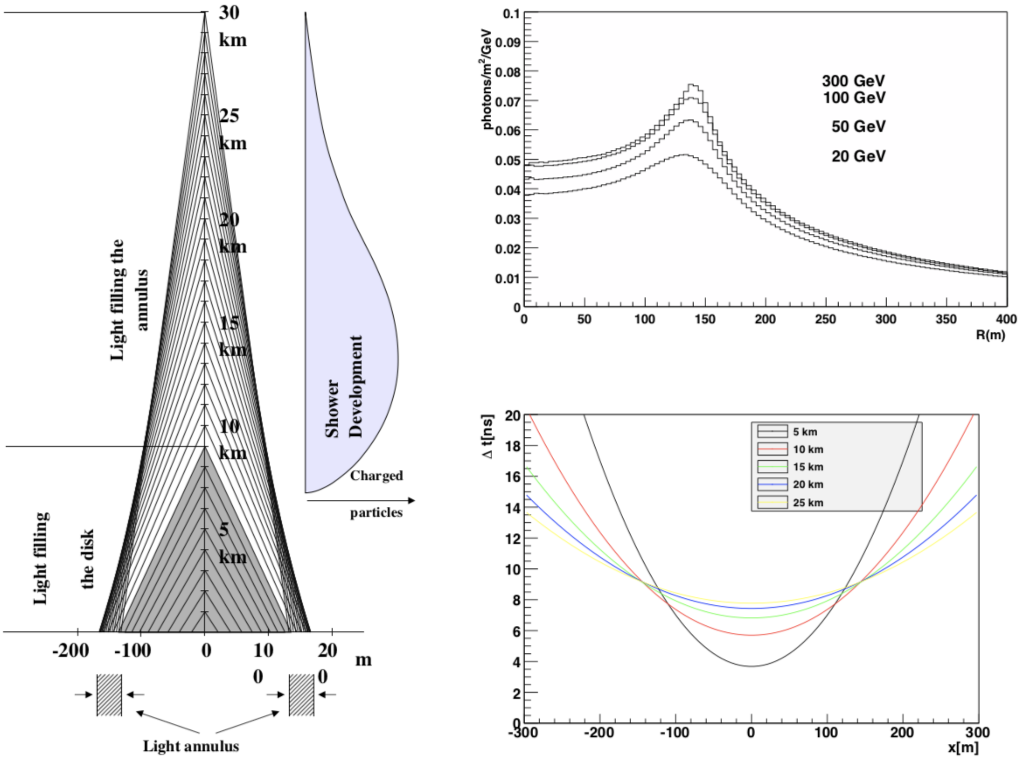

Figure 3.13: **left**: schemes of the shower development and the Cherenkov cone generated; on **top right** is showed the lateral density of intensity profile for different energy; the plot in **bottom right** area shows the time delay for different altitude of emission [160]

example a $\gamma-$ray and the imagine of the shower on the camera.

For the IACT, two basic requirements are required:

a) one or more IACT with sufficient sensitivity to image the Cherenkov light from air showers.

b) an analysis methodology with the power to separate gamma-ray air shower images from background cosmic ray air shower images.

The *imaging technique*, first proposed by A.M. Hillas in 1985 and further developed since then, consisted Cherenkov Light of placing a fast camera composed by 37 PMTs at the focal plane of a telescope in order to record the image of the shower with an angular resolution better than its size [161]. This technique was used in Whipple Observatory 10 m reflector and finally, in 1989, a first γ source was detected: the Crab Nebula [162].

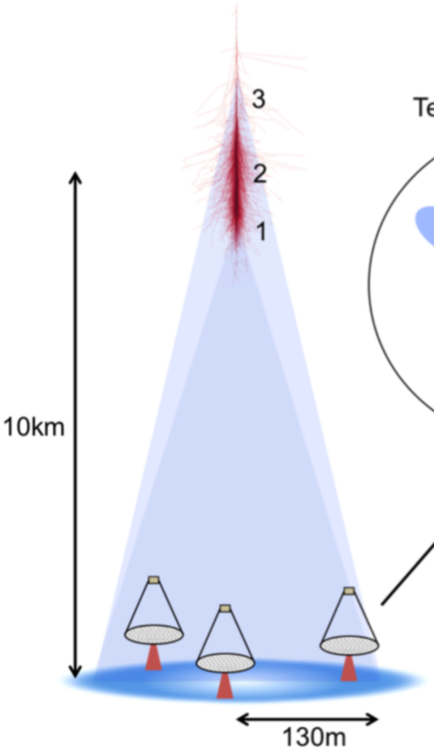

Figure 3.14: Example how the γ-ray produces the shower which produces the Cherenkov light. The telescopes collects the Cherenkov photons and then the primary cosmic ray direction is reconstructed [160].

In 1992 the Whipple collaboration discovered a signal from an active galactic nuclei located at z=0.031: the blazar Markarian 421. The signal was detected at 30% of the signal of the Crab and this fact opened a window on the new field: extragalactic sources [163].

Since then, other telescopes have been built (like CANGAROO or HEGRA), improving their characteristics and the technique of analysis with time. Today, the last ground-based telescopes built are called third-generation telescopes and they were built by two large European collaborations: H.E.S.S. and MAGIC (that will be described in chapter 4).

H.E.S.S

High Energy Stereoscopic System (H.E.S.S.) is an array of five telescopes, four telescopes of Phase I of H.E.S.S. operating from 2002 and one much larger fifth telescope, H.E.S.S. II, which is in operation since July 2012, on a square surface with 120 m side length, in Khomas Highland of Namibia (1800 m a.s.l.). Four telescopes are identical each other and each one has a focal length of 15 m and 13 m diameter. The H.E.S.S. reflector is segmented into 382 round facets with 60 cm of diameter and the total mirror area is 108 m^2 per telescope, while the cameras consist of 960 pixels of 0.16° angular size providing a total field of view of 5°. The drive system combines for each axis and operates on circular rails of about 7 m radius: the positioning speed of the telescopes is 100°/min [164, 165].

In Phase II of the project, a single huge dish with about 600 m^2 mirror area was added at the center of the array for extending the energy coverage towards lower energies and further improving sensitivity. The H.E.S.S. II follows the same guiding principles as for the other smaller telescopes but with different size: the focal length is at 36 m and the total mirror area is 614 m^2. The camera contains 2048 PMTs in 128 drawers and the field of view is equal to 3.2 degrees in the sky [165]. In the figure 3.15 is reported a picture where it is possible to see all the array of the H.E.S.S. observatory: four telescopes of the Phase I and the fifth owner at Phase II.

Figure 3.15: The H.E.S.S. array is located in the Khomas Highland of Namibia. The picture shows the 5 telescopes and the Farm Goellschau place [165].

VERITAS

Very Energetic Radiation Imaging Telescope Array System (VERITAS) is an array of four ground-based gamma-ray telescopes located at the Fred Lawrence Whipple Observatory (FLWO) in southern Arizona, USA. Indeed the telescopes are based on Whipple 10m Telescope. Every telescope has 12 m of diameter and the reflector is composed by 350 identical hexagonal mirrors with an area of 100 m^2.

Each telescope is equipped with 499 pixellated photomultipliers tube (PMT) camera, providing a $\sim 3.5°$ of field of view and the angular resolution is 0.08 deg at 1 TeV and 0.13 deg at 200 GeV (68% containment radius) [166].

MAGIC

MAGIC is the acronym of *Major Air Gamma-ray Imaging Cherenkov* and consist in two parabolic telescopes. Each telescope has 17 m diameter and the focal length of the parabolas is around 17 meter. The MAGIC telescopes are located on Roque de los Muchachos observation site at La Palma, Canarie.

The first telescope, MAGIC I, was installed in 2004 and in 2011 was installed MAGIC II, 80 meter away, like it is possible to see in the Figure 3.16. The next chapter is dedicated to MAGIC where will be describe the features of the telescopes, the subsystems that work together when the data are collected and the software to analyze the data.

Figure 3.16: The MAGIC array in La Palma, on Rocque de los Muchachos. The site was chosen also by other astrophysics collaboration and indeed there are other telescopes. Some of them are present in the picture. Image taken form `https://magic.mpp.mpg.de/`.

CTA

In the same loco the first telescope of the observatory *Cherenkov Telescopes Array* (CTA) was installed near the MAGIC II. The CTA is the new generation of the ground based observatory for $\gamma-$ray astronomy at very-high energies. The project plans to install the telescopes in two sites: one in the northern hemisphere, at Roque de los Muchachos on the island La Palma, and one in southern hemisphere, in the Acatama desert in Chile. In this way it is possible to observe the whole sky.

It is foreseen to install more than 100 Cherenkov telescopes with different size:

- **Large Size Telescope** (LST), with its 23 m of diameter of parabolic reflective surface, to cover the unique low energy sensitivity of CTA between 20 and 150 GeV. This is because γ-rays with low energies produce a small amount of Cherenkov light.
- **Medium Size Telescope** (MST) has a reflector of 12 m of diameter and a focal length of 16 m and observes γ-rays with energy from about 150 GeV to 5 TeV.
- **Smal Size Telescope** (SST) is the smallest telescope of the CTA: has a diameter of only 4.3 m and it is sensitive to the highest energy γ rays between a few TeV and 300 TeV.
- **Schwarzschild-Couder Telescope** (SCT) is an alternative of the MST model and it is a dual-mirrored version: the primary mirror has 9.7 m diameter and 5.4 m is the diameter of the secondary mirrors. The angular resolution is improved as a results of a smaller point spread function (PSF) and the very large number of camera pixels (> 11000), based on silicon photomultipliers (SiPMs), covers approximately 8° field of view.

The number of the telescopes installed in the sites is different. The plan is for the southern site to host a large array of all three classes of CTA telescopes spread over 4 km^2 : four LST, 25 MST and 70 SST so the whole energy range is covered. The northern site will be more limited in size than Chilean site and so it will focus on the low and middle energy ranges, from 20 GeV to 20 TeV. Four LST and 15 MST will be installed [167].

Chapter 4

MAGIC Telescopes

The MAGIC telescopes constitute a stereoscopic system of two 17 m diameter IACTs located in El Roque de los Muchachos in La Palma island in the Canary, Spain. Its coordinates are 28.8 deg N, 17.8 deg W, at 2225 m over the sea level. MAGIC observes the sky at very high energy collecting the γ-rays which are generated from different kind of sources.

This place has been chosen for different reasons: the mains are the low light pollution levels and the peculiarity that the clouds usually stay below the observatory height. Indeed the same area it was chosen by other telescopes for these features and the same site was previously used by *High-Energy-Gamma-Ray Astronomy (HEGRA)* a former IACT array.

The first telescope of MAGIC, called MAGIC I (M1), was inaugurated in 2003 and the science program started in autumn 2004. The collaboration constructed the second telescope of MAGIC, called MAGIC II (MII) in 2008, an evolved twin of M1. Both the telescopes have been operating in stereoscopic mode since 2009 and two years later, 2011-2012 the MAGIC telescopes were further upgraded for improve the field of view, the structure like the mirrors, and the trigger. The main features of the telescopes are summary in the table 4.1.

4.1 Telescope structure

The role of the upgrade which was done during the years 2011-2012 was made to uniform the stereoscopic system hence the older M1 was improved following the design of M2.

The entire structure of one telescope weights ~ 67 tons: two-thirds of the weight is given by the sum of the carriage and the tower next to the reflector

Parameters	M1/M2
Digitizer type	DRS4
ADC res. (bits)	14
Sampling (GS/s)	2.05
Dead time (μs)	27
Camera shape	rounded
Pixel Number	1039
N trigger pixels	547
Trig. area (deg^2)	4.30
Field of View (°)	3.5

Table 4.1: Features of the telescopes MI and MII [168]

while the telescope weights only one third of the total weight: this allows the telescope to move quickly.

The frame of the telescopes is made of a grid of lightweight carbon fiber tubes, connected by aluminium elements in a "net" system composes by tube and knot. This material is able to sustain the weight and the tensions during observation and, at the same time, is light enough to allow MAGIC to be fast at repointing in less than ~ 20 s to any direction in the sky.

The drive system allows to move the telescope in two direction: in Azimuth angle (Az) operates in a range from $-98°$ to $408°$, and in Zenith angle (Zd) operates in a range from $100°$[1] to $-73°$. The telescope can move due to the presence of two azimuth drive units, which can move along on a circle guide rail with 20 m of diameter, and one elevation drive unit placed behind the mirror structure.

A specific software called *COSY* is dedicated to move the telescopes and checks every seconds the correct pointing all along the data acquisition. Angular positions are measured by 14-bit shaft encoders, and cross-checked by a starguider camera mounted in the center of the mirror dish.

The *camera* of the telescope is placed in the focus of the reflector at a distance of 17 meters from the mirror dish and it is held by an aluminum mast secured to the main structure by 20 steel cables.

The camera has a field of view (FoV) of 3.5° diameter and each single pixel has 0.1° diameter, the whole FoV includes 1039 pixels [168]. The photosensors are photomultiplier tubes (PMTs) from Hamamatsu, are grouped in 169 cluster modules and 91 cluster modules are used for the trigger. Every cluster contains seven pixels grouped in a hexagonal configuration, as seen in the figure 4.1.

---

[1] At this zenith angle the telescopes towards the ocean for neutrino searches

The PMTs are 25.4 mm in diameter, with an hemispherical photocathode and 6 dynodes: the cathode and the dynodes are powered with $\sim$ 1250 V. The Cherenkov photons striking the photocathode eject a single electron that is accelerated several times inside the tube, creating a cascade of electrons easily collectable. It is important to collect as many photons as possible from the Cherenkov light so the PMTs have a high quantum efficiency QE $\sim 32\%$ at the peak wavelength and operate at rather low gain of $3 \cdot 10^4$ in order to also allow observations under moderate moonlight without damaging the dynodes [169].

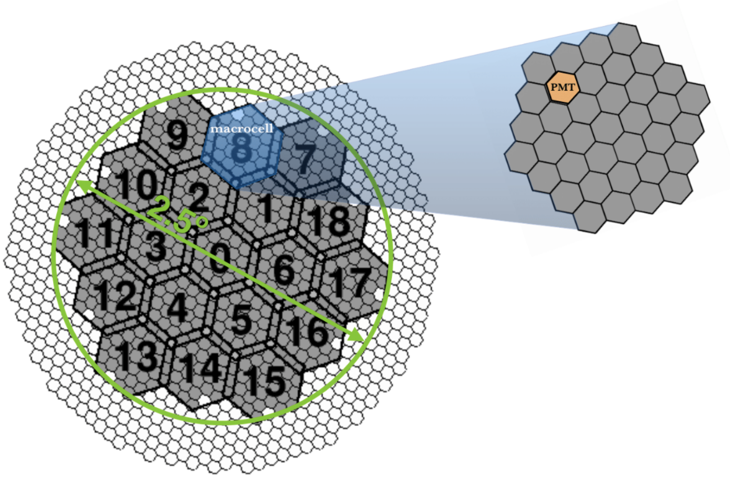

Figure 4.1: The geometry of the camera and all 1039 channels. Camera subdivided in 19 small regions of 37 pixels (macrocells). L1 trigger looks if n neighbors pixel are active inside each macrocells [170]

The reflector of each telescope has an area of 236 m^2 and it was covered by mirrors. Initially the surface of M1 was covered with 956 square shaped mirrors with a size of 49.5×49.5 cm^2 instead the reflector of MII is cover with 247 mirrors with a size of 98.5×98.5 cm^2 [171]. In M1 every four mirrors are mounted on one of the 247 panels, except the panels on the edge which have only three mirrors, while in MII every mirror is mounted on a panel. The panels are fixed at the frame and they are connected to movable actuators which can move the panels with a precision < 20 μm, corresponding to a displacement of the light spot at the camera of less than 1 mm [172].

When pointing the telescope to different zenith angles, the reflector's surface undergoes small deformations under varying gravitation loads. To correct for this effect, the individual mirror-segments must be realigned. For this reason every tile can move alone independently by others tiles. The small bendings are corrected before (and during) the data acquisition through the sub-system called *Active Mirror Control*.

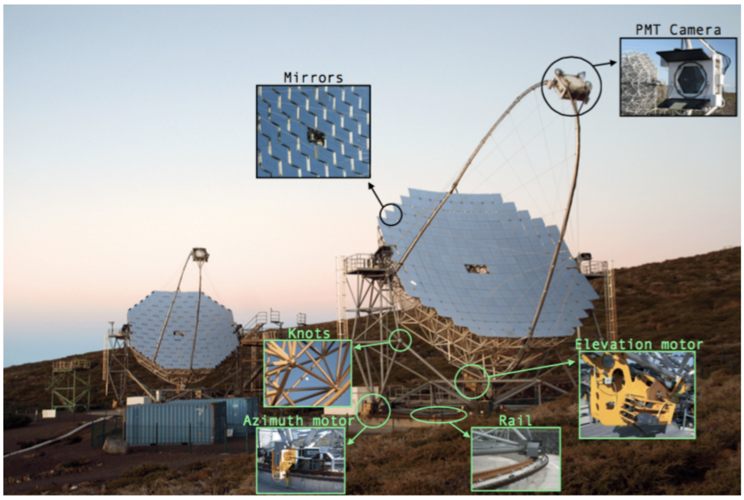

Figure 4.2: The MAGIC telescopes: in background there is M1 and in foreground M2. Some hardware sub-systems are highlighted. Image taken from https://magic.mpp.mpg.de/

4.1.1 Readout and Trigger system

Trigger, readout and Data AcQuisition (DAQ) electronics are placed in a *counting house (CH)*.

The telescopes are connected with the CH through the optical cables which continuously transmit analog signals from the PMTs to the readout and trigger electronics located in the CH. The optical fibers are ∼ 162 m long and are grouped in 19 bundles per telescope. The optical signals from the camera travel through optical fiber and are converted back to electrical signals inside the counting house where are split into two branches: one is needed for trigger and the other for readout.

Only the signals passing the threshold of the **trigger** can be stored and this is necessary to discriminate good signals from the noise. The trigger system is composed of three different levels of trigger called *pixel-wise* (L0), *pixel-group* (L1) [173] and *stereo-telescope* (L3).

- **Level 0 (L0) trigger**: the first check is conducted on individual pixel. For each pixel, a threshold called Discriminator Threshold (DT) is determined, the trigger examines every pixel and only the pixel over the DT threshold are selected. The trigger rate depends on the DTs, the lower the DTs, the higher the trigger rate, hence DTs should therefore be kept as low as possible but this depends by the atmosphere condition or from the presence of stars in the FoV. A dedicate channel rate counter called Individual Pixel Rate Control (IPRC) allows to obtain the individual pixel rate and to adjust dynamically the value of DTs.

- **Level 1 (L1)**: In the second step the camera is split into 19 hexagonal cells, each contains 36 pixels like in figure 4.1. L1 trigger checks all the pixels which survive from the level 0, and sees if there are next-neighbor (NN) pixels over the threshold. If a number n of neighbor pixels in any macrocell are in coincident, the L1 trigger releases a signal. Usually it is used 3 NN for standard stereoscopic observations in MAGIC however n=2, 4 and 5 are also used.
- **Level 3 (L3) trigger**: This trigger operates only in stereoscopic way. L3 receives signal from each telescopes and, if the signal is presented in only one telescope that signal will be rejected, otherwise, the signals are stored if are present on each telescopes. The two signals from L1 show differences in the arrival times of the Cherenkov light from air showers. Because of this the signals are artificially stretched to 100 ns width and delayed according to the zenith and azimuth orientation of the MAGIC [168].

The second signal is directed to the readout system, responsible for the DAQ. This signal is delayed a few ns in order to wait for the trigger system response, which will determine if an event is produced by a $\gamma-$ray and hence, has to be recorded by DAQ. The main component of the current digitization electronics is *Domino Ring Sampler version 4 (DRS4)*. DRS4 is composed by an array of 1024 switching capacitors and its sampling frequency is set on 1.64 Gsamples/s.

The DRS4 works in this way: the analog data are stored in the capacitors with a switching period of 500 ps (512μs in total). Once the cycle is finished, it starts over overwriting the first capacitor and so on. When the trigger occurs the sampling is stopped and the charges of the 60 capacitors are read out by an ADC of 14 bit precision at a speed of 32 MHz [170, 174]. This is called Region of Interest (RoI) and allows to reduce the dead time to 27μs. The data from the RoI of the DRS4 chip are read by the DAQ program.

4.1.2 Auxiliar systems

GRB alert

As described in section §3.3.2 the GRB events are very fast and can take place in every point of the sky. The detection of VHE emission from GRBs is one of the Key Observational Program (KOP) of the MAGIC experiment. It is necessary that the telescopes may observe the first instant of the events, when the photons have the maximum energy.

MAGIC telescopes is connected with space-telescopes (e.g. Swift-XRT or Fermi-LAT) because of their wide FoV. In total GRB satellites that can send GRB triggers are 5 and when one of them observes a GRB sends a message of alert in the system of MAGIC. A software called GSPOT checks the observability criteria: Sun below astronomical horizon, delay to $T_0 < 4$h, position error $< 1.5°$, Zenith $< 60°$, distance to Moon $> 30°$. If all the criteria are satisfied, GSPOT will tell the Central Control to repoint automatically the telescopes to the GRB position and start the follow-up [175].

Weather Monitoring System

The weather station is located on the roof of the counting house and monitors the atmospheric state every 2 s and two software, one per telescopes called respectively CaCo1 and CaCo2, monitoring the values in input. This procedure is necessary for to safety the operation of the telescopes protecting them from damages the subsystems which operate in open air. The weather station includes several instruments to monitor the weather and communicates the value of wind, rain, humidity and the pressure. For each of parameter there is a safety limit and when the limit is exceeded automatic reactions are performed to ensure the safety of the telescopes.

Pyrometer

The pyrometer is installed on the dish of the M1 telescope and points to the same direction of the telescope. It provides the cloudiness parameter with a number in a range from 0, the sky is completely without clouds, to 100, the sky is completely covered by clouds. The pyrometer measures the temperature of the sky fitting the value of IR radiation with blackbody spectrum. The measured temperature increases if the sky is cloudy, because clouds reflect radiation from the ground. Thus, an estimation of the cloudiness (higher cloudiness implies lower transparency) is given by:

$$c = \frac{T_{low} - T_m}{T_{low} - T_{up}} \tag{4.1}$$

where $T_{low} = 250\text{K}$ and $T_{up} = 200\text{K}$ and correspond respectively when the sky is clear and when the sky is cover. T_m is the temperature measured by pyrometer.

LIDAR

One of the most important ancillary system for the analysis, in particular way for DM analysis, is the LIDAR which allows to measure the atmospheric extinction along the line of sight (l.o.s.) of the telescope. The acronym LIDAR derives from *Laser Imaging Detection And Ranging*) and its values is very important because the dust can absorb the Cherenkov light and this affects the reconstruction of the main parameters of a shower, in particular the estimation of the energy of the primary particles: this will lead to a wrong computation of quantities like the effective area and the flux.

The LIDAR is located in a dome on the CH roof and works together with the MAGIC telescopes. It flashes a laser at a position shifted by 3° from the source, taking care not to disturb the measurement of the telescopes. The LIDAR fires 50000 shots at 250 Hz, so one data run takes about 3 min, a new run is performed every 5 min [176]. The laser releases pulses which peak at 532 nm wavelength, not too far from where the Cherenkov spectrum is peaked ($\sim$ 330 nm), and scatter with air molecules clouds (Rayleigh scattering) and particles (Aerosol/Mie scattering) in the sky. A mirror with 60 cm diameter and 150 cm focal length is focused on the detector module. The detector module comprises a 6 mm diameter diaphragm, a pair of lenses with interference filter and a Hybrid Photo Detector (HPD, Hamamatsu R9792U-40) with 55% peak quantum efficiency.

The return signal is processed and will provide a value of the expected transmission t at 3, 6, 9 and 12 km of altitudes. The scale of the values that LIDAR transmission can assume at 9 km is split into different ranges which are reported in table 4.2. The data are affected by the quality of the air. Data collected within an aerosol transmission higher than 85%, are considered to be compatible with published systematic uncertainties, and can be used to do science with no need for a correction. For a transmission between 75% and 85% the correction are suggested while, when the data show an aerosol transmission between 55% and 75%, LIDAR corrections are needed to compute spectrum and flux.

Transmision Range	Data quality
$t > 85\%$	Perfect (no correction)
$75\% < t < 85\%$	Good (correction suggested)
$55\% < t < 75\%$	Bad (correction are needed)

Table 4.2: Based on the transmission range the data are classified with the label *perfect* quality, *good* quality and *bad* quality at which is necessary to apply the LIDAR correction

Figure 4.3: The MAGIC LIDAR system on top of the counting house, with the dome completely open. In the picture there are also the MAGIC II telescope and GRANTECAN in the background [176].

4.2 Standard analysis chain

The standard analysis chain of MAGIC collaboration is separated in several different steps and each step has its dedicated program[177]. All the programs are included inside the package called *MARS*, acronym of *MAGIC Acquisition and Reconstruction Software*. MARS is an object-oriented C++ software based on the ROOT library.

The purpose of the analysis chain is to extract the information from the data collected such we are able to reconstruct the primary particles generating the showers and determine the direction and energy of the γ-ray candidates.

The analysis starts with the RAW data which consist of binary files containing the full information available per pixel and per triggered event, plus reports file which are written in ASCII and containing auxiliary information from the different telescope subsystems. These data are converted into ROOT format and every information is reassembled in ROOT-trees. The first step of the analysis is called *low level processing*. For each pixel in each event two pieces of information are obtained: charge (in photoelectron) and time which the signal arrives. With those information we proceed with the *image cleaning*. This is necessary to calibrate the telescopes and identify and separate the signal from the baseline level.

Subsequently for every event *Hillas parameters* are computed. The basic ones were originally introduced by Hillas in 1985 and their definitions are based on the distribution of the photons in the pixels that constitute the Cherenkov image. Nowadays we use an extended set of parameters and some of them are shown in figure 4.4. This process is performed on each telescope.

Until now we have two independent images of the same event: one from the *Camera 1* (M1) and the other *Camera 2* (M2). Then the two different images are combined in a single stereoscopic event as see in figure 4.5.

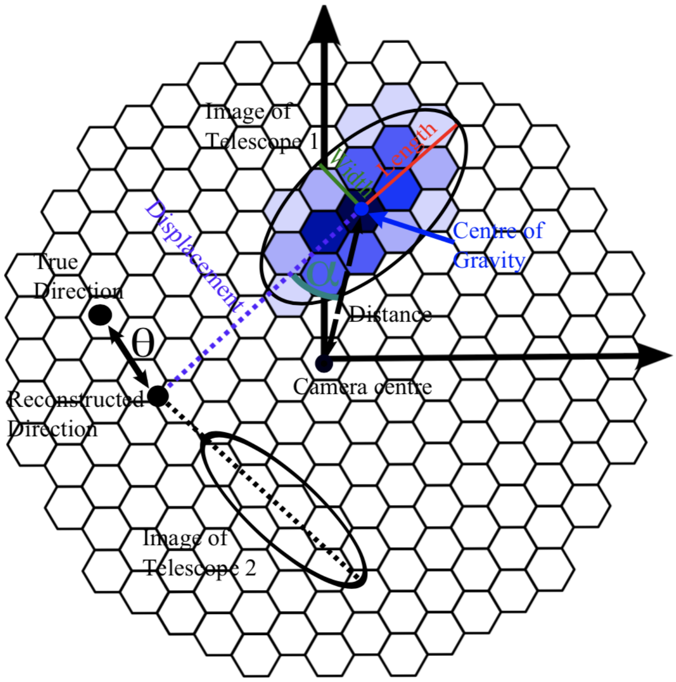

Figure 4.4: The Hillas parameters are associated for each event and each telescope. Some of them are shown in the figure. The γ event produces an ellipsis in a camera. The blue pixels are the PMTs which had collected the light from the events. Also in the other camera an ellipsis is created and from their merger the direction of the shower is found [176].

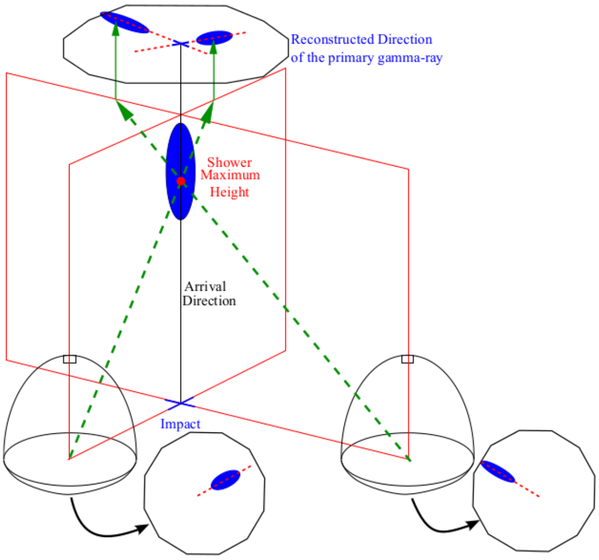

Figure 4.5: A single event is seen from each telescopes. The stereo reconstruction allows to compute the direction and the energy of the primary $\gamma-$ray [176].

It is necessary to apply cuts on the data because they may be affected by technical problems or bad weather conditions. Using different indicators the analyzer can select the data according to his needs. This process could be done both for each single telescope or on the set of stereo data.

The trigger can be activated by three different kind of events: accidental triggers, muons or shower generated by γ and hadronic events. The coincidence trigger excludes most of them and the remaining and most important background contribution is due to the cascades of hadronic origin.

The surviving stereo data are undergone to *random forest* which are necessary to compute the γ/hadron separations, direct and energy reconstruction.

The method use an algorithm called *random forest* (RF) [178]. RF method is based on a collection of decision trees, built up with some elements of random choices. Generally RF are first trained on a set of Monte Carlo which are simulated γ-rays, and OFF events (data set composed mainly by hadronic shower). RF uses a set of N high discriminating parameters to construct a large number (default 100) of decision trees. Each event is characterized by a vector whose components are image parameters obtained by analyzing the camera pixels.

From this sample, a binary decision tree can be constructed, subdividing the parameter space first in two parts depending on one of the parameters, and subsequently repeating the process again and again for each part. RF creates a set of largely uncorrelated trees and combines their results to form a generalized predictor. One example about a decision tree is displayed in figure 4.6(a).

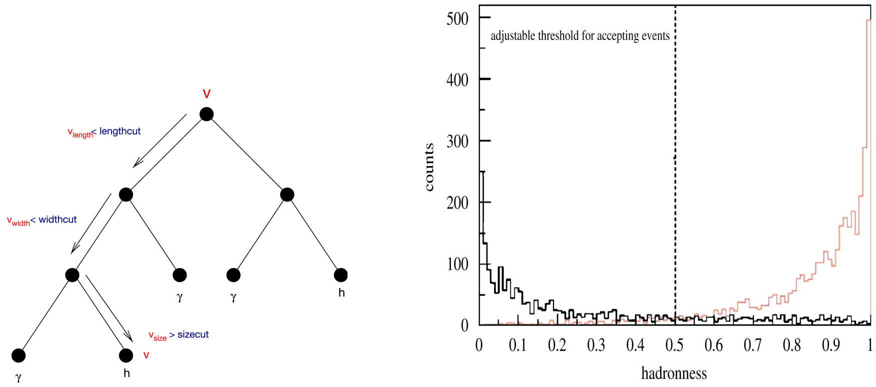

(a) A single tree decision (b) The hadroness distribution

Figure 4.6: Plot (a) shows a scheme of tree structure: each node is a threshold and the event v, which has component v_{lenght}, v_{width} and v_{size} moves on the path and at the end it will be classified like an hadron. In (b) plot is displayed the distribution of the hadroness value: on the x-axis is reported the value of hadroness and on y-axis the number of events with that values [178].

A single event must be classified for every tree. At the end it is computed a mean of the times that the same event is classified like a γ or a hadron. The equation is:

$$h = \frac{\sum_{i=1}^{N_{Tree}} l_i}{N_{Tree}} \tag{4.2}$$

where l_i is the result of the tree of the event with index i and the result h is called *hadroness*. RF assigns at every event a value of h: the more $h \to 0$ the more the event is associated a γ shower; on the other side, the more $h \to 1$ the more the event is associated an hadron shower. So the hadronness, spanning from 0 (ideal γ ray event) to 1 (hadron shower), indicates if the event is a good gamma candidate. Only events with hadronness below a certain cut value will be used for the subsequent steps of the analysis.

The cut values are chosen to minimize the value of Gini index Q_{Gini}[2] (also called Gini coefficient): is a measure of statistical dispersion of a sample and a higher Gini index indicates greater inequality in the population.

---

[2] Gini coefficient was developed by the Italian statistician and economist Corrado Gini in 1912 like a measure of the income inequality in a society.

Given a population N composed by N_γ and N_h, the Q_{Gini} can be expressed in terms of the node class populations:

$$Q_{Gini} = 4\frac{N_\gamma}{N}\frac{N_h}{N} = 4\frac{N_\gamma(1 - N_{\gamma)}}{N^2} \in [0, 1] \tag{4.3}$$

Minimization of the Gini index provides both the choice of the image parameter and the split value to be used.

RF are used also to have a better estimate of the shower direction. We call the parameter *disp* the angular distance between the image center of gravity and the point on the camera which corresponds to the shower direction [179]. It is computed using by RF algorithm which is trained on MC simulated γ-rays events for which the correct source position. Hence the MC the real value of *disp* is known, then it is computed on the data set. For every event in a single camera are given 2 points of disp (because of head-tail ambiguity), they become 4 points when the images are merged and are combining *disp* results from both telescope. The closest pair of *disp* points are chosen if its distance is smaller than a certain value.

The training of RF on MC is necessary also to estimate the *energy recostruction* for the sample of data which we want to analyze. The method used is called look-up table (LUT). The γ MC training sample is divided in bins for every parameters considered for the energy reconstruction. A multi-dimensional table containing the mean energy (and RMS) of MC events belonging to each bin is build. Then the estimated energy of a real event is the value stored in the table for the multi-parameters bin corresponding to this event.

The energy of the incident $\gamma-$ray is proportional of the number of photoelectrons generated from the shower. In first approximation, called *zero order*, the energy is proportional of the *size* of the image. At *first order* the LUT considers also the ratio between the impact and Cherenkov radius. At *second order* consider the small variance due to atmosphere transparency, geomagnetic field and image leakages (when the image is at the edge of the FoV and its energy is underestimated).

Once we have found hadronness, reconstructed energy and direction of the events, we move on to the second part of the analysis, called **standard high-level data analysis**, where we will study the signal from the source. In this step the data are clean from the background and there are all the parameters to compute the *significance*, the *skymap*, the *flux* (or Spectral Energy Distribution, SED), and the *light curve* from the source.

A dedicated software called *Odie* computes the significance using the $Li\&Ma$ method [180]. The significance is computed considered ON and OFF events, which are plotted on the histogram called θ^2-plot like in figure 4.7. θ parameter is the distance between the reconstructed incoming direction of the primary $\gamma-$ray and the nominal source position. The source is located at $\theta = 0$ and every value of θ correspond to a circumference with radius θ^2 and center on where there is the source. The extraction of signal leads to two independent data sets: N_{on} is the number of events when the telescopes aim the source, N_{off} is number of events come from background observation. The significance S is computed through the equation:

$$S = \frac{N_{on} - \alpha N_{off}}{\sqrt{\alpha(N_{on} + N_{off})}} \tag{4.4}$$

where the parameter $\alpha = t_{on}/t_{off}$ is the ratio between the time was observed the source (t_{on})and the time to background observation (t_{off}). The equation 4.4 is applied when the number of photons is very low and follow a Poisson distribution but, in the case that the number of photons is not too low ($N_{on} > 10$ and $N_{off} > 10$), $\alpha \simeq 1$ and are approximately normally distributed [180], the equation of significance becomes:

$$S = \sqrt{2}\Big\{ N_{on}\ln\Big[\frac{1+\alpha}{\alpha}\Big(\frac{N_{on}}{N_{on}+N_{off}}\Big)\Big] + N_{off}\ln\Big[(1+\alpha)\Big(\frac{N_{off}}{N_{on}+N_{off}}\Big)\Big]\Big\}^{1/2} \tag{4.5}$$

The equation 4.5 is the standard way of calculating significance for detected signals for MAGIC.

The image shown in figure 4.7 is taken from my analysis on the Crab. On the *x-axis* are reported the values of the θ^2 in the range from 0 to 0.4, while on the *y-axis* is reported the number of the events. The equation 4.5 is applied on the region inside the vertical dashed line which is placed at $\theta^2 = 0.02$. The software extracts both the value of N_{on} which is the number of events inside the region $\theta^2 = 0.02$, and N_{off} which is the number of background events. Because of the two quantities are almost the same, the value of the significance is around the value 0.

The *sky map* is a two-dimensional histogram containing the arrival direction of all the $\gamma-$ray candidates registered during the measurements. It is possible to choose different coordinate system: generally it is used **equatorial cordinates** to create the images of the astrophysical sources. The incoming direction of each photon is reconstructed with a certain error called **Point Spread Function** (PSF), that describes the distribution of uncertainties in the reconstruction of the incoming direction of photons originated by a point-like source. The software *CASPAR* produces a skyplot in two steps: first a

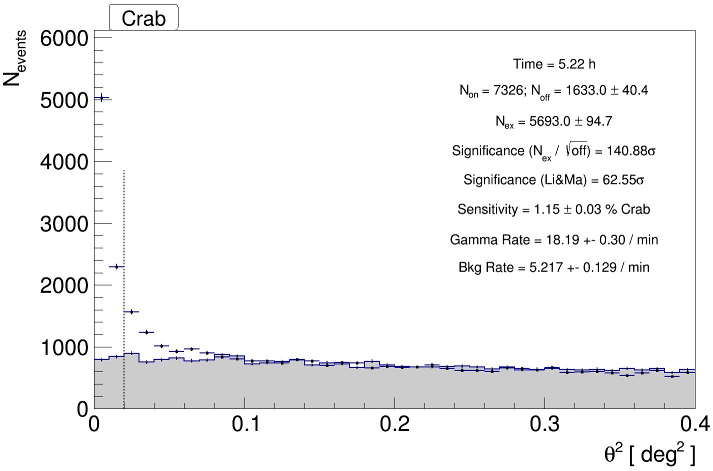

Figure 4.7: The θ^2-plot of the Crab is shown.

camera exposure model is created on-the-fly, using one of the algorithms described below, secondly from that model the background event distribution in sky coordinates is sampled, and compared to the real total event distribution. To obtain the exposure model two algorithms are available: *blind map*, without assumptions on the source position, and *wobble position*, the source is assumed to be where expected. From these models both an OFF background map and an ON map with the events in the data are created. Caspar produces several plots: ON, OFF, ON-menus-OFF map, flux and relative flux plot, and the most important, **Test Statistics (TS)** map and its distribution. TS distribution compares the Null Hypothesis, what you expect without the source in the FoV, with the data.

Another software that I used during the thesis is *Flute*. Flute is a dedicated software to compute the differential spectrum and the integral flux.

The differential spectrum is defined as:

$$\frac{dF(E)}{dE} = \frac{dN_\gamma}{dE dA_{eff} dt_{eff}} \tag{4.6}$$

where dA_{eff} is the effective area given by the product of the ratio between the γ measured and γ simulated (from MC simulation) and the effective area which is computed using MC:

$$A_{eff} = \frac{N_\gamma}{N_{\gamma,simulated}} A_{MC,total} \tag{4.7}$$

and t_{eff} is the effective time of observation and it is computed form the Poisson statistic:

$$t_{eff} = \frac{N_0}{\lambda} \tag{4.8}$$

where λ is the rate of true events. In the figure 4.8 is show the spectral energy distribution which is obtained to times the differential energy spectrum with E^2.

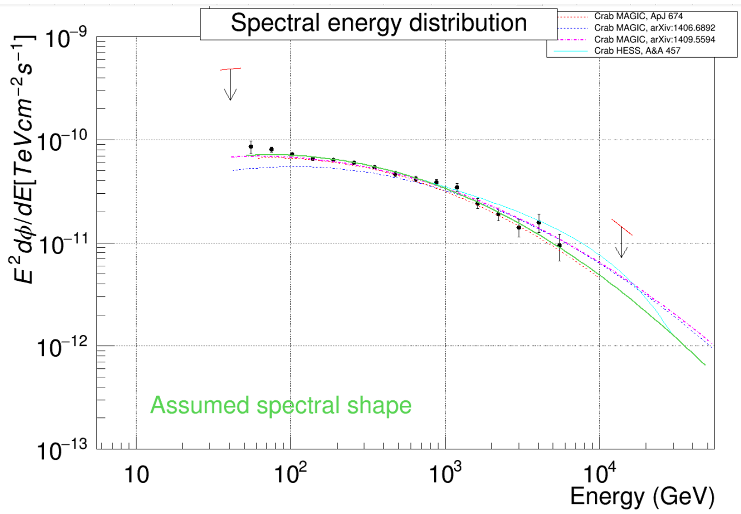

Figure 4.8: The software Flute computes the Spectral Energy Distribution. In this case I used the same data of Crab that I used for the θ^2-plot in figure 4.7

It is possible to compute also the integral flux given by:

$$F_{E>E_0}(t) = \int_{E_0}^{\infty} \frac{dN_\gamma}{dE dA_{eff} dt_{eff}} dE \tag{4.9}$$

where in this case is computed the flux on all the energy band above the threshold E_0 and in function of the time.

Usually dark matter analysis starts from this point. It is necessary to extract every signal from the datasets and check the presence of excess of $\gamma-$rays, and the significance and the flux are computed. If there is not signal it is necessary to compute the upper limits using the specific method called *Full Likelihood*.

4.3 The Full Likelihood method

The Full Likelihood (FL) method is an alternative standard approach based on an empirical assumption on the expected spectral shape and the maximum likelihood analysis [181].

In the standard analysis in MAGIC the probability to see an observe excess can be estimated by maximization of the likelihood function:

$$L(g, b|n, m) = \frac{(g+b)^n}{n!} e^{-(g+b)} \times \frac{(\tau b)^m}{m!} e^{-(\tau b)} \tag{4.10}$$

where n is the number events in ON region while m is the number events in OFF region, τ is the ratio of Off to On exposure time, while g is the number of γ-ray, b is the background events given by Poisson statistic.

FL method integrates the equation 4.10 with the DM models which is denoted with the lecter M with parameters $\boldsymbol{\theta}$. The FL is given by:

$$\mathcal{L}(N_{Est}, \boldsymbol{\theta}|N_{Obs}, E_1, ..., E_{N_{Obs}}) = \frac{N_{Est}^{N_{Obs}}}{N_{Obs}!} e^{-N_{Est}} \times \prod_{i=1}^{N_{Obs}} \mathcal{P}(E_i; M(\boldsymbol{\theta})) \tag{4.11}$$

where N_{Est} denotes the total number of observed and estimated events, $N_{Obs} = n + m$, and $\mathcal{P}(E_i; M(\boldsymbol{\theta})$ is the value of the probability density function (PDF) of the event i with measured energy E_i.

The $\mathcal{L}$ per period is a product of every $\mathcal{L}_\rangle$ find for each telescope pointing direction $i = 1, 2, 3, 4$ and per energy bin E_j. In this analysis we have several nuisance parameters ($\boldsymbol{\nu}$): the *J-factor* and its error γ_J, the parameter τ and its error σ_τ, and the b_{ij} background events in the On region. The parameter g_{ij} depends on the free parameter $\langle\sigma v\rangle$ by:

$$g_{ij}(\langle\sigma v\rangle) = T_{Obs,i} \int_{E'_{min,j}}^{E'_{max,j}} dE' \int_0^\infty \frac{d\Phi(\langle\sigma v\rangle)}{dE} A_{Eff} G(E'|E) dE \tag{4.12}$$

where $T_{Obs,i}$ is the total time of observing per direction, E and E' are the true and estimated γ-ray energy of the j-th energy bin, A_{eff} is the effective collection area and G is the PDF of the energy estimator.

The binned $\mathcal{L}$ for each pointing and each IRFs as:

$$\begin{aligned}\mathcal{L}_i(\langle\sigma v\rangle; \boldsymbol{\nu}_i|\mathcal{D}_i) = \prod_{j=1}^{N_{Obs}} \Big[\frac{(g_{ij}(\langle\sigma v\rangle) + b_{ij})^{N_{ON,i}}}{N_{ON;ij}!} e^{-(g_{ij}+b_{ij})} \frac{(\tau_i b_{ij})^{N_{Off,i}}}{N_{Off}!} e^{-(\tau_i b_{ij})} \Big] \\ \times \mathcal{T}(\tau_i|\tau_{Obs,i}, \sigma_{\tau,i}) \times \mathcal{J}(J|J_{Obs,i}, \sigma_{J_{Obs}}) \end{aligned} \tag{4.13}$$

where the index i represents the set of data for each position of telescope and j

is the estimated energy bin. The $\boldsymbol{\nu_i}$ is nuisance parameters and $\mathcal{D}_\rangle$ is the data set for each position. $\mathcal{J}$ is the likelihood for the J-factor, $\mathcal{T}$ is the likelihood for τ_i (the OFF/ON acceptance ratio), parameterized by a Gaussian function with mean $\tau_{Obs,i}$ and variance $\sigma^2_{\tau,i}$ which include statistical and systematics uncertainties [6, 7]. In this analysis have been chosen a systematic uncertainty $\sigma_\tau = 0.015\tau_{Obs,i}$.

Given two hypothesis we call *null hypothesis*, H_0, the idea that there are not dark matter signal, hence $g_{ij} = 0$, and *test hypothesis*, H_1, the idea that the signal follow the equation in section 3.1 where an a priori we supposed a model of decay.

To maximize the power of a test of H_0 with respect to the alternative H_1, the Neyman–Pearson lemma states that the critical region w should be chosen such that for all data values x inside w, the ratio:

$$\lambda_P(\langle\sigma v\rangle|\mathcal{D}) = \frac{\mathcal{L}(\langle\sigma v\rangle, \hat{\hat{\nu}}|\mathcal{D})}{\mathcal{L}(\widehat{\langle\sigma v\rangle}, \hat{\nu}|\mathcal{D})} \tag{4.14}$$

where $\widehat{\langle\sigma v\rangle}$ and $\hat{\nu}$ are the values of the parameters which maximize $\mathcal{L}$ and and the $\hat{\hat{\nu}}$ maximizes $\mathcal{L}$ for a given $\langle\sigma v\rangle$. Using Wilk's theorem for great set of data we have $-2ln(\lambda_P(\widehat{\langle\sigma v\rangle}|\mathcal{D})) \sim \chi^2(d)$ where d are the degrees of freedom. Using the likelihood ratio test, we would reject the null hypothesis H_0 when:

$$-2ln(\lambda_P) > \alpha \sim \chi^2_\alpha \tag{4.15}$$

Upper limits with α at 95% Confidence Level (CL) are given for:

$$-2ln(\lambda_P(\widehat{\langle\sigma v\rangle}|\mathcal{D})) = 2.71 \tag{4.16}$$

The numbers of the events detected in ON and OFF regions for different bins in function of the IRFs for a specifc observation period, are the input parameters of the likelihood .

The FL method will be used to compute the $\langle\sigma v\rangle$ under the null hypothesis H_0 and test hypothesis H_1, considering the "pure" annihilation of dark matter particles into channels $b\bar{b}$, $\mu^+\mu^-$, $\tau^+\tau^-$, and W^+W^-, and one-sided 95% confidence level (CL) limits are given by the largest of the two $\langle\sigma v\rangle = 2.71$ solution

Chapter 5

MAGIC observation of M15

As seen in section 2.4, M15 is the only globular cluster with those particular features located in the Northern hemisphere that MAGIC can observe.

During 2015 and 2016 MAGIC telescopes observed M15 in search for a VHE $\gamma-$rays excess due to pulsars. The same data collected are used also to find some γ-rays signals from self-annihilation dark matter particles.

5.1 Dark Matter content

The J-factor represents the astronomical factor and depends on the geometry of the Earth-source system and the amout of DM in the source. The γ-ray differential flux from dark matter annihilation measured within a solid angle $\Delta\Omega$ is given by:

$$\frac{dN_\gamma}{dE} = \Phi^{PP}(E) \times J(\Delta\Omega) \tag{5.1}$$

where the left side of the equation depends on the physical model of the annihilation or decay, while the second term depends completely by the source (or better how much DM is present inside it and the distribution) and its position in the sky.

The amount of dark matter inside the core of the globular clusters is a subject of debate. Globular clusters are the oldest structures in the Universe and probably they were located in the center of their sub halos. Unfortunately it is supposed that the tidal effects by the host galaxy have been destroyed the sub halos around the GC while the core-collapse process could compress the DM in the center and dramatically enhance the γ- ray flux.

In the next section I will renew the J-factor extimations used in the previous analyses of M15.

Whipple observations

In the analysis presented in [182], the Whipple collaboration chose several sources: two dwarf galaxies, Ursa Minor and Draco, two galaxies of the Local Group, M32 and M33, and the globular cluster M15. The equation of the normalized J-factor is:

$$J(\psi, \Delta\Omega) = \Big(\frac{1}{\rho_c^2 R_H}\Big) \int_{\Delta\Omega} d\Omega \int \rho^2(s, \psi, \Omega) ds \tag{5.2}$$

where $\Delta\Omega$ the observed solid angle, and ψ is the direction of the line-of- sight integration, $\rho_c = 9.74 \times 10^{-30} gcm^{-3}$ is the critical density in the Universe and $R_H = 4.16$ Gpc is the Hubble Radius. The J-factor depends on the density profile of the dark matter inside the source. The density distribution follows the equation 5.3:

$$\rho(r) = \rho_s \Big(\frac{r}{r_s}\Big)^{-\gamma} \Big(1 + \Big(\frac{r}{r_s}\Big)^{\alpha}\Big)^{-\frac{\beta-\gamma}{\alpha}} \tag{5.3}$$

Since the distribution of dark matter is unknown, the authors used two different profiles: Navarro-Frank-White (NFW) profile, which sets the constant in the equation 5.3 $(\alpha, \beta, \gamma) = (1, 3, 1)$, and Burkert profile, which sets $(\alpha, \beta, \gamma) = (2, 3, 1)$. In the study of M15 the authors initially used a NFW profile. The density profile can be described by the virial mass m_{vir} and concentration c which are related to ρ_s and r_s. From the study by Bullock et al [183], the parameter c is related to *virial mass* m_{vir} (which is described in §2.1.1) by:

$$c = 9\Big(\frac{m_{vir}}{1.5 \times 10^{13} h^{-1} M_\odot}\Big)^{-0.13} \tag{5.4}$$

with an error $\Delta c \sim 0.14$.

The authors started from the study conducted by Van den Bosch [119], published in 2006, where the authors showed a profile of mass to luminosity ratio. Models for the M/L of M15 are consistent with a purely baryonic mass profile: this indicates that the mass of the DM halo must be significantly less than the baryonic mass. The hypothesized virial mass m_{vir}, is in the range from 5×10^6 to 5×10^7 $M_\odot$ and consequently c in range of 32 to 82. Because of this, and considering a NFW profile, the initial value of J can be in the 7-150 range. With evolution overtime, the adiabatic contraction of the core increased the density of the dark and baryonic matter. The authors have used the adiabatic compression model of Blumenthal et al [184] to compute the final amount of DM inside the GC. The distribution after the adiabatic contraction is denoted NFW+AC and the J factor is therefor higher by a factor ∼ 10 to

Source	Distance	Model	J_{min}	J_{max}
M15	10 kpc	NFW	7	150
		NFW+AC	8×10^3	2×10^4

Table 5.1: Estimation of the J-factor for source M15. The distribution of DM inside the GC is described by the NFW distribution and the J-factor value is inside the range showed in the last two columns. In the second row the value of the J-factor is after the adiabatic compression which increases the amount of the DM in the core [182].

10^2. Table 5.1 displays the results for M15 and the figure 5.1 shows the density distribution for $m_{vir} = 10^7 M_{\odot}$ and $c = 50$.

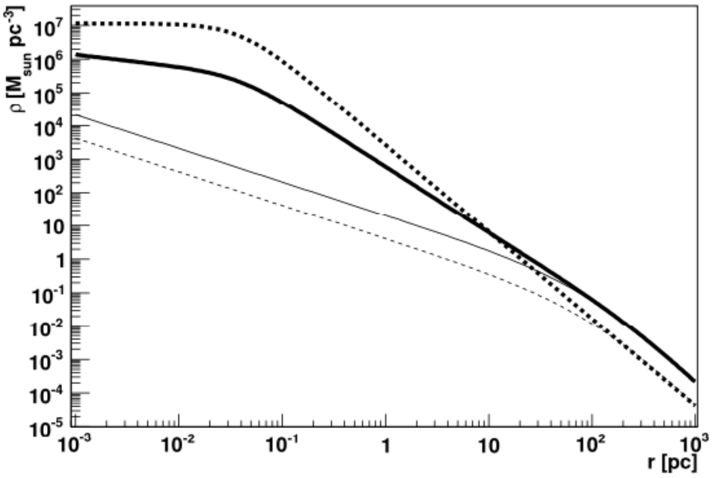

Figure 5.1: Density profile of M15 before and after the adiabatic compression. The solid lines represent the DM profile before (thin line) described by NFW profile and after (thick line) describe by NFW+AC. The dashed lines represent the density of the baryonic matter before (thin line) and after (thick line) the compression [182].

The J-factor value is usually expressed in units [$\mathrm{GeV}^2\mathrm{cm}^{-5}$] while in the table J-factor shows like a dimensionless quantity. In these units the J-factor becomes equal to 1.5×10^{19} GeV^2 cm^{-5} .

H.E.S.S. observations

After the study carried out by the Whipple collaboration, also H.E.S.S. searched signals from DM particles annihilation from the GC M15. H.E.S.S. observed

M15 during the years 2006 and 2007 and collected $\sim$ 15.2 h, in wobble mode and with a better resolution than Whipple [185].

The H.E.S.S. collaboration started from the same considerations of the Whipple team: the primordial scenario of GCs requires that GCs were formed in extended DM halos. The DM halo profile of a GC is thus modeled assuming an initial NFW profile described by equation 5.3 with $(\alpha, \beta, \gamma) = (1, 3, 1)$. The DM halo is parameterized by a virial mass M_{vir} and a concentration parameter c_{vir}. The normalization parameter ρ_s present in the 5.3 and r_s are related with the virial mass and the concentration parameters respectively by:

$$\rho_0 = \frac{M_{vir}}{4\pi r_s^3 f(c_{vir})} \qquad r_s = \frac{R_{vir}}{c_{vir}} \tag{5.5}$$

where $f(x)$ is the volume integral of the NFW profile, $f(x) = ln(1+x) - x/(1+x)$.

The baryonic mass provides a lower limit for M_{vir}. The value of M_{vir} is included between 5×10^6 and 5×10^7 $M_\odot$ corresponding to c_{vir} between $\sim$ 48 and 65. After setting these initial conditions, an adiabatic compression is applied. This increases the amount the dark matter in the core as in the Whipple study. But this time, a further process which smooths the quantity of the DM in the central region by the kinetic heating of DM by stars is also taken into account to calculate the J-factor.

In this way the modeling of the M15 DM halo proceeds in two steps following the relaxation time scale given by:

$$T_r = \frac{3.4 \times 10^9}{ln\Lambda} \left(\frac{v_{rms}}{kms^{-1}}\right)^3 \left(\frac{m}{M_\odot}\right)^{-2} \left(\frac{n}{pc^{-3}}\right)^{-1} \text{yr} \tag{5.6}$$

where v_{rms} is the velocity dispersion, n is the stellar density, and $ln\Lambda$ is the usual Coulomb logarithm given by R/r_{min}. The T_e is equal to 7×10^4 years. In the first step, the dark halo is assumed to be adiabatically compressed during the collapse of the M15 core. This step is described in the study of Wood et al [182]. The baryon distribution is known, thanks to the observations made through the use of the Sub-arcsecond Imaging Spectrograph on the Canada-France-Hawaii Telescope (CFHT) [186]. The AC takes place in a few orbital periods time which, being $\sim 10^3$ years, so much less than T_r.

The second step considers the interaction between DM particles with the SM particles. This process is the basis of the direct detection and it acquires importance in very dense environments, which are rich of neutron stars and white dwarfs or other compact objects. The DM particles can deposit their kinetic energy interacting with the SM particles into the stars and this process is called dark kinetic heating because the temperature of the stars could raise due to the energy released inside them. The capture of DM onto stars is proportional to the number of nucleons in the star multiplied by the escape velocity. The capture rate Γ_c is given by:

$$\Gamma_c = \left(\frac{8}{3\pi}\right)^{1/2} \frac{\rho_{DM}\bar{v}}{m_{DM}} \left(\frac{3V_{esc}^2}{2\bar{V}^2}\right) \sigma_{eff} \tag{5.7}$$

where ρ_{DM} is the density of DM around the star, m_{DM} is the mass of the DM particles, $\bar{V}$ is the average DM velocity, V_{esc} is the escape velocity, and σ_{eff} is the effective cross section. Once DM is captured by a star or a compact object, it will form a thermal distribution inside the star of characteristic radius r_{th}, and could self-annihilate [187, 188].

This process leads to a depletion of the amount of DM inside the heating radius $r_H \sim 5$ pc. The profile of the dark matter is showed in figure 5.2.

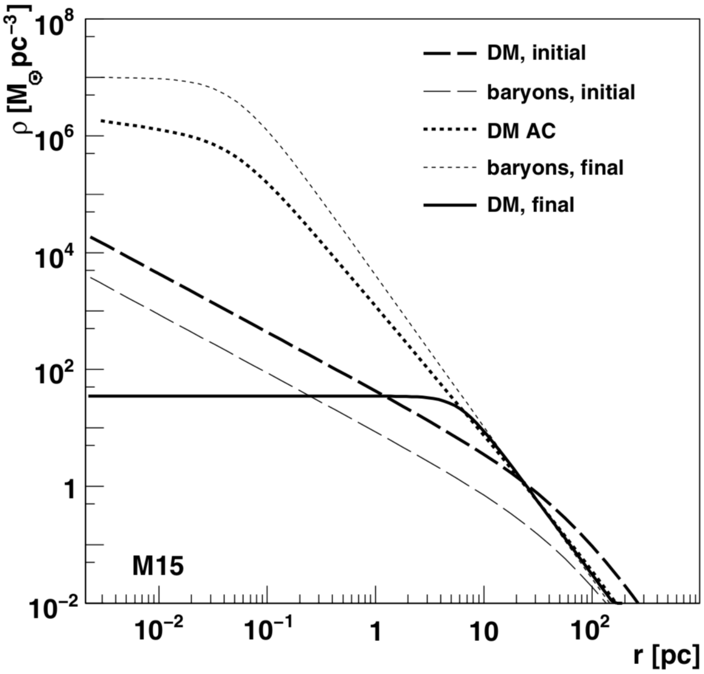

Figure 5.2: Density profile of DM and baryonic matter in M15 in function of the radius, before and after the core collapse. The initial DM distribution follows a NFW profile with $M_{vir} = 10^7 M\odot$ and the initial configuration is showed by the thin dashed line. The distribution of DM and baryonic is showed by the thin dotted line. After the adiabatic compression phase the amount of DM decreases because of the kinetic heating by stars and the final density profile of DM is plotted by the solid line [185].

The resulting J-factor is given by:

$$J(l,\Omega) = \frac{1}{\Delta\Omega}\int_{\Delta Omega} d\Omega \int_{l.o.s} \rho^2(r(s))ds \tag{5.8}$$

where r depends on the distance and θ is the opening angle of the integration cone centered on the target position, and $\Delta\Omega$ is the solid angle, which is set at 5×10^{-6} sr. The J-factor is computed for every step of the evolution of the GC and the results are reported in table 5.2. The final result for the J factor is 7×10^{19} GeV^2 cm^{-5} .

DM halo profile	M15 /10^{24} GeV^{2}cm^{-5}
Initial NFW (M_{vir}, c_{vir})	$1.5(10^7, 50)$
AC NFW	4.3×10^3
Final	14

Table 5.2: Estimation of the J-factor for M15 in every process considered. The values of M_{vir} and c_{vir} are shown inside the parentheses, together the values of the initial NFW. The results of the J factor are expressed in the units of 10^{24} GeV^2 cm^{-5}. The solid angle is $\Delta\Omega = 5 \times 10^{-6}$ sr [185].

5.2 J-factor

In the previous section I have described the works to study the source M15. In particular, I introduced the previous observations in γ-rays range by Whipple and H.E.S.S., to study the upper limits on the average cross section for velocity, using some modelling on the interaction and dynamics of DM.

My work takes the ratio M/L and the density distribution from new data. The plots are taken from Van den Brok et al [1] and are shown in figure 5.3.

The profile of the ratio M/L shows a discrepancy around 5 in the inner zone, and around 1 outside the center. When the ratio is greater than 1, the dynamical mass is greater than the mass which produces radiation. This can be explained by a missing dark mass. This mass could be constituted from compact objects like neutron stars, stellar black holes or intermediate mass black holes, white dwarfs, and/or non baryonic dark matter. Figure 5.3 shows the amount of density as a function of radial distance from the core: plot (a) shows the ratio between mass and light, plot (b) shows the total density

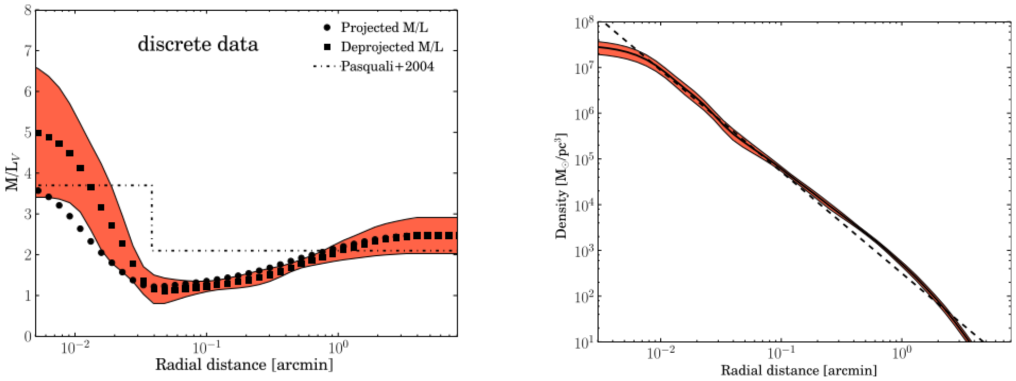

(a) The mass-to-light(M/L) profile of M15

(b) The density distribution

Figure 5.3: The plots show the distribution of the total density (plot b) and the M/L distribution (plot a) whose are taken by Van den Brok et al [1].

distribution. The density decrease very quickly: from $\sim 10^{-3}$ arcmin to 1 arcmin the value of the density changes of several orders of magnitude, from 10^7 to $\sim 6 \times 10^2$ M$_\odot$/pc^3.

Due to the high density it is impossible for us to be able to resolve objects within the cluster core. To get an idea of the amount of dark objects (like neutron stars, black holes and white dwarfs) and dark matter it is necessary to use theoretical models which, taking into consideration the interaction between stars and interaction of dark matter with ordinary matter, can predict the quantities of each cluster component.

Waiting for the construction of evolutionary models concerning M15 we can think that the amount of the DM inside the cluster is given by:

$$\rho_{DM} = f\left(1 - \frac{1}{M/L}\right)\rho \tag{5.9}$$

where the factor f ranges between 0 and 1 and represents the percentage of dark matter inside the cluster. In the first step of the analysis we consider the missing mass completely composed by dark matter, $f = 1$. This hypothesis, set an upper limit to the amount of dark matter, will allow us to have an idea of the maximum amount of dark matter.

In figure 5.4 is displayed the total density profile and dark mass profile in the cluster which is computed from the combination between density and M/L and with $f = 1$.

M15 source is approximated as a sphere so, in spherical symmetry, each values on $x-$axis in the plots reported in the figure 5.3 represent spherical shell

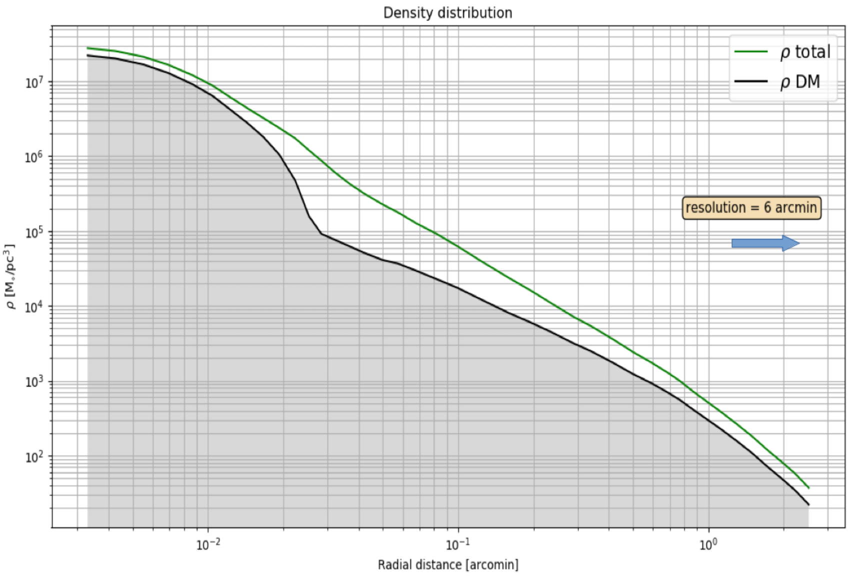

Figure 5.4: Taking the data from Van den Brok et al [1] and under the maximal assumption that all the missing mass is made up of DM, it is possible to show the total density (green line) and the amount of the DM density (black line).

with radius R, with a certain density.

The line of sight (l.o.s) is the line which starts from the telescopes and crosses the M15 surface (at C) and its inner spherical subdivisions until leaving the source at point D, like in figure 5.5.

In equation 5.8 the term ds is the linear part of the increment of l.o.s. and its length is given by the integral $\int_{l.o.s} ds$.

The geometric of the problem can be illustrated in figure 5.6. The observer is located in the origin of the XY plane ($observer \equiv O$) while the center of the source is located on the $x-$axis at distance D end it is equal to 10.5 kpc. The M15 radius is equal to the distance between the point A and C, $\overline{AC}$ while the l.o.s. is the chord $\overline{CD}$. Figure 5.6 is not in scale because the distance between the observer and the source is much greater than the radius of the GC.

The angle θ is the angle between the line which crosses to the source center and the l.o.s. and corresponds with the value of radial distance in the plots in figure 5.3. When $\theta = 0°$, the l.o.s is parallel to the $x-$axis and crosses the center of the source. As the angle grows point C moves away from line D means that the observers is observing the source away from the center.

The biggest problem is being able to find a correct parametric description of the line of sight in order to calculate the innermost integral of the J factor, that is writing the integral $\int_{los} \rho^2 ds$.

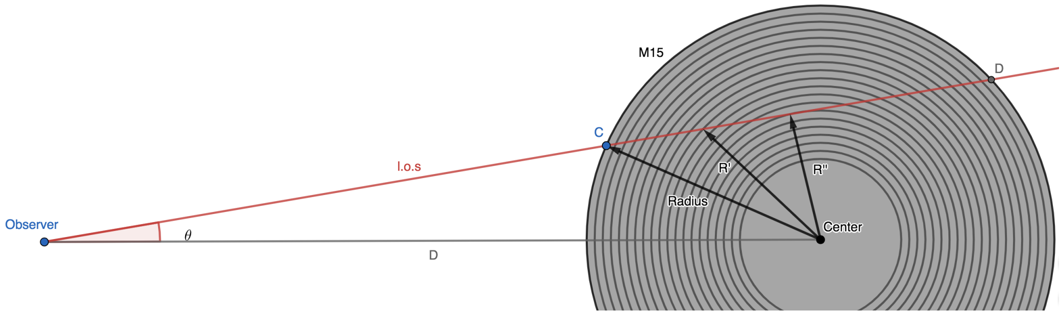

Figure 5.5: The line of sight is the imaginary line which follow the direction where the observer is looking. M15 is represented like a lot of spherical shell and the l.o.s. touches some shell in one point at distance R.

The data are shown in table 5.3 and are taken from the article and the bibliography about M15.

Data	Value
Distance (D)	10.4 kpc
R	0.027 kpc
R_{max}	0.011 kpc
θ_{max}	3.5515275 arcmin
θ_{min}	3.299×10^{-3} arcmin

Table 5.3: Data used to compute the J-factor. M15 is located at 10.4 kpc, R is its radius and has a diameter equal to 0.054. The source was observed with an angle which changed in the $\theta_{min} - \theta_{max}$ range, which at biggest θ corresponds a radius R_{max}

If we consider the chord $\overline{CD}$, we must start from a well-known theorem that links the chord with the angle in the center and called *"Perpendicular bisector"*.

Theorem 5.2.1 *The perpendicular bisector of a chord passes through the centre of the circle.*

This entails both the chord is split in two equal parts, the first segment $\overline{CE}$ and second segment $\overline{ED}$, and the angle in the center is divided in two equal parts called γ in the figure 5.6.

From theorem 5.2.1 it is possible to trace a line normal to each chord which starts from the center and finish in the middle of the chord. The volume dS^3 is define like the infinity volume of the l.o.s. and contains the mass $M(R)$ which is defined by the value of density $\rho(R)$ at distance $\bar{R}$. In spherical coordinates, each values on $x-$axis in the plots in figure 5.3 represent spherical shell with a certain density. The minimum value of the vector $\bar{R}$ is equal to the length of the perpendicular bisector, called R_{min}, and the maximum value is equal to the radius of M15 while .

While the point of the origin of the vector $\bar{R}$ is fixed in the center of the circumference, the other extremity runs on the segment $\overline{CD}$. In figure 5.6 the geometry is described on the XY plane (Cartesian coordinate system) where the observer is located in the origin of this plane. I call this frame with the term $\mathcal{K}$. In this frame it is very hard to find a correct formula to describe the variation of $\bar{R}$ on the line of sight for each θ angle. It is more easier to describe the variation of $\bar{R}$ from another point of view by a new observer. I locate the second observer on the center of the circle, where is located the point A, and I call the second frame with the letter $\mathcal{K}'$ where its axes are called X' and Y', whose intersect in the origin point O'. In the figure 5.6 is showed the second frame $\mathcal{K}'$ in red colour.

In this way a point can be described in coordinates (X, Y) and in coordinates (X', Y'). The transformation allows to pass from the first frame $\mathcal{K}$ to second frame $\mathcal{K}'$ is given by the equation 5.10:

$$\begin{pmatrix} X' \\ Y' \end{pmatrix} = \begin{pmatrix} \cos\theta & -\sin\theta \\ \sin\theta & \cos\theta \end{pmatrix} \begin{pmatrix} X \\ Y \end{pmatrix} + \begin{pmatrix} D \\ 0 \end{pmatrix} \tag{5.10}$$

where θ is the angle of l.o.s and D is the distance between the Earth and the center of M15.

From equation 5.10 is easy to see that the second frame follows the direction of the perpendicular bisector of a chord and, reminding the theorem, the cord is split into two equal parts. The geometry seen by the second observer is shown in figure 5.7:

In the frame $\mathcal{K}'$

a) the *x-axis* is parallel to the bisector for every l.o.s;

b) from the theorem 5.2.1 the l.o.s. is split into two equal parts: one is over the *x-axis* and the other one is below it;

c) every point of the l.o.s. can be expressed in polar coordinate (r, ϕ) and we call the $\bar{R}$ the vector that link the center with point dS.

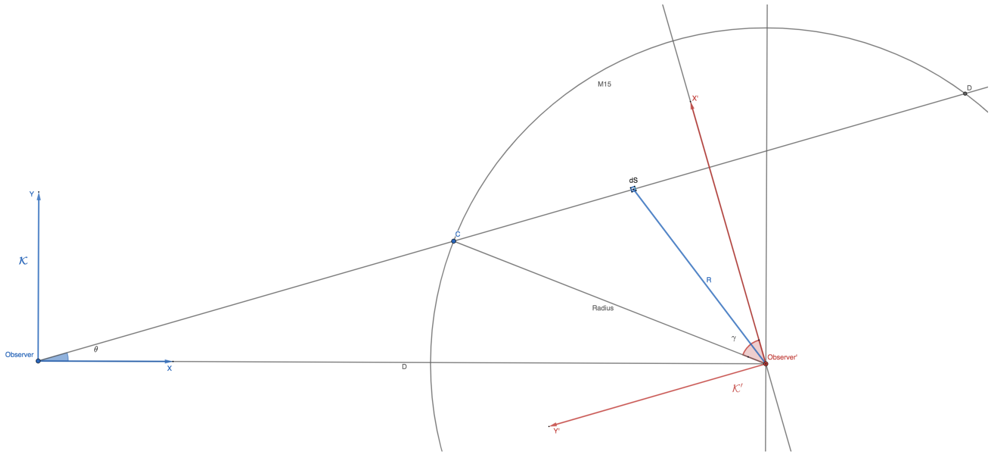

Figure 5.6: It is displayed the geometry of the problem. The picture is not in scale. The second frame $\mathcal{K}'$ has the origin located in the center of the circle and it is shown by the red line.

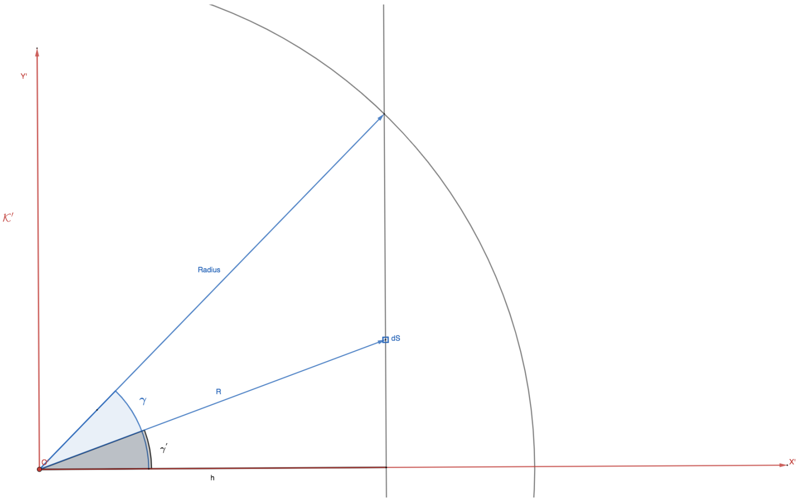

Figure 5.7: The second observer sees the l.o.s. like line which is perpendicular his $x-axis$. The distance between one point on the line and the center is equal to $\bar{R}$.

The element dS can be expressed with the radial vector $\bar{R}$ which is function of the length r and the angle γ. So, the small variation of ds has coordinates describe by $\bar{R}(dr, d\gamma)$.

The system loses one of freedom degree because the vector $\bar{R}$ is bound to stay on the l.o.s. so it is possible to express the position of ds both the length r or the angle γ. Under those conditions it is possible to change the variable in the integral from ds to dr .

$$\int_{l.o.s.} \rho^2(s)ds \Rightarrow 2\int_{R_{min}}^{Radius} \rho^2(r)dr \tag{5.11}$$

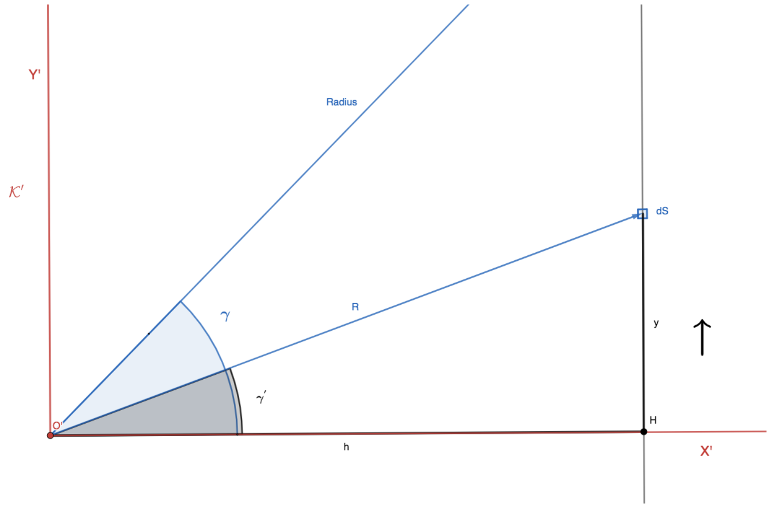

Figure 5.8: The parameter dS moves on the l.o.s. and forms a triangle with leg x and y and hypotenuse R.

Computing the length of $\bar{R}$ it is possible to use the Pythagorean theorem on the right triangle, $\triangle O'dsH$ with leg respectively h and y, shown in figure 5.8.

Side h is the perpendicular bisector of the chord while side y is the distance of the elements dS from the $x'-$axis. Side R is the hypotenuse which subtends angle γ' with the $x-$axis.

Side h is constant because for a given angle θ only one perpendicular bisector h is found. Thus, it is possible to express the J-factor using only the opposite side y and its variation dy.

In this way the parameter r becomes $r = \sqrt{h^2 + y^2}$ and integral 5.11 becomes:

$$\int_{l.o.s.} \rho^2(s)ds \Rightarrow 2\int_0^{y_{max}} \rho^2(\sqrt{h^2+y^2})\frac{y}{\sqrt{h^2+y^2}}dy \tag{5.12}$$

where y_{max} is given by $y_{max} = \text{Radius} \cdot \sin\gamma$.

The J-factor is a measure of square density of DM across the l.o.s. within the solid angle $\Delta\Omega$ and passing through the source. Therefore the integral of the J-factor is given by:

$$\boxed{J = 2\pi\frac{R^2}{D^2}\int_0^{\theta_{max}}\int_0^{y_{max}} \rho^2(\sqrt{h^2+y^2})\frac{y}{\sqrt{h^2+y^2}}dyd\theta} \tag{5.13}$$

where R is the radius of the source and D is its distance from the observer.

The integral was computed using the mean values taken from the plots in figure 5.3(a) and figure 5.3(b) and the result of the integral is:

$$\boxed{J = 3.9626 \times 10^{23}\frac{\text{GeV}^2}{\text{cm}^5}} \tag{5.14}$$

and its behaviour as a function of the radius is displayed in figure 5.9.

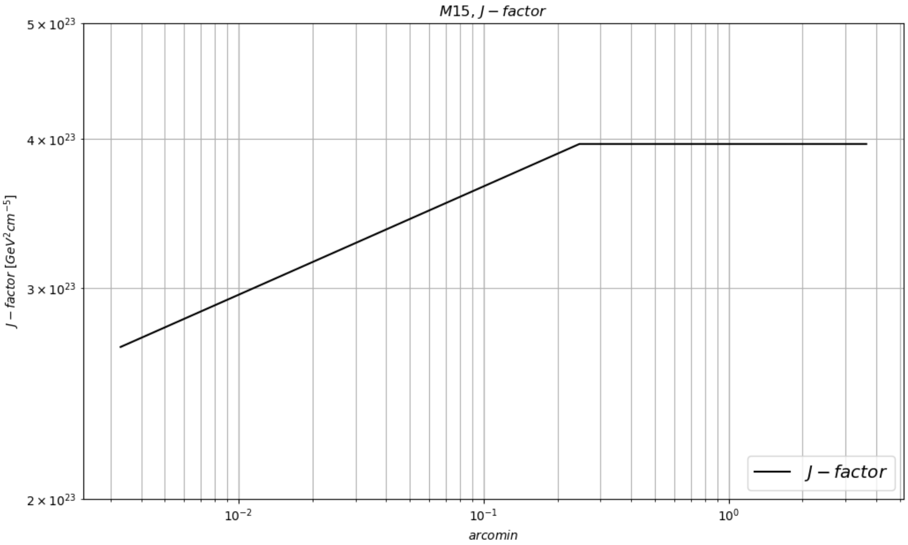

Figure 5.9: The amount of J-factor which was computed as in section 5.2. The increase of the amount of the J factor at large θ becomes negligible.

Because of the high slope of the density for increasing radial distance and the fact that it is squared in the integral, the inner part of the density distribution dominates the J-factor.

5.3 The error on J-factor

In the figure 5.3 the plots show both the mean value of the measures and also their uncertainties. The error of the measure has a Gaussian distribution: red area around the mean value is the 1σ confidence interval and this is valid both for mass-to-luminosity ratio profile (figure 5.3(a)) and also the density profile (figure 5.3(b)). The two physical quantities are independent each from other and the error on the J-factor quantity descendes from the propagation of those two uncertainties in equation 5.13. The relation is not linear and it is not easy to propagate the error and estimate a real value therefore I applied a Monte Carlo method.

Monte Carlo simulation for uncertainty propagation take as inputs the uncertainty distribution for each variable and an equation for the calculation of a desired quantity.

Let X be a random variable having distribution function F_X and let $f : \mathbb{R} \to \mathbb{R}$ be a function. The expected value is given:

$$E[x] = \int_{-\infty}^{+\infty} f(x) dF(x) \tag{5.15}$$

It is possible to generate a sample n with a great number of draws x_1, ..., x_n from the distribution F_X. For the *law of large numbers* (LLN) there is convergence to the mean. In this way the equation 5.15 becomes:

$$\begin{gathered} \frac{1}{n}\sum_{i=1}^{n} f(x_i) \longrightarrow E[f(x)] \\ \int_{-\infty}^{+\infty} f(x) dF(x) = \frac{1}{n}\sum_{i=1}^{n} f(x_i) \end{gathered} \tag{5.16}$$

5.3.1 Calculation Method

I assumed that the density ρ and M/L distributions follow Gaussian distributions around the mean at each value of the radius. It is possible to image the plots in figure 5.3 in three dimension: on the xy plane it is showed the value of the measure in function of the radial distance, while on the yz plane we should see the Gaussian distribution for every point.

For each simulation I extract two numbers: one called α in reference to the radial density distribution and the other, called β, in reference to the M/L plot. The numbers extracted are independent of each other but each one follows Gaussian distribution which is given by:

$$f(y) = \frac{1}{\sigma\sqrt{2\pi}} e^{-\frac{1}{2}(\frac{y-\mu}{\sigma})^2} \tag{5.17}$$

where the y is the value of the y-axis, μ is the mean or expectation of the distribution, and in the our case this value is given by the mean values on the plot in figure 5.3, and σ is the deviation standard, which is given by the borders of the red area in the same plots that are the 1-sigma contours.

The standard normal distribution is the simplest case of Gaussian distribution, with $\mu = 0$ and $\sigma = 1$ and it is symmetric around $y = \mu = 0$. Every normal distribution is a version of the standard normal distribution, whose domain has been stretched by a factor σ and then translated by μ (the mean value):

$$f(y|0,1) = \frac{e^{y^2/2}}{\sqrt{2\pi}} \Rightarrow f(y,\mu,\sigma^2) \tag{5.18}$$

In this way every draw of the number α and β may follow standard normal distribution, with $\mu = 0$ and $\sigma = 1$, and then they shift on the Gaussian distribution with $\mu = \bar{\rho}$ in one case and $\mu = \overline{M/L}$ in other case.

For every extraction we are interested the value on x-axis of the number drawn because that value is represented the distance from the mean measured value in units of the σ. The values α_x and β_x translate the curves of the plots up, if their x-values are major than 0, or down, if the x-values are minor than 0. The new profile is given by the equations:

$$\rho_{new} = \bar{\rho} + \alpha_x \cdot \sigma_{\rho_+} \tag{5.19}$$

$$\mathrm{M/L}_{new} = \overline{\mathrm{M/L}} + \beta_x \cdot \sigma_{ML_+} \tag{5.20}$$

if the value of α or β is upper than 0. In the other case, if the value is negative it use the lower bounds. Then the two number extracted are independent each other, it is possible to have every combination of them. At this point I have two new different profile in density and M/L and it is possible to compute the J-factor for that configuration.

In the figure 5.10 two extractions are shown. The point α has $x = 0.476$

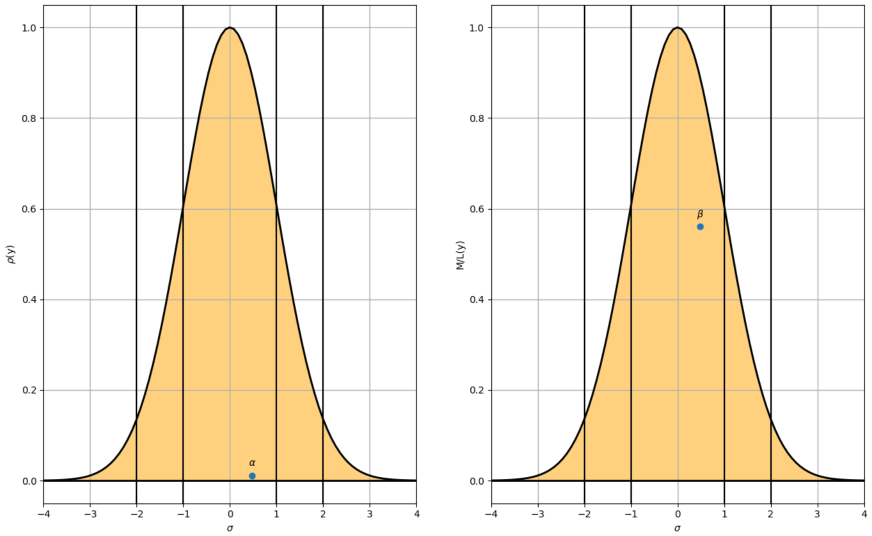

Figure 5.10: It shows an example of extraction of the two numbers α and β. On the x-axis the value 0 is the mean value μ while the numbers indicates the σ values.

while the point β has $x = 0.485$. These value represent the distance between the μ value, respectively from $\bar{\rho}$ and $\overline{M/L}$. Following the equations 5.19 and 5.20 the two new profile are obtained. Those profile are shown in the figure 5.11 and figure 5.12 respectively.

The new profiles will be used to compute the J-factor using the same algorithm of equation 5.13. In this specific case the density inside the M15 is increased and also the ratio between mass and luminosity is also greater than the mean value. Indeed the amount of the J-factor exceeds the amount 5×10^{23} $\mathrm{GeV}^2/\mathrm{cm}^5$ and the new profile is shown in figure 5.13.

The mass-to-luminosity ratio indicates how the density of dark matter contributes the total of density of the source. The ρ of the dark matter is given by the equation 5.9:

$$\rho_{DM} = \left(1 - \frac{1}{M/L}\right)\rho$$

The problem arises when the value of the β is over -2σ: when the M/L profile is less than 1, the ratio becomes over 1 and the quantity $1 - 1/(M/L)$ is lower than 0. This solution does not have sense and this bug leads random amount of J-factor as seen in figure 5.14. In light of this the allowed range where it is possible to draw β starts from -2σ and goes to $+\infty$.

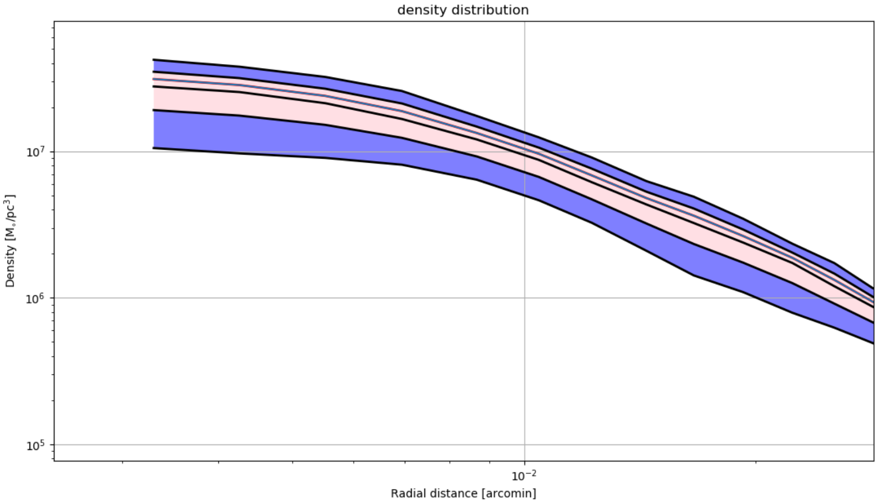

Figure 5.11: This plot is an enlargement of the density profile. The black line in the middle is the $\bar{\rho}$ which is taken from the original plot. The pink area is the 1σ region, also it is taken from the original plot. The blue area is 2σ region. The blue line close to the $\bar{\rho}$ is the new density profile which will be used for the simulation.

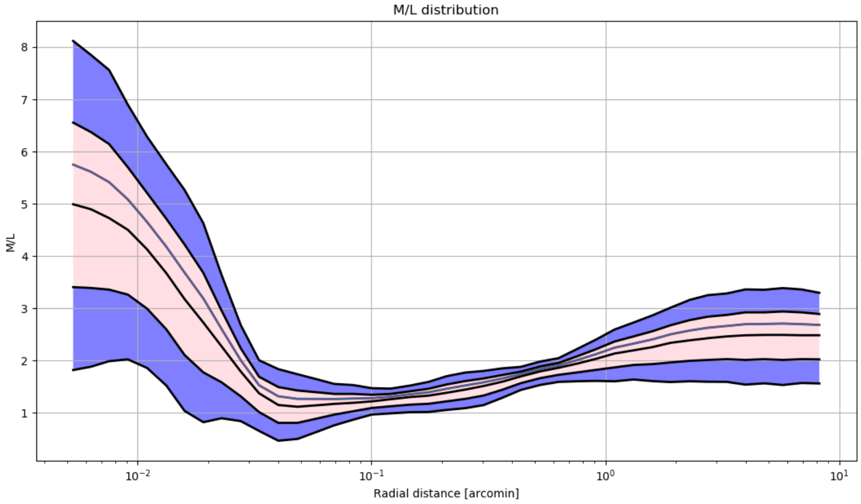

Figure 5.12: It shows the new M/L distribution. The black line in the middle is the average $\overline{M/L}$. The pink area is the 1σ region. Both the value are taken from the original plots. The blue are is the 2σ region and the blue line is the new profile of the M/L distribution.

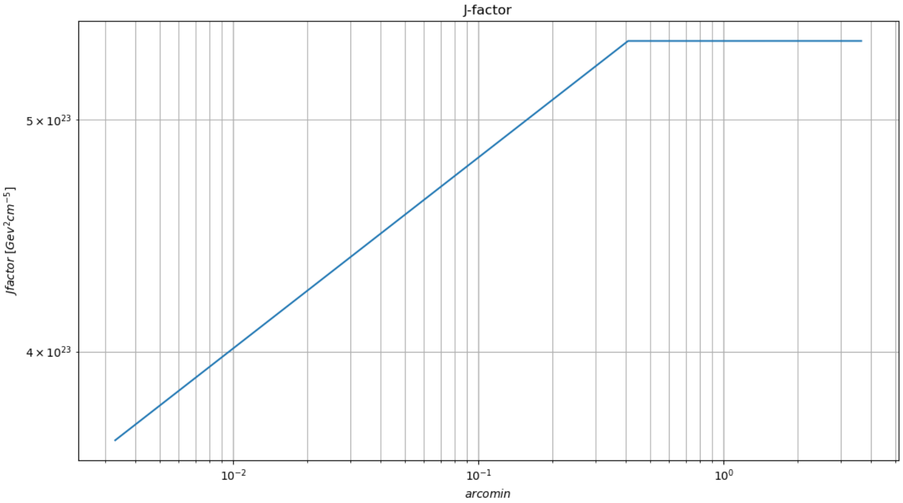

Figure 5.13: The J-factor profile obtained with the new profiles of density and mass and luminosity ratio.

The different results of J-factor will be positioned around an average value and, from their distribution, it will be possible to extract the standard deviation with the common statistic formulas:

$$\bar{J} = \frac{1}{N-1} \sum_i J_i \tag{5.21}$$

$$\sigma_J = \sqrt{\frac{\sum_i (J_i - \bar{J})^2}{N-1}} \tag{5.22}$$

The mean value and the standard deviation of the J-factor are:

$$J \pm \sigma = (4.0503 \pm 2.2453) \times 10^{23} \frac{\mathrm{GeV}^2}{\mathrm{cm}^5} \tag{5.23}$$

and it is possible to compare with the J-factor which was computed from the

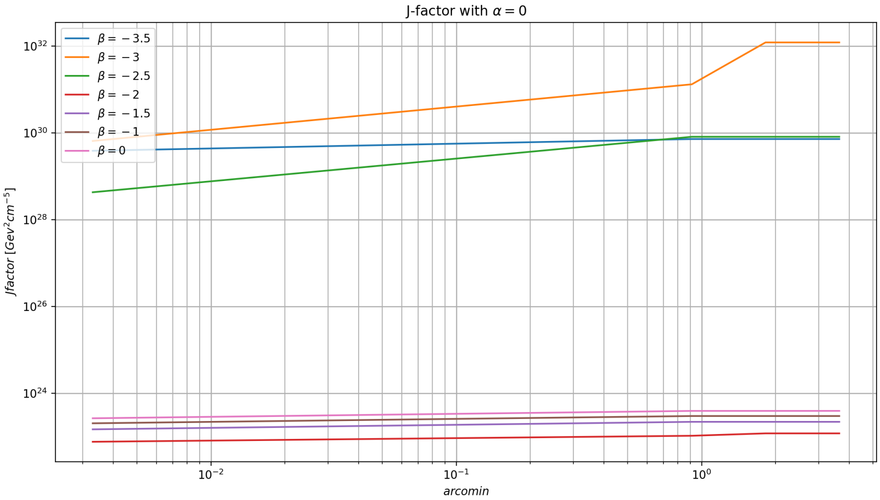

Figure 5.14: J-factor for different values of β with α fixed at value 0. The value of β is given in multiples of the standard deviation. The mean value is given with $\beta = 0$. When the value of β is below than -2σ the amount of dark matter is over the total mass and it is not meaning to compute the J-factor.

measured ρ and M/L profiles in equation 5.14:

$$J_{true} = 3.9626 \times 10^{23} \frac{\mathrm{GeV}^2}{\mathrm{cm}^5} \tag{5.24}$$

$$\bar{J} - J_{true} = (4.0503 - 3.9626) \times 10^{23} = 0.0877 \times 10^{23} \frac{\mathrm{GeV}^2}{\mathrm{cm}^5} \tag{5.25}$$

The distribution of the value of the J-factor is displayed in the figure 5.15 in logarithmic scale. The number of simulations is 2089 and the values that I found are:

$$log_{10}\bar{J} = 23.607492 \tag{5.26}$$

$$\sigma(log_{10}J) = 0.27128238 \tag{5.27}$$

This results will be used to compute the upper limits on the the $< \sigma v >$ for different masses of the dark matter particles.

Limit on cross sections calculated in this way are clearly over optimistic and represent at most a “maximal” constraint given that only a fraction of the

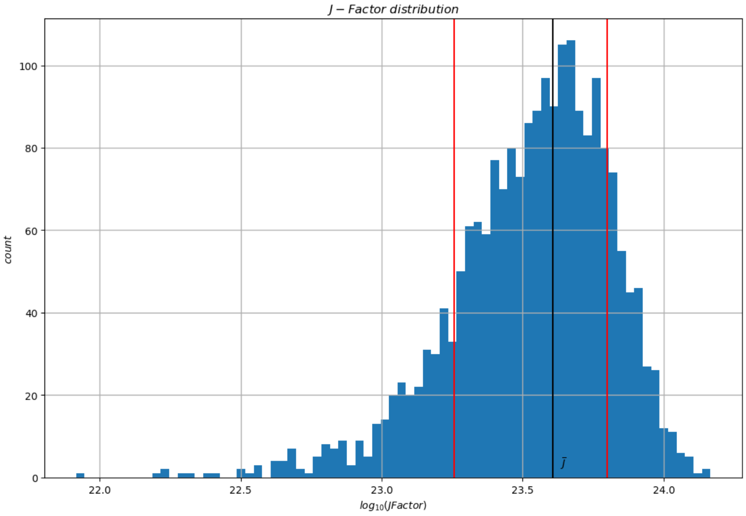

Figure 5.15: $J - factor$ distribution in x-logaritmic scale. The red vertical lines rapresent $-\sigma$ and $+\sigma$ while the black line is the mean value of the distribution.

missing mass is actually due to DM as it is shown in figure 5.16. Therefore I assumed a model not dominated by DM adopting a $f = 0.01$ inside the equation 5.9 and in further computations. With this assumption, the value of the J-factor is 4.27×10^{19} GeV^2 cm^{-5} which corresponds 19.63 in logarithm scale with an error $\sigma = 0.28$.

5.4 Data analysis

MAGIC observations of M15 (NGC 7078) started in 2015 and lasted until September 2016, three months per year; $\sim$ 170 h were taken in total. The data was collected in wobble mode: the source is not in the center of the field of view but is located at 0.4 deg from it and the antisource is in the opposite place on the camera as see in figure 5.17. The distance between the source and the center of the camera is called *wobble distance* and it is indicated with the letter w. The source is placed at an offset equal to w and the antisource is placed at the same offset but with an angle 180° from the source. M15 was observed with an offset $w = 0.4$ deg in 4 different position at angles correspond at $0°, 90°, 180°, 270°$ between the R.A. axis and the offset direction and measured in the direction of Dec axis. So in the wobble mode observation every 20 minutes, M15 moved on other position on the camera so the source

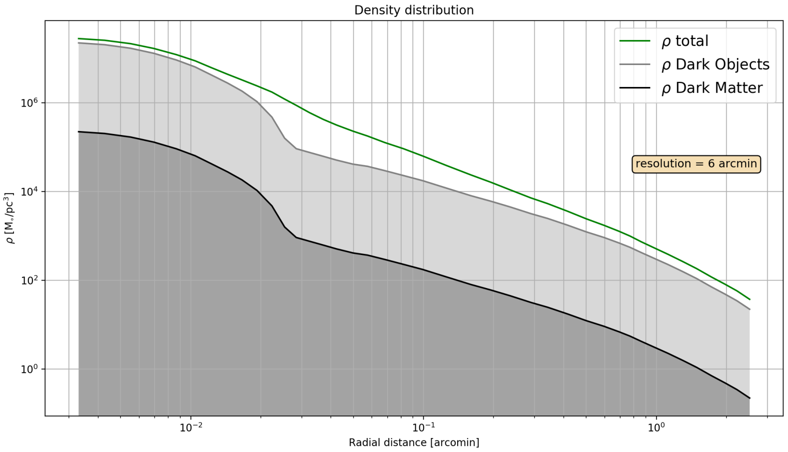

Figure 5.16: Under the hypothesis that 1% of the missing matter is made up of dark matter and the remaining 99% of missing mass is made up by dark objects, in the plot the different profiles for each component are shown as a function of the radial distance from the center of M15.

was first in 0° and then in 180°, next at 90° and then in 270°.

For the study of dark matter is required that the data survives certain quality cuts to reduce the noise as much as possible. The most important cut are:

- Lidar transmission is above 80;
- Zenith is started from 5° to 35°;
- cloudiness below 45%;
- moonless night, in total darkness;
- average median DC current not larger than 2μA.

These requests are very strict but are also necessary because the number of expected photons is not high and we try to maximize the sensitivity to signals events while minimizing noise as much as possible.

The cuts were applied on every run of data collected for each telescope, M1 and M2, on the *Star* data. The total observation after the cuts are 84.6 hours in the first period and 56.4 hours in the second periods in total the first cut reduce the hours from 170 h to 138 h.

Then the data of M1 and M2 were merged to recreate the stereoscopic vision. Only for my peace I also checked the cuts on the stereoscopic data and

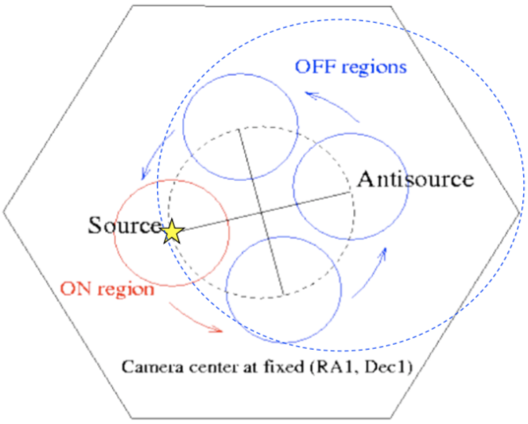

Figure 5.17: The scheme of the wobble mode observation. The source is no located in the center of the camera but at a distance $w = 0.4$ deg from it. The antisource is located in the opposite place of the source on the camera. Every 20 mins M15 is moved on other position.

I report some plots of the most important parameters in the figures 5.18, 5.19, 5.20.

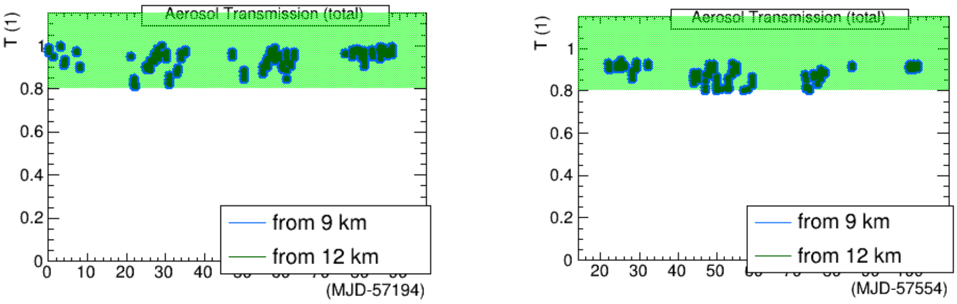

(a) (b)

Figure 5.18: The Lidar transmission at 9km is a parameter that indicates the transmission of the light in atmosphere until 9 km above the level of sea. For this analysis I have chosen only the data with Lidar transmission > 0.8. The plots are taken after to check the cut on Superstar data collected in the Cycle X (figure **a**) and Cycle XI (figure **b**).

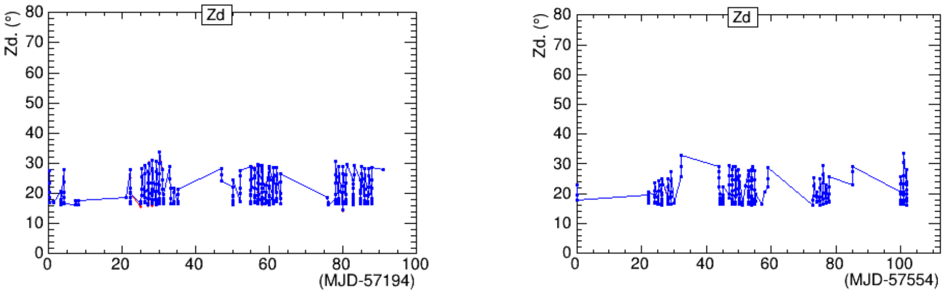

(a)

(b)

Figure 5.19: M15 was observed with low Zenith angle. I applied the cuts on the Zenith angle on Star data so all the data which were collected with Zenith$<35°$ have been chosen. The plots are taken from the check on the Superstar data in both the Cycles: **a** represents the Cycle X and **b** the Cycle XI.

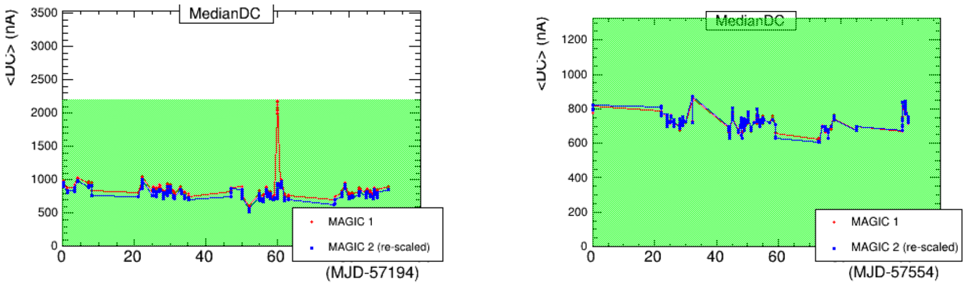

(a)

(b)

Figure 5.20: The level of the DC current indicates the level of the noise in the camera. The data were collected in total darkness so it is requested low values of current. The threshold is 2.2μA. The plots are taken from the check on Superstar data and figure **a** represent the data collected during the Cycle X and the figure **b** represent the data of the Cycle XI.

5.4.1 Definition of the region of interest

In section §5.2 the J-factor is a function of the aperture used for signal extraction which was denoted with the Greek letter θ. The research of the signals from self-annihilation, is strong depends from the angle θ. In MAGIC analysis we define a circular aperture for signal search around the source defined by θ_c. Given a source which is located on the camera of the telescope, we define with w the distance between the source and the center of the camera, and with the letter θ is the radius of the circumference around the source. So the parameter θ^2 defines the area of the circle where we search the signals.

To optimize the sensitivity is necessary to optimize both also the parameter h hadroness and the region θ [189]. For a point-like source the hadroness and the θ are optimized using a sample of Crab Nebula observations. In our case the signals from DM annihilation are expected to have another emission spectrum and the Crab Nebula is not a good test bench so it is necessary to compute the best value of hadroness and the region where we search the signals.

In order to find the best parameters I used fast MC which simulate random events. For each values of parameter θ an h I did 50 MC and select the values of them that optimize my result for the best sensitivity. The best sensitivity is the sensitivity with the lowest result in the measured on $\langle \sigma v \rangle$ plot.

I started to compute the best value of θ because the first step is to understand the region of the source. I changed the parameter θ^2 in a range between 0.01 deg^2 and the maximum value 0.02 deg^2 with steps by 0.002 deg^2. The bottom limit $\theta^2 = 0.01$ deg^2 ($\theta = 0.1^\circ$) is chosen because it corresponds with the resolution of MAGIC: it makes no sense to study signals at values below $\theta = 0.1^\circ$ if the instrument cannot discriminate them.

At the same time M15 is a point-like source for MAGIC given that the whole amount of dark matter is included within ~ 4 arcmin ($\sim \theta = 0.07^\circ$).

In order to this we would expect the θ value close to 0.1° but, because of statistical fluctuations, the imagine of M15 will not appear as a point on the camera but as figure on the map with width equal to $\theta > 0.1^\circ$.

To find out the region it is necessary to see the sensitivity in function of both DM particles mass and θ. The result is shown in figure 5.21 where have been plotted the ratio between sensitivity on maximum sensitivity as a function of θ, for several masses and for a fixed value of hadroness cut ($h = 0.15$). The denominator, which is maximum sensitivity, is connected with the highest value of cross section for a WIMP with a given mass. The numerator, which is sensitivity, gives an information about the value of the cross section for WIMP with a given mass as a function of θ^2. So every curve represents the behaviour of the cross section as a function of the distance from the center of the source. Since we are searching the minimum value of cross section for WIMPs that can be detected by the telescope, we have to look for which θ value corresponds to the minimum for most of the sensitivity for each WIMP. In this way the area where the signal is circumscribed is given from θ^2 value where there are more points which have the minimum value. The best sensitivity is obtained with $\theta^2 = 0.016$ deg^2, which corresponds to $\theta = 0.126^\circ$.

When the region is defined I find out the h which maximizes the sensitivity. The other parameter h was chosen either setting up different values of h per bin, or in estimated energy ($h(E)$) setting up γ-ray efficiency target in the MC events. I did two different plots which were analogous to the previous step. In

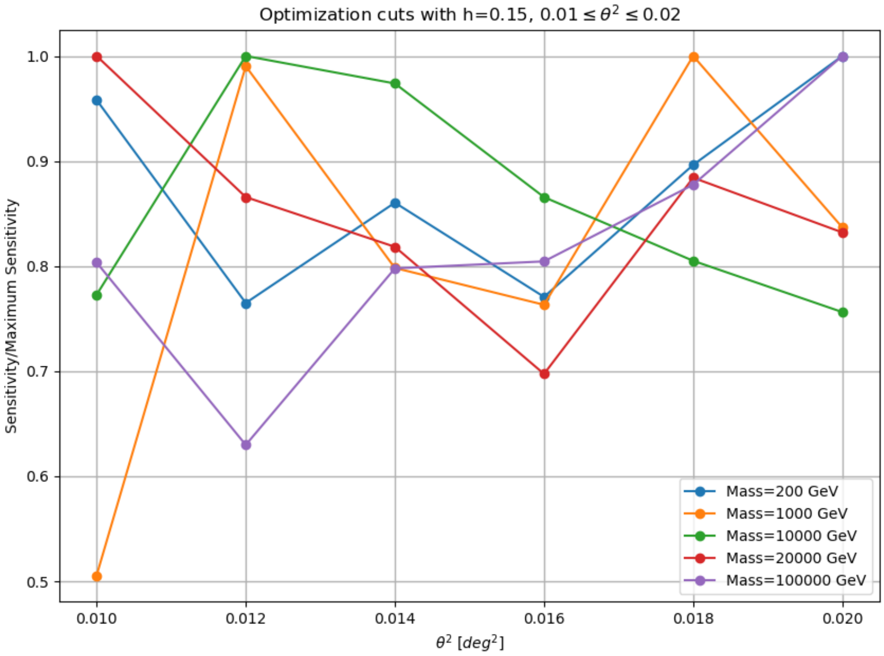

Figure 5.21: Sensitivity to maximum sensitivity ratio in function of several DM masses and fixed hadroness cut ($h = 0.15$). The sensitivity is computed for the thermally averaged annihilation cross-section considering the $b\bar{b}$ channel.

this case the θ^2 value is fixed at 0.016 and the hadroness changes in a range from 0.1 to 0.3 in steps of 0.05, while *h(E)* changes in a range from 70% to 90% in steps of 5%. From the plots it was possible to distinguish the best region where the parameters minimize the sensitivity so I kept only the values of h and *h(E)* with the smallest cross section. As all of these values of the sensitivity were more close to each other and it is impossible to discern the best value of hadroness from other values, for this part I have preferred to see the difference directly on thye plot of $\langle \sigma v \rangle$ as a function of all of masses. The several sensitivities are drawn on the same canvas and the results is displayed in figure 5.22 and the most little cross section is obtained with the $h = 0.2$.

The best sensitivity for most of the DM mass range scanned is obtained for values of $\theta = 0.126°$ and h $= 0.2$, and from this result, these values we are used in the next steps of the analysis.

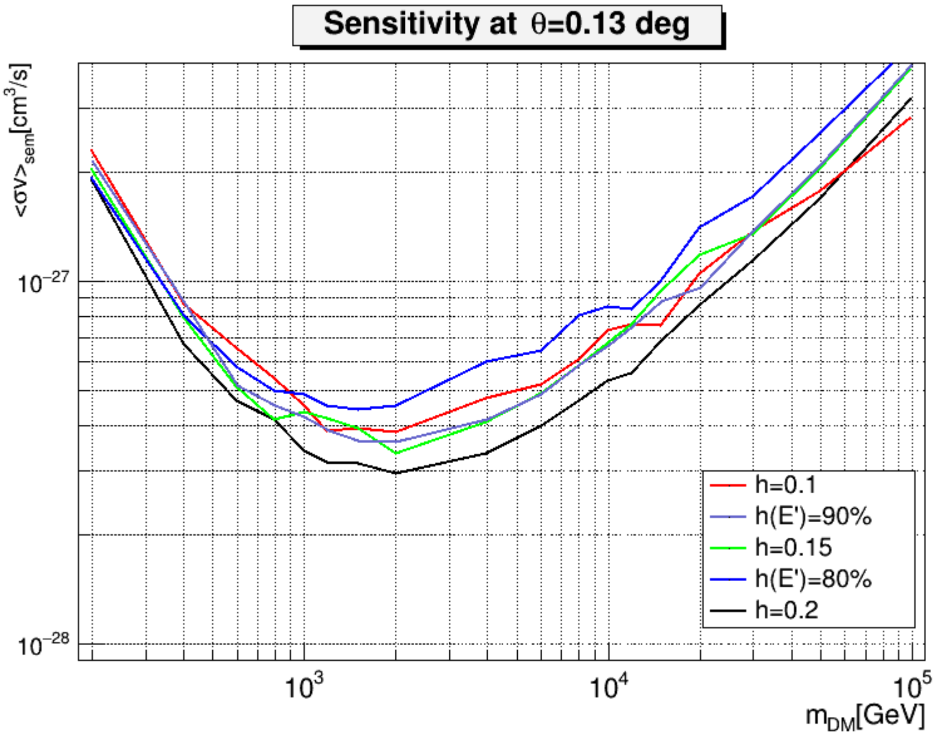

Figure 5.22: $\langle \sigma v \rangle$ computed in function of DM masses between 200 GeV and 100 TeV annihilating into a $b\bar{b}$ pair. On the canvas are reported the different sensitivities in function of h and $h(E)$ at fixed $\theta^2 = 0.016$ deg^2.

5.4.2 High level Analysis

The first results checks for the presence of the signals from the source. The histogram which is drawn in figure 5.24, shows the number of signal events from the source and from the background in function of θ^2. The source is located at 0 on the *x-axis* and each value of θ^2 represents a circular crown with width equal to the bin. After 138.04 hours of data collected, 31252 events (N_{on}) are $\gamma-$ray candidates that where found inside a circular region of radius $\theta = 0.126°$, and $\sim$ 31654 (N_{off}) are background events. The significance is computed following the Li&Ma method [180] and no source was detected. Only for point-like sources the software computes the PSF and also the optimal cut value in θ^2 range. The cut value recommend is $\theta^2 = 0.017$ deg^2 and it is close to the optimal value that I found in section 5.4.1.

The sky-map in figure 5.24 shows the test significance maps in function of σ. The figure is centered on M15 and also in this case there are not significant excesses of events over the background.

After the standard analysis it is necessary to proceed with the full likelihood

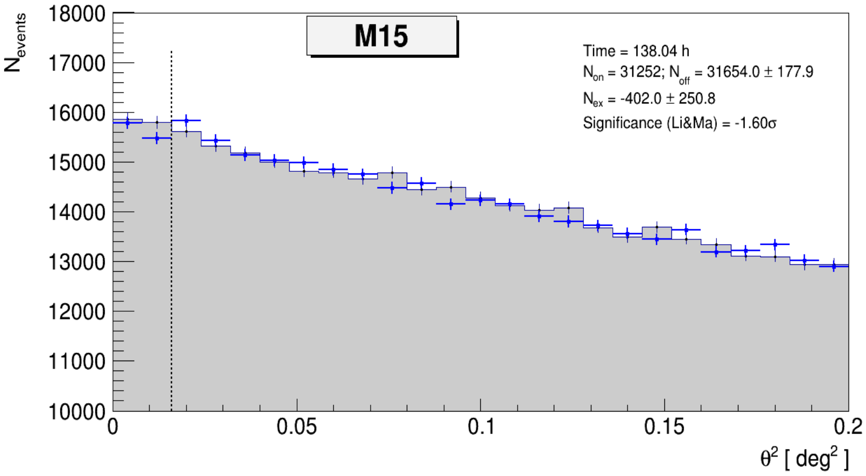

Figure 5.23: θ^2 plot shows the number of ON events (blue cross) and OFF events (grey area). The significance is given by $Li\&Ma$ equation. The region between zero and the vertical dashed line ($\theta^2 = 0.016$ [deg^2]) represents the ON and OFF integration regions.

method (FL) in order to calculate the mean γ-ray flux per annihilation process (dN/dE) for DM particles of masses into the SM pairs of quarks $b\bar{b}$, leptons $\mu^+\mu^-$ and $\tau^+\tau^-$, bosons W^+W^-.

The method is applied on each wobble position, on a Zenith range between 5° and 35° per period of observations as seen in table 5.4. Some of the parameters are shown in the figure 5.25 and these values will be used in the FL methods. As seen in section 4.3, the FL method requires some parameters in input (for example A_{eff}, the energy estimated (E_{est}) and energy true (E_{true}), the normalization τ, differential rates from the background (B) and source (S)) to improve the sensitivity [181].

HSP	Cycle X	Cycle XI
Zenith angle	5-35 deg	5-35 deg
Wobble pointing	0.4°	0.4°
Wobble angle	0, 180, 90, 270	0, 180, 90, 270

Table 5.4: List of the parameters for every cycle of collected data.

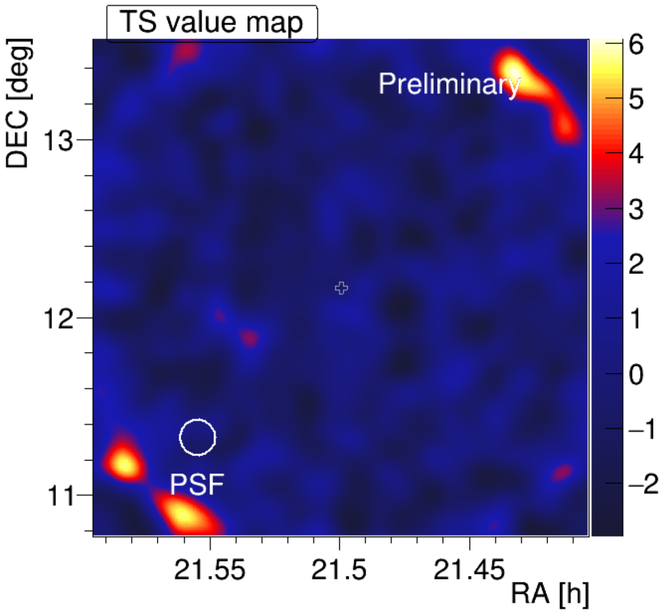

Figure 5.24: The significance sky-map which is centered on M15, after 138.04 hours of MAGIC stereoscopic observations and LE cuts. The color scale represents the test statistic value in σ-scale.

5.5 Cross section Upper limits

In this section I show the results on the thermal averaged cross-section ($\langle\sigma v\rangle$) for DM particles annihilating into different SM particles pairs.

The analysis is performed on self-annihilation DM particles into channels $b\bar{b}$, $\tau^+\tau^-$, $\mu^+\mu^-$ and W^+W^-, the most common scenarios for annihilating DM models, considering 100% branching ratio into four different channels.

I computed one-sided, 95% confidence level upper limits to $\langle\sigma v\rangle$ by numerically solving the equation $-2ln\lambda(\langle\sigma v\rangle|\mathcal{D}) = 2.71$ which is explained in the section §4.3, with the restriction that $\langle\sigma v\rangle$ must be inside the physical region (≥ 0). In the first analysis the maximal hypothesis that all the missing matter is made up by dark matter had obviously to be rejected. This speculation leads to obtain meaningless limits because they are too low, around 10^2 times lower than the thermal relic cross section value. Instead, it is necessary to assume that the dark matter is only a small amount of the missing matter inside the core. In absence of new models to compute the possible amount of dark matter, we have considered the relationship between the densities in other works. In this way we have supposed that dark matter makes up only 1% of the entire missing mass. Under this idea the J-factor decreases and it is equal to 4.27×10^{19} GeV^2 cm^{-5} (in a log-scale the value is 19.63). Every parameter,

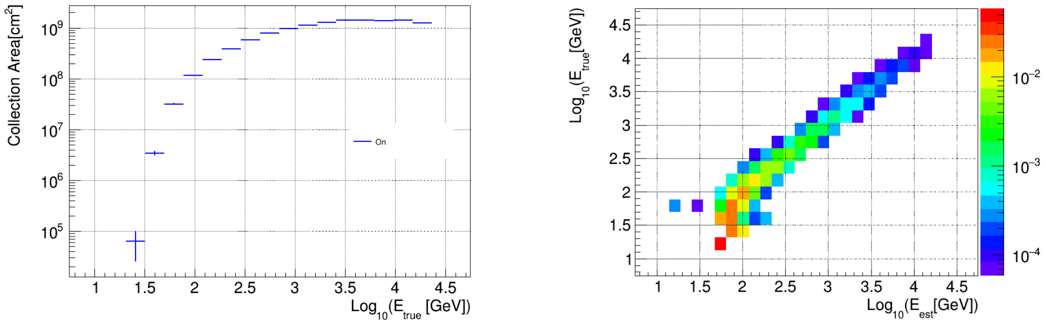

(a) Collection area

(b) Migration matrix

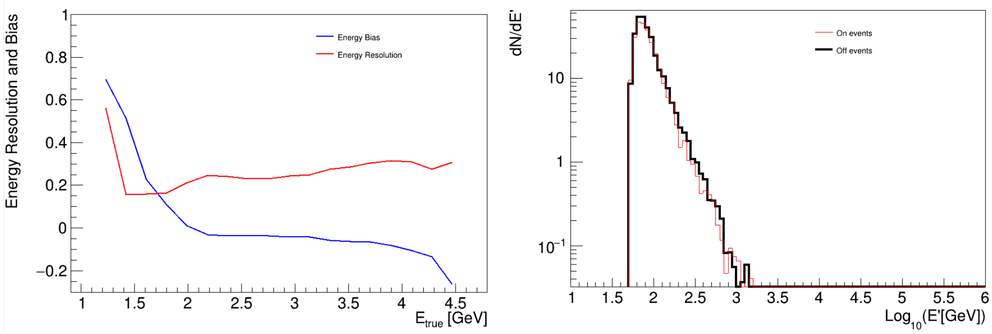

(c) Energy resolution and bias

(d) Events

Figure 5.25: For every wobble position different parameters are computed and will be used inside the full likelihood method. For example in the figure are shown the collection area, migration matrix, energy bias and resolution and the dN/dE regarding the first wobble position.

excluding the J-factor, inside the equation 4.13 is computed in independent way for each wobble position and for each cycle of observation.

The results are reported in the figure 5.26 where it is shown the upper limit on $\langle \sigma v \rangle$ obtained with ~ 138 h of data taken at low Zenith angle, with J like a fixed parameter.

In the plot it is shown also limit which is obtained under the null hypothesis H_0 (absence of dark matter) and it is reported in dashed line. Also the 68% and 95% confidence bands under the null hypothesis are reported. These are estimated from the distributions of limits obtained by applying our analysis to 300 independent H_0 realizations: 300 fast Monte Carlo simulations of background events, with the same statistics and probability density function in those periods of data set.

As can be seen in figure 5.26, our limits are consistent with the null hypothesis for all considered DM models. The lowest value as a function of the particle masses for each channel computed on real data is reported in table 5.5.

Channel	m_χ [GeV]	$\langle\sigma v\rangle$ [cm^3/s]
$b\bar{b}$	2000	3.07×10^{-24}
$\mu^+\mu^-$	400	1.82×10^{-24}
$\tau^+\tau^-$	600	4.62×10^{-25}
W^+W^-	800	1.70×10^{-24}

Table 5.5: The results of the $\langle\sigma v\rangle^{UL}$ computed for each annihilation channel of DM particles.

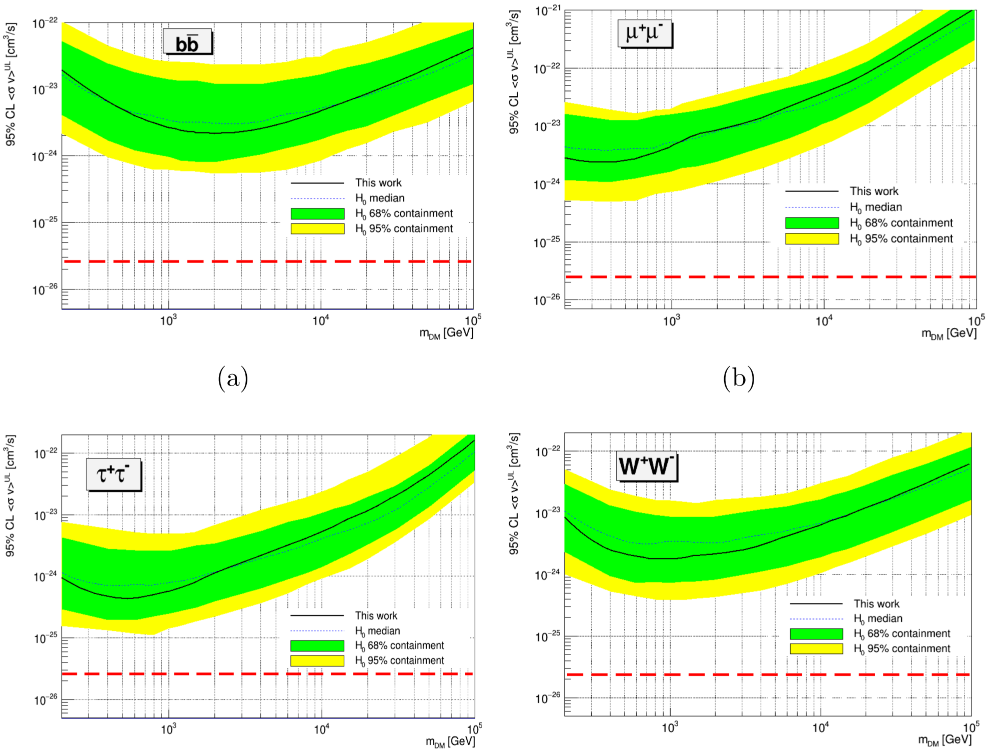

(a) (b)

(c) (d)

Figure 5.26: 95% CL ULs on the DM annihilation cross section $\langle \sigma v \rangle$ as a function of the dark matter particle mass m_{DM} for four different annihilation channels: $b\bar{b}$ (upper left), $\mu^+\mu^-$ (upper right), $\tau^+\tau^-$ (bottom left), and W^+W^- (bottom right), from 138 h of good quality data from MAGIC observations of M15 GC under the hypothesis that the dark matter is only 1% of the missing matter. The J-factor is 19.63 ± 0.27 and it is used in the FL to calculate the limits. The observed (solid line) and the expected (dashed line) limits are shown together with the 1σ (green) and 2σ (yellow) bands computed after 300 simulations of the null hypothesis (no DM signal).

Chapter 6

Conclusion and future works

Results

Observations in the range of VHE γ-ray by Whipple [182] and H.E.S.S. [185] are the unique studies about the DM inside M15 so far. In both these studies the main issue was to determine the relative DM distribution in the cluster in order to be able to compute the J-factor.

Whipple dedicated 1.2 h of observation of M15 searching for signal from DM annihilation. In their model the initial distribution of the DM is described by an NFW profile and, subsequently, due to the adiabatic contraction, the DM is pressed towards the center.

H.E.S.S. observed M15 for 15.2 h at mean Zenith degree equal to 37.0°. The H.E.S.S. team considered the same initial profile and adiabatic contraction but also added an additional process that causes the amount of dark matter inside M15 to decrease. The estimation of the amount of DM in the cluster is done in two steps: in the first step the adiabatic contraction presses the DM towards the core increasing the density in the center, in the second step the dark matter particles are captured inside the stars and self-annihilate releasing energy and decreasing their concentration. Assuming the absence of a massive BH in the center of M15, H.E.S.S. reaches the limit $\langle \sigma v \rangle \sim 5 \times 10^{-24}$ cm^3 s^{-1} around $m_{DM} = 2$ TeV.

The MAGIC telescopes observed the GC M15 in 2015/2016, collecting 173 h of data at mean Zenith degree equal to 20.81°. I studied this data set and applying strong cuts, only $\sim$ 138 h of data are selected with quality enough for searching signal from annihilation DM particles.

The J-factor has been computed using recent data collected by the Hubble telescopes and the Canada–France–Hawaii Telescope. The new measurements on star velocities have given a better resolution on the star velocities located in the center and hence a better resolution on the estimate of M/L profile with respect to previous works.

As a mere starting point, I assumed that the M/L is completely due to the presence of DM in the core, a new way of calculating the J factor has been studied from these inputs. The obtained value of the J-factor is equal to 4.0×10^{23} GeV^2 cm^{-5}, around 5 orders of magnitude compared both with the results of Whipple §5.1 and H.E.S.S. §5.1.

The J-factor derives from two quantities which were estimate with a certain uncertainty, therefor also the J-factor is affected by errors. The propagation of the errors is not easy and for this reason I have used a Monte Carlo approach. Pairs of random numbers are extracted with a certain probability density function. The numbers are associated at new profiles both M/L and density matter and from their combination a new J-factor profile was computed. If this is done many times, the calculated values of the J-factor will be distributed around the mean value of the measure and spread out following the value of variance. After a great number of simulations, the results is $J \pm \sigma = (4.0503 \pm 2.2453) \times 10^{23}$ GeV^2 cm^{-5}. The mean value of the J-factor after a lot of extraction matches with the J-factor computed using the mean values of the measurements while the value of the variance is the same order of the other DM sources.

After the determination value of the astrophysical factor the next step of the work is to analyse the data set.

The standard data analysis reveals absence of γ-ray excess from DM particles so I have been computing the most stringent limits on the thermally-annihilation cross-section of WIMP DM particles annihilating into SM pairs $b\bar{b}$, $\tau^+\tau^-$, $\mu^+\mu^-$ and W^+W^-.

Excluding the possibility that all the missing matter is made up of dark matter, I assumed that if the amount of dark matter is 1% of the missing mass. With this assumption the value of the J factor is very close to the H.E.S.S. value. The constraints are computed using the Full Likelihood method and the estimated value of the J-factor, considering also 100% branching ratio into different SM particle pairs. Finally the results on the upper limits for each channel are: $\langle\sigma v\rangle_{b\bar{b}} = 3.07 \times 10^{-24}$ cm^3 s^{-1}, $\langle\sigma v\rangle_{\tau^+\tau^-} = 4.62 \times 10^{-25}$ cm^3 s^{-1}, $\langle\sigma v\rangle_{\mu^+\mu^-} = 1.82 \times 10^{-24}$ cm^3 s^{-1}, $\langle\sigma v\rangle_{W^+W^-} = 1.70 \times 10^{-24}$ cm^3 s^{-1}The upper limits shown in this work are of the same order of magnitude of H.E.S.S. upper limits, which is $\sim 5 \times 10^{-24}$ cm^3 s^{-1}, and consequently they are better of Whipple's result, which is 3.3×10^{-22} cm^3 s^{-1}.

Next work

In my analysis I assumed the absence of an IMBH located in the center of the GC, and I started under the most optimistic hypothesis: that all the missing mass is composed by DM particles. This assumption is very strong because we known that are present a population of stellar remnants and heavy dark objects inside the core, both contributing to the observed M/L. My results are similar to the results of H.E.S.S. which were found using a model of evolution where they took in consideration the interactions between dark matter and baryonic matter during the life of the globular cluster.

For this reason it is necessary to build a model of the distribution of DM inside the GC following the H.E.S.S. model and improving it with the most recent works. An important original contribution of my work is the Monte Carlo method to derive uncertainty on J-factor, that can be applied in general to any combination of density profile, mass to luminosity ratio and assumption on the DM content.

New studies conducted in the last years to measure the distribution of dark matter and its possible dynamics considering the presence of gas and stars, may offer new scenarios of dark matter evolution within M15.

Moliné et al [190] studied the internal structure of the subhaloes and used a different equation to describe the concentration parameter (c_{200}) of DM inside them. In the article the range of masses of subhaloes varied between 10^6 and 10^{11} h^{-1} $M_\odot$ and they showed how the concentration of subhaloes varies as a function of mass, maximum circular velocity and distance to the host halo centre. The equation which describe the $c_{200}(m_{200}, x_{sub})$ profile is different by the previous work conducted by Bullock et al [183] (which is used both in the Whipple and H.E.S.S. jobs) on haloes with masses in a range from 10^{11} to 10^{14} $M_\odot$. It is possible to use this new equation to evaluate the parameter c_{200} obtaining a new density profiles of simulated DM halos.

Both Moliné and Bullock fit their data with a NFW profile but the observation data from rotation curve of galaxies do not show the presence a cusp in the center. This disagreement between observation data and simulations could suggest that another way to model the amount of DM in the GC is possible using another density profile. Read et al [191] argued the transformation from cusp profile (NFW) to a core profile ($coreNFW$) due to stars formation in the center of the subhaloes [192]. In the article, the authors show that the cores fully form in less than 4 Gyr for the $M_{200} = 10^8$ $M_\odot$ while for mass below 10^7 $M_\odot$ the core is not created and the profile is very close to NFW profile[1].

---

[1] The authors suggest that there is a critical stellar mass at which core formation becomes impossible but the limit 10^7 $M_\odot$ which is shown in the article is due to the lower resolution of the simulations at this mass scale.

M15 is rich of stars and exotic components which are the result of the very high star density and therefore close interactions and near-collisions of stars occurring relatively often. It is plausible that the coreNFW profile can describe the configuration of the DM in this extreme environment of M15.

Both Whipple telescope and H.E.S.S. considered an adiabatic compression using the model proposed by Blumenthal et al [184] in which all the halo particles are positioned on circular orbits and predicts steeper inner profiles for initially NFW haloes than observed. This model has been revised by Selwood et al [193] using another approach: using the Yaung's method the authors studied the density of a dark matter halo that is compressed by the growth of a disk in its center.

In addition to various ways to improve the model of H.E.S.S. new kinematic measurements on the stars located in the center of the cluster are waited.

New measurements could reduce the error on M/L ratio and on the mass density radial profile; in addition could give us new constraints about the amount of dark objects inside the central region.

For example the *Multi Unit Spectroscopic Explorer (MUSE)* which is installed on Yepun (UT4), the fourth Unit Telescope of the Very Large Telescope at the Paranal Observatory, observed M15 in September 2018 and now the team has published their new results on the dynamic of the core [194]. Their next step will be used dynamical models to fit their kinematic data set to understand the internal dynamics of the cluster due to the presence of compact systems of stellar remnants, for example black hole binaries, and post core-collapse oscillations. Since M15 contains many evolved star types it is a current object of studies on RR Lyrae stars [195], on red giant branch (RGB) stars [196], on neutron stars and binary system composed by double neutron stars [2] [197]. It is probably that new studies on M15 on its internal dynamics, early evolution and dark objects, will be published shortly.

With the new data from internal dynamics and new dynamical models about the evolution of the amount of DM inside the GC, it will be possible to have a more accurate estimate of the J-factor, and this will allow us to obtain better limits on the self-annihilation of dark matter particles.

---

[2] PSR 2127 + 11C is the only known double system of neutron stars and it is located inside the core of M15

List of Figures

List of Tables

Bibliography

[1] Mark den Brok et al. "The central mass and mass-to-light profile of the Galactic globular cluster M15". In: *Monthly Notices of the Royal Astronomical Society* 438.1 (2014), pp. 487–493.

[2] Anthony M Brown et al. "Understanding the γ-ray emission from the globular cluster 47 Tuc: Evidence for dark matter?" In: *Physical Review D* 98.4 (2018), p. 041301.

[3] Elaine CFS Fortes et al. "What could be the observational signature of dark matter in globular clusters?" In: *Journal of Cosmology and Astroparticle Physics* 2020.08 (2020), p. 010.

[4] Jelena Aleksić et al. "Optimized dark matter searches in deep observations of Segue 1 with MAGIC". In: *Journal of Cosmology and Astroparticle Physics* 2014.02 (2014), p. 008.

[5] MAGIC collaboration et al. "Limits to dark matter annihilation cross-section from a combined analysis of MAGIC and Fermi-LAT observations of dwarf satellite galaxies". In: *Journal of Cosmology and Astroparticle Physics* 2016.02 (2016), p. 039.

[6] Max L Ahnen et al. "Indirect dark matter searches in the dwarf satellite galaxy Ursa Major II with the MAGIC Telescopes". In: *Journal of cosmology and astroparticle physics* 2018.03 (2018), p. 009.

[7] Victor A Acciari et al. "A search for dark matter in Triangulum II with the MAGIC telescopes". In: *Physics of the Dark Universe* 28 (2020), p. 100529.

[8] Kenath Arun, SB Gudennavar, and Ch Sivaram. “Dark matter, dark energy, and alternate models: A review”. In: *Advances in Space Research* 60.1 (2017), pp. 166–186.

[9] Jennifer M Gaskins. “A review of indirect searches for particle dark matter”. In: *Contemporary Physics* 57.4 (2016), pp. 496–525.

[10] Marc Schumann. “Direct detection of WIMP dark matter: concepts and status”. In: *Journal of Physics G: Nuclear and Particle Physics* 46.10 (2019), p. 103003.

[11] Felix Kahlhoefer. “Review of LHC dark matter searches”. In: *International Journal of Modern Physics A* 32.13 (2017), p. 1730006.

[12] Björn Penning. “The pursuit of dark matter at colliders—an overview”. In: *Journal of Physics G: Nuclear and Particle Physics* 45.6 (2018), p. 063001.

[13] Antonio Boveia and Caterina Doglioni. “Dark matter searches at colliders”. In: *Annual Review of Nuclear and Particle Science* 68 (2018), pp. 429–459.

[14] Fritz Zwicky. “Die rotverschiebung von extragalaktischen nebeln”. In: *Helvetica Physica Acta* 6 (1933), pp. 110–127.

[15] Gianfranco Bertone and Dan Hooper. “History of dark matter”. In: *Reviews of Modern Physics* 90.4 (2018), p. 045002.

[16] Gianfranco Bertone, Dan Hooper, and Joseph Silk. “Particle dark matter: Evidence, candidates and constraints”. In: *Physics reports* 405.5-6 (2005), pp. 279–390.

[17] Vera C. Rubin and Jr. Ford W. Kent. “Rotation of the Andromeda Nebula from a Spectroscopic Survey of Emission Regions”. In: 159 (Feb. 1970), p. 379. DOI: `10.1086/150317`.

[18] M. S. Roberts and R. N. Whitehurst. “The rotation curve and geometry of M31 at large galactocentric distances.” In: 201 (Oct. 1975), pp. 327–346. DOI: `10.1086/153889`.

[19] SS Gershtein and Ya B Zeldovich. “Rest mass of muonic neutrino and cosmology”. In: *Jetp Lett* 4.120-122 (1966), p. 1.

[20] S. D. M. White, C. S. Frenk, and M. Davis. “Clustering in a neutrino-dominated universe”. In: 274 (Nov. 1983), pp. L1–L5. DOI: `10.1086/184139`.

[21] Scott Dodelson and Lawrence M. Widrow. “Sterile neutrinos as dark matter”. In: *Phys. Rev. Lett.* 72 (1 Jan. 1994), pp. 17–20. DOI: `10.1103/PhysRevLett.72.17`. URL: `https://link.aps.org/doi/10.1103/PhysRevLett.72.17`.

[22] Heinz Pagels and Joel R Primack. “Supersymmetry, cosmology, and new physics at teraelectronvolt energies”. In: *Physical Review Letters* 48.4 (1982), p. 223.

[23] Kim Griest. “Cross sections, relic abundance, and detection rates for neutralino dark matter”. In: *Phys. Rev. D* 38 (8 Oct. 1988), pp. 2357–2375. DOI: `10.1103/PhysRevD.38.2357`. URL: `https://link.aps.org/doi/10.1103/PhysRevD.38.2357`.

[24] Jonathan L. Feng. “Supersymmetry and cosmology”. In: *Annals of Physics* 315.1 (2005). Special Issue, pp. 2–51. ISSN: 0003-4916. DOI: `https://doi.org/10.1016/j.aop.2004.09.014`. URL: `http://www.sciencedirect.com/science/article/pii/S0003491604001903`.

[25] R. D. Peccei and Helen R. Quinn. “Constraints imposed by CP conservation in the presence of pseudoparticles”. In: *Phys. Rev. D* 16 (6 Sept. 1977), pp. 1791–1797. DOI: `10.1103/PhysRevD.16.1791`. URL: `https://link.aps.org/doi/10.1103/PhysRevD.16.1791`.

[26] Christopher F McKee, Antonio Parravano, and David J Hollenbach. “Stars, gas, and dark matter in the solar neighborhood”. In: *The Astrophysical Journal* 814.1 (2015), p. 13.

[27] Jatan Buch, Shing Chau John Leung, and JiJi Fan. “Using Gaia DR2 to constrain local dark matter density and thin dark disk”. In: *Journal of Cosmology and Astroparticle Physics* 2019.04 (2019), p. 026.

[28] PF de Salas et al. “On the estimation of the local dark matter density using the rotation curve of the Milky Way”. In: *Journal of Cosmology and Astroparticle Physics* 2019.10 (2019), p. 037.

[29] Massimo Persic, Paolo Salucci, and Fulvio Stel. “The universal rotation curve of spiral galaxies—I. The dark matter connection”. In: *Monthly Notices of the Royal Astronomical Society* 281.1 (1996), pp. 27–47.

[30] Yoshiaki Sofue and Vera Rubin. “Rotation curves of spiral galaxies”. In: *Annual Review of Astronomy and Astrophysics* 39.1 (2001), pp. 137–174.

[31] Joshua D Simon and Marla Geha. “The kinematics of the ultra-faint Milky Way satellites: solving the missing satellite problem”. In: *The Astrophysical Journal* 670.1 (2007), p. 313.

[32] Ekaterina V Karukes and Paolo Salucci. “The universal rotation curve of dwarf disc galaxies”. In: *Monthly Notices of the Royal Astronomical Society* 465.4 (2017), pp. 4703–4722.

[33] G Mark Voit. “Tracing cosmic evolution with clusters of galaxies”. In: *Reviews of Modern Physics* 77.1 (2005), p. 207.

[34] SW Allen et al. “Cosmological constraints from the local X-ray luminosity function of the most X-ray-luminous galaxy clusters”. In: *Monthly Notices of the Royal Astronomical Society* 342.1 (2003), pp. 287–298.

[35] Volker Springel et al. “Populating a cluster of galaxies–I. Results at z= 0”. In: *Monthly Notices of the Royal Astronomical Society* 328.3 (2001), pp. 726–750.

[36] Jelena Aleksić et al. “MAGIC gamma-ray telescope observation of the perseus cluster of galaxies: Implications for cosmic rays, dark matter, and NGC 1275”. In: *The Astrophysical Journal* 710.1 (2010), p. 634.

[37] Joachim Wambsganss. “Gravitational lensing in astronomy”. In: *Living Reviews in Relativity* 1.1 (1998), p. 12.

[38] Léon VE Koopmans and Tommaso Treu. "The structure and dynamics of luminous and dark matter in the early-type lens galaxy of 0047–281 at z= 0.485". In: *The Astrophysical Journal* 583.2 (2003), p. 606.

[39] Sandor M Molnar. "Cluster Physics with Merging Galaxy Clusters". In: *Frontiers in Astronomy and Space Sciences* 2 (2016), p. 7.

[40] Chiara Mastropietro and Andreas Burkert. "Simulating the bullet cluster". In: *Monthly Notices of the Royal Astronomical Society* 389.2 (2008), pp. 967–988.

[41] John A Peacock. *Cosmological physics*. Cambridge university press, 1999.

[42] Georges Aad et al. "Observation of a new particle in the search for the Standard Model Higgs boson with the ATLAS detector at the LHC". In: *Physics Letters B* 716.1 (2012), pp. 1–29.

[43] Peter Coles and Francesco Lucchin. *Cosmology: The origin and evolution of cosmic structure*. John Wiley & Sons, 2003.

[44] Eiichiro Komatsu et al. "Seven-year wilkinson microwave anisotropy probe (WMAP*) observations: cosmological interpretation". In: *The Astrophysical Journal Supplement Series* 192.2 (2011), p. 18.

[45] Djuna Croon et al. "GUT Physics in the era of the LHC". In: *Frontiers in Physics* 7 (2019), p. 76.

[46] Savas Dimopoulos and David Sutter. "The Supersymmetric flavor problem". In: *Nuclear Physics B* 452.3 (1995), pp. 496–512.

[47] Andrei D Sakharov. "Violation of CP-invariance, C-asymmetry, and baryon asymmetry of the Universe". In: *In The Intermissions... Collected Works on Research into the Essentials of Theoretical Physics in Russian Federal Nuclear Center, Arzamas-16*. World Scientific, 1998, pp. 84–87.

[48] Antonio Riotto and Mark Trodden. "Recent progress in baryogenesis". In: *Annual Review of Nuclear and Particle Science* 49.1 (1999), pp. 35–75.

[49] Richard H Cyburt et al. “Big bang nucleosynthesis: Present status”. In: *Reviews of Modern Physics* 88.1 (2016), p. 015004.

[50] Peter AR Ade et al. “Planck 2013 results. XVI. Cosmological parameters”. In: *Astronomy & Astrophysics* 571 (2014), A16.

[51] DJ Fixsen. “The temperature of the cosmic microwave background”. In: *The Astrophysical Journal* 707.2 (2009), p. 916.

[52] CB Netterfield et al. “A measurement by BOOMERANG of multiple peaks in the angular power spectrum of the cosmic microwave background”. In: *The Astrophysical Journal* 571.2 (2002), p. 604.

[53] Laura Lopez-Honorez et al. “Constraints on dark matter annihilation from CMB observations before Planck”. In: *Journal of Cosmology and Astroparticle Physics* 2013.07 (2013), p. 046.

[54] KIM GRIEST. “The Search for the Dark Matter: WIMPs and MACHOs”. In: *Annals of the New York Academy of Sciences* 688.1 (1993), pp. 390–407.

[55] C. Alcock et al. “The MACHO Project: Microlensing Results from 5.7 Years of Large Magellanic Cloud Observations”. In: *The Astrophysical Journal* 542.1 (Oct. 2000), pp. 281–307. DOI: `10.1086/309512`. URL: `https://doi.org/10.1086/309512`.

[56] R Ansari et al. “Experimental limits on the contribution of sub-stellar and stellar objects to the galactic halo”. In: *Astronomy and Astrophysics-A&A* 314 (1995), pp. 94–103.

[57] Katherine Freese, DS Graff, and B Fields. *Limits on Stellar Objects as the Dark Matter of Our Halo: Nonbaryonic Dark Matter Seems to be Required*. Tech. rep. 1999.

[58] Jaiyul Yoo, Julio Chaname, and Andrew Gould. “The end of the MACHO era: limits on halo dark matter from stellar halo wide binaries”. In: *The Astrophysical Journal* 601.1 (2004), p. 311.

[59] Jonathan L Feng. "Dark matter candidates from particle physics and methods of detection". In: *Annual Review of Astronomy and Astrophysics* 48 (2010), pp. 495–545.

[60] Gerard Jungman, Marc Kamionkowski, and Kim Griest. "Supersymmetric dark matter". In: *Physics Reports* 267.5-6 (1996), pp. 195–373.

[61] Manuel Drees and Fazlollah Hajkarim. "Neutralino dark matter in scenarios with early matter domination". In: *Journal of High Energy Physics* 2018.12 (2018), pp. 1–28.

[62] Hsin-Chia Cheng, Konstantin T Matchev, and Martin Schmaltz. "Bosonic supersymmetry? Getting fooled at the CERN LHC". In: *Physical Review D* 66.5 (2002), p. 056006.

[63] Thomas Flacke et al. "Electroweak Kaluza-Klein dark matter". In: *Journal of High Energy Physics* 2017.4 (2017), p. 41.

[64] Hsin-Chia Cheng, Jonathan L Feng, and Konstantin T Matchev. "Kaluza-Klein dark matter". In: *Physical review letters* 89.21 (2002), p. 211301.

[65] Toby Falk, Keith A Olive, and Mark Srednicki. "Heavy sneutrinos as dark matter". In: *Physics Letters B* 339.3 (1994), pp. 248–251.

[66] Alexey Boyarsky, Oleg Ruchayskiy, and Mikhail Shaposhnikov. "The role of sterile neutrinos in cosmology and astrophysics". In: *Annual Review of Nuclear and Particle Science* 59 (2009), pp. 191–214.

[67] Alexey Boyarsky et al. "Sterile neutrino dark matter". In: *Progress in Particle and Nuclear Physics* 104 (2019), pp. 1–45.

[68] Edward W Kolb, Daniel JH Chung, and Antonio Riotto. "WIMPzillas!" In: *AIP Conference Proceedings*. Vol. 484. 1. American Institute of Physics. 1999, pp. 91–105.

[69] Daniel JH Chung et al. "Gravitational production of superheavy dark matter". In: *Physical Review D* 64.4 (2001), p. 043503.

[70] Roberto D Peccei and Helen R Quinn. "CP conservation in the presence of pseudoparticles". In: *Physical Review Letters* 38.25 (1977), p. 1440.

[71] Martin J Rees and Dennis William Sciama. “Large-scale density inhomogeneities in the universe”. In: *Nature* 217.5128 (1968), pp. 511–516.

[72] James Hopwood Jeans. “I. The stability of a spherical nebula”. In: *Philosophical Transactions of the Royal Society of London. Series A, Containing Papers of a Mathematical or Physical Character* 199.312-320 (1902), pp. 1–53.

[73] William H. Press and Paul Schechter. “Formation of Galaxies and Clusters of Galaxies by Self-Similar Gravitational Condensation”. In: 187 (Feb. 1974), pp. 425–438. DOI: `10.1086/152650`.

[74] Volker Springel, Carlos S Frenk, and Simon DM White. “The large-scale structure of the Universe”. In: *nature* 440.7088 (2006), pp. 1137–1144.

[75] Michael Kuhlen, Mark Vogelsberger, and Raul Angulo. “Numerical simulations of the dark universe: State of the art and the next decade”. In: *Physics of the Dark Universe* 1.1-2 (2012), pp. 50–93.

[76] Marc Davis et al. “The evolution of large-scale structure in a universe dominated by cold dark matter”. In: *The Astrophysical Journal* 292 (1985), pp. 371–394.

[77] Ricardo A Flores and Joel R Primack. “Observational and theoretical constraints on singular dark matter halos”. In: *arXiv preprint astro-ph/9402004* (1994).

[78] Julio F Navarro, Carlos S Frenk, and Simon DM White. “A universal density profile from hierarchical clustering”. In: *The Astrophysical Journal* 490.2 (1997), p. 493.

[79] Ben Moore et al. “Dark matter substructure within galactic halos”. In: *The Astrophysical Journal Letters* 524.1 (1999), p. L19.

[80] Anatoly Klypin et al. “Where are the missing galactic satellites?” In: *The Astrophysical Journal* 522.1 (1999), p. 82.

[81] David H Weinberg et al. “Cold dark matter: controversies on small scales”. In: *Proceedings of the National Academy of Sciences* 112.40 (2015), pp. 12249–12255.

[82] James S Bullock and Michael Boylan-Kolchin. "Small-scale challenges to the Λ CDM paradigm". In: *Annual Review of Astronomy and Astrophysics* 55 (2017), pp. 343–387.

[83] Julio F Navarro et al. "The diversity and similarity of simulated cold dark matter haloes". In: *Monthly Notices of the Royal Astronomical Society* 402.1 (2010), pp. 21–34.

[84] Jesús Zavala and Carlos S Frenk. "Dark matter haloes and subhaloes". In: *Galaxies* 7.4 (2019), p. 81.

[85] Volker Springel et al. "The Aquarius Project: the subhaloes of galactic haloes". In: *Monthly Notices of the Royal Astronomical Society* 391.4 (2008), pp. 1685–1711.

[86] Raffaele Gratton et al. "What is a globular cluster? An observational perspective". In: *The Astronomy and Astrophysics Review* 27.1 (2019), pp. 1–136.

[87] Michael A Beasley. "Globular cluster systems and galaxy formation". In: *Reviews in Frontiers of Modern Astrophysics*. Springer, 2020, pp. 245–277.

[88] Georges Meylan et al. "Central velocity dispersion in the globular cluster omega Centauri." In: *Astronomy and Astrophysics* 303 (1995), p. 761.

[89] Richard T Inman and Bruce W Carney. "AM-4-The poorest globular cluster?" In: *The Astronomical Journal* 93 (1987), pp. 1166–1171.

[90] Harlow Shapley and Helen B Sawyer. "A Classification of Globular Clusters". In: *Harvard College Observatory Bulletin* 849 (1927), pp. 11–14.

[91] Eugenio Carretta et al. "Distances, ages, and epoch of formation of globular clusters". In: *The Astrophysical Journal* 533.1 (2000), p. 215.

[92] H Baumgardt et al. "Mean proper motions, space orbits, and velocity dispersion profiles of Galactic globular clusters derived from Gaia DR2 data". In: *Monthly Notices of the Royal Astronomical Society* 482.4 (2019), pp. 5138–5155.

[93] Ivan King. “The structure of star clusters. I. an empirical density law”. In: *The Astronomical Journal* 67 (1962), p. 471.

[94] BA Cook et al. “The information content of stellar halos: stellar population gradients and accretion histories in early-type illustris galaxies”. In: *The Astrophysical Journal* 833.2 (2016), p. 158.

[95] Duncan A Forbes and Rhea-Silvia Remus. “Metallicity gradients in the globular cluster systems of early-type galaxies: in situ and accreted components?” In: *Monthly Notices of the Royal Astronomical Society* 479.4 (2018), pp. 4760–4769.

[96] Karl Gebhardt and Markus Kissler-Patig. “Globular cluster systems. I. V- I color distributions”. In: *The Astronomical Journal* 118.4 (1999), p. 1526.

[97] Marta Reina-Campos and JM Kruijssen. “A unified model for the maximum mass scales of molecular clouds, stellar clusters and high-redshift clumps”. In: *Monthly Notices of the Royal Astronomical Society* 469.2 (2017), pp. 1282–1298.

[98] PJE Peebles and RH Dicke. “Origin of the globular star clusters”. In: *The Astrophysical Journal* 154 (1968), p. 891.

[99] Peter Creasey et al. “Globular clusters formed within dark haloes I: present-day abundance, distribution, and kinematics”. In: *Monthly Notices of the Royal Astronomical Society* 482.1 (2019), pp. 219–230.

[100] Smadar Naoz and Ramesh Narayan. “Globular clusters and dark satellite galaxies through the stream velocity”. In: *The Astrophysical Journal Letters* 791.1 (2014), p. L8.

[101] BF Griffen et al. “Globular cluster formation within the Aquarius simulation”. In: *Monthly Notices of the Royal Astronomical Society* 405.1 (2010), pp. 375–386.

[102] Jeremy J Webb et al. “Modelling the effects of dark matter substructure on globular cluster evolution with the tidal approximation”. In: *Monthly Notices of the Royal Astronomical Society* 488.4 (2019), pp. 5748–5762.

[103] M Sten Delos. “Tidal evolution of dark matter annihilation rates in subhalos”. In: *Physical Review D* 100.6 (2019), p. 063505.

[104] Jean P Brodie and Jay Strader. “Extragalactic globular clusters and galaxy formation”. In: *Annu. Rev. Astron. Astrophys.* 44 (2006), pp. 193–267.

[105] Alan P Lightman and Stuart L Shapiro. “The dynamical evolution of globular clusters”. In: *Reviews of Modern Physics* 50.2 (1978), p. 437.

[106] Lyman Spitzer Jr and Michael H Hart. “Random gravitational encounters and the evolution of spherical systems. II. Models”. In: *The Astrophysical Journal* 166 (1971), p. 483.

[107] M Hénon. “L’évolution initiale d’un amas sphérique”. In: *Annales d’Astrophysique.* Vol. 27. 1964, p. 83.

[108] Donald Lynden-Bell. “Statistical mechanics of violent relaxation in stellar systems”. In: *Monthly Notices of the Royal Astronomical Society* 136 (1967), p. 101.

[109] John N Bahcall, Tsvi Piran, and Steven Weinberg. *Dark matter in the universe.* World Scientific, 2004.

[110] Sourav Chatterjee et al. “Understanding the dynamical state of globular clusters: core-collapsed versus non-core-collapsed”. In: *Monthly Notices of the Royal Astronomical Society* 429.4 (2013), pp. 2881–2893.

[111] Thomas J Maccarone et al. “A black hole in a globular cluster”. In: *Nature* 445.7124 (2007), pp. 183–185.

[112] Paolo Gondolo and Joseph Silk. “Dark matter annihilation at the galactic center”. In: *Physical Review Letters* 83.9 (1999), p. 1719.

[113] S Djorgovski and Ivan R King. “A preliminary survey of collapsed cores in globular clusters”. In: *The Astrophysical Journal* 305 (1986), pp. L61–L65.

[114] Patrick R Durrell and William E Harris. “A color-magnitude study of the globular cluster M15”. In: *The Astronomical Journal* 105 (1993), pp. 1420–1440.

[115] Roeland P Van der Marel and Jay Anderson. "New limits on an intermediate-mass black hole in Omega Centauri. II. Dynamical models". In: *The Astrophysical Journal* 710.2 (2010), p. 1063.

[116] BBP Perera et al. "Evidence for an intermediate-mass black hole in the globular cluster NGC 6624". In: *Monthly Notices of the Royal Astronomical Society* 468.2 (2017), pp. 2114–2127.

[117] Bülent Kızıltan, Holger Baumgardt, and Abraham Loeb. "An intermediate-mass black hole in the centre of the globular cluster 47 Tucanae". In: *Nature* 542.7640 (2017), pp. 203–205.

[118] Joris Gerssen et al. "Hubble Space Telescope evidence for an intermediate-mass black hole in the globular cluster M15. II. Kinematic analysis and dynamical modeling". In: *The Astronomical Journal* 124.6 (2002), p. 3270.

[119] Remco van den Bosch et al. "The dynamical mass-to-light ratio profile and distance of the globular cluster M15". In: *The Astrophysical Journal* 641.2 (2006), p. 852.

[120] Martin Schwarzschild. "A numerical model for a triaxial stellar system in dynamical equilibrium". In: *The Astrophysical Journal* 232 (1979), pp. 236–247.

[121] Laura L Watkins et al. "Discrete dynamical models of ω Centauri". In: *Monthly Notices of the Royal Astronomical Society* 436.3 (2013), pp. 2598–2615.

[122] Holger Baumgardt et al. "On the central structure of M15". In: *The Astrophysical Journal Letters* 582.1 (2002), p. L21.

[123] Franz Kirsten et al. "Precision astrometry of pulsars and other compact radio sources in the globular cluster M15". In: *Astronomy & Astrophysics* 565 (2014), A43.

[124] Fabio Acero et al. "Fermi large area telescope third source catalog". In: *The Astrophysical Journal Supplement Series* 218.2 (2015), p. 23.

[125] PF Zhang et al. “Detection of gamma-ray emission from globular clusters M15, NGC 6397, 5904, 6218 and 6139 with Fermi-LAT”. In: *Monthly Notices of the Royal Astronomical Society* 459.1 (2016), pp. 99–107.

[126] MAGIC Collaboration et al. “Deep observations of the globular cluster M15 with the MAGIC telescopes”. In: *Monthly Notices of the Royal Astronomical Society* 484.2 (2019), pp. 2876–2885.

[127] W. Bednarek, J. Sitarek, and T. Sobczak. “TeV gamma-ray emission initiated by the population or individual millisecond pulsars within globular clusters”. In: *Monthly Notices of the Royal Astronomical Society* 458.1 (Feb. 2016), pp. 1083–1095. ISSN: 0035-8711. DOI: `10.1093/mnras/stw367`. eprint: `https://academic.oup.com/mnras/article-pdf/458/1/1083/8181858/stw367.pdf`. URL: `https://doi.org/10.1093/mnras/stw367`.

[128] Victor Hess. “On the observations of the penetrating radiation during seven balloon flights”. In: *arXiv preprint arXiv:1808.02927* (2018).

[129] BP Abbott et al. “LIGO Scientific Collaboration and Virgo Collaboration (2016) Directly comparing GW150914 with numerical solutions of Einstein’s equations for binary black hole coalescence. Physical Review D, 94 (6). ISSN 1550-2368, http://dx. doi. org/10.1103/PhysRevD. 94.064035”. In: *PHYSICAL REVIEW D Phys Rev D* 94 (2016), p. 064035.

[130] Maurizio Spurio. *Particles and astrophysics.* Springer, 2014.

[131] Malcolm S Longair. *High energy astrophysics.* Cambridge university press, 2010.

[132] AM Atoyan, FA Aharonian, and HJ Völk. “Electrons and positrons in the galactic cosmic rays”. In: *Physical Review D* 52.6 (1995), p. 3265.

[133] G Ambrosi et al. “Direct detection of a break in the teraelectronvolt cosmic-ray spectrum of electrons and positrons”. In: *Nature* 552.7683 (2017), p. 63.

[134] Hyesung Kang and Thomas W Jones. “Numerical studies of diffusive shock acceleration at spherical shocks”. In: *Astroparticle Physics* 25.4 (2006), pp. 246–258.

[135] Elena Amato. “The origin of galactic cosmic rays”. In: *International Journal of Modern Physics D* 23.07 (2014), p. 1430013.

[136] Anthony M Hillas. “The origin of ultra-high-energy cosmic rays”. In: *Annual review of astronomy and astrophysics* 22 (1984), pp. 425–444.

[137] AVi Olinto. “Ultra high energy cosmic rays: the theoretical challenge”. In: *Physics Reports* 333 (2000), pp. 329–348.

[138] James Matthews. “A Heitler model of extensive air showers”. In: *Astroparticle Physics* 22.5-6 (2005), pp. 387–397.

[139] CJ Cesarsky, Ji A Paul, and PG Shukla. “Bremsstrahlung gamma radiation and interstellar electron spectrum in the local interstellar medium”. In: *Astrophysics and Space Science* 59.1 (1978), pp. 73–83.

[140] George B Rybicki and Alan P Lightman. *Radiative processes in astrophysics*. John Wiley & Sons, 2008.

[141] SR Kelner, Felex A Aharonian, and VV Bugayov. “Energy spectra of gamma rays, electrons, and neutrinos produced at proton-proton interactions in the very high energy regime”. In: *Physical Review D* 74.3 (2006), p. 034018.

[142] Gabriele Ghisellini. “Beaming, synchrotron and inverse compton”. In: *INAF–Osservatorio Astronomico di Brera* (2008).

[143] Alessandro De Angelis and Mário João Martins Pimenta. *Introduction to particle and astroparticle physics: questions to the Universe*. Springer, 2015.

[144] Dan Hooper, Edward W Kolb, et al. “Pierre Auger data, photons, and top-down cosmic ray models”. In: *Physical Review D* 73.12 (2006), p. 123001.

[145] Piero Ullio and Lars Bergström. “Neutralino annihilation into a photon and a Z boson”. In: *Physical Review D* 57.3 (1998), p. 1962.

[146] Jason Kumar et al. “Gamma-ray signals from dark matter annihilation via charged mediators”. In: *Physical Review D* 94.1 (2016), p. 015022.

[147] Tracy R Slatyer. "TASI Lectures on Indirect Detection of Dark Matter". In: *arXiv e-prints* (2017), arXiv–1710.

[148] Felix A Aharonian. "Gamma rays from supernova remnants". In: *Astroparticle Physics* 43 (2013), pp. 71–80.

[149] Diego F Torres. "Order parameters for the high-energy spectra of pulsars". In: *Nature Astronomy* 2.3 (2018), pp. 247–256.

[150] Victor A Acciari et al. "Detection of the Geminga pulsar with MAGIC hints at a power-law tail emission beyond 15 GeV". In: *Astronomy & Astrophysics* 643 (2020), p. L14.

[151] Patrick Slane. "Pulsar Wind Nebulae". In: *Handbook of Supernovae* (2017), p. 2159.

[152] W Bednarek and M Bartosik. "Gamma-rays from the pulsar wind nebulae". In: *Astronomy & Astrophysics* 405.2 (2003), pp. 689–702.

[153] Guillaume Dubus. "Gamma-ray binaries and related systems". In: *The Astronomy and Astrophysics Review* 21.1 (2013), p. 64.

[154] AA Abdo et al. "Detection of gamma-ray emission from the starburst galaxies M82 and NGC 253 with the Large Area Telescope on Fermi". In: *The Astrophysical Journal Letters* 709.2 (2010), p. L152.

[155] Fabio Acero et al. "Detection of gamma rays from a starburst galaxy". In: *Science* 326.5956 (2009), pp. 1080–1082.

[156] VA Acciari et al. "A connection between star formation activity and cosmic rays in the starburst galaxy M82". In: *Nature* 462.7274 (2009), p. 770.

[157] RICHARD L AMOROSO. "On the Possibility of Relativistic Shock-Wave Effects in Observations of Quasar Luminosity". In: ().

[158] UF Katz. "Cherenkov light imaging in astroparticle physics". In: *Nuclear Instruments and Methods in Physics Research Section A: Accelerators, Spectrometers, Detectors and Associated Equipment* 952 (2020), p. 161654.

[159] Walter Heitler. *The quantum theory of radiation*. Courier Corporation, 1984.

[160] Mathieu de Naurois and Daniel Mazin. “Ground-based detectors in very-high-energy gamma-ray astronomy”. In: *Comptes Rendus Physique* 16.6-7 (2015), pp. 610–627.

[161] A Michael Hillas. “Cerenkov light images of EAS produced by primary gamma”. In: *19th International Cosmic Ray Conference (ICRC19), Volume 3*. Vol. 3. 1985.

[162] Trevor C Weekes et al. “Observation of tev gamma-rays from the crab nebula using the atmospheric cherenkov imaging technique”. In: *Astrophysical Journal* 342 (1989), pp. 379–395.

[163] Michael Punch et al. “Detection of TeV photons from the active galaxy Markarian 421”. In: *nature* 358.6386 (1992), pp. 477–478.

[164] James Anthony Hinton, Hess Collaboration, et al. “The status of the HESS project”. In: *New Astronomy Reviews* 48.5-6 (2004), pp. 331–337.

[165] et al W. Hofmann. *The H.E.S.S. Telescopes*. Available on line. July 2012. URL: `https://www.mpi-hd.mpg.de/hfm/HESS`.

[166] J Holder et al. “Status of the VERITAS Observatory”. In: *AIP Conference Proceedings*. Vol. 1085. 1. American Institute of Physics. 2008, pp. 657–660.

[167] CTA consortium. *CTA-observatory*. Available on line. 2020. URL: `www.cta-observatory.org`.

[168] Jelena Aleksić et al. “The major upgrade of the MAGIC telescopes, Part I: The hardware improvements and the commissioning of the system”. In: *Astroparticle Physics* 72 (2016), pp. 61–75.

[169] D Borla Tridon et al. “Performance of the Camera of the MAGIC II Telescope”. In: *arXiv preprint arXiv:0906.5448* (2009).

[170] Rubén López Coto and Enrique Fernández Sánchez. *Very-high-energy-ray observations of pulsar wind nebulae and cataclysmic variable stars with MAGIC and development of trigger systems for IACTs.* Universitat Autònoma de Barcelona, 2015.

[171] Razmik Mirzoyan et al. "Absolute reflectance of a concave mirror used for astro-particle physics experiments". In: *Astroparticle Physics* 105 (2019), pp. 1–12.

[172] Adrian Biland et al. "The active mirror control of the MAGIC telescope". In: *arXiv preprint arXiv:0709.1574* (2007).

[173] Riccardo Paoletti et al. "The trigger system of the MAGIC telescope". In: *IEEE transactions on nuclear science* 54.2 (2007), pp. 404–409.

[174] Julian Sitarek et al. "Analysis techniques and performance of the Domino Ring Sampler version 4 based readout for the MAGIC telescopes". In: *Nuclear Instruments and Methods in Physics Research Section A: Accelerators, Spectrometers, Detectors and Associated Equipment* 723 (2013), pp. 109–120.

[175] Alessio Berti et al. "Search for High Energy emission from GRBs with MAGIC". In: *Proceedings of the International Astronomical Union* 12.S324 (2016), pp. 70–73.

[176] Christian Fruck et al. *A novel LIDAR-based Atmospheric Calibration Method for Improving the Data Analysis of MAGIC.* Tech. rep. 2014.

[177] Roberta Zanin et al. "MARS, the MAGIC analysis and reconstruction software". In: *Proc. of the 33st International Cosmic Ray Conference, Rio de Janeiro, Brasil.* Citeseer. 2013.

[178] J Albert et al. "Implementation of the random forest method for the imaging atmospheric Cherenkov telescope MAGIC". In: *Nuclear Instruments and Methods in Physics Research Section A: Accelerators, Spectrometers, Detectors and Associated Equipment* 588.3 (2008), pp. 424–432.

[179] RW Lessard et al. “A new analysis method for reconstructing the arrival direction of TeV gamma rays using a single imaging atmospheric Cherenkov telescope”. In: *Astroparticle Physics* 15.1 (2001), pp. 1–18.

[180] T-P Li and Y-Q Ma. “Analysis methods for results in gamma-ray astronomy”. In: *The Astrophysical Journal* 272 (1983), pp. 317–324.

[181] Jelena Aleksić, Javier Rico, and Manel Martınez. “Optimized analysis method for indirect dark matter searches with Imaging Air Cherenkov Telescopes”. In: *Journal of Cosmology and Astroparticle Physics* 2012.10 (2012), p. 032.

[182] M Wood et al. “A search for dark matter annihilation with the Whipple 10 m telescope”. In: *The Astrophysical Journal* 678.2 (2008), p. 594.

[183] James S Bullock et al. “Profiles of dark haloes: evolution, scatter and environment”. In: *Monthly Notices of the Royal Astronomical Society* 321.3 (2001), pp. 559–575.

[184] George R Blumenthal et al. “Contraction of dark matter galactic halos due to baryonic infall”. In: *The Astrophysical Journal* 301 (1986), pp. 27–34.

[185] A Abramowski et al. “HESS observations of the globular clusters NGC 6388 and M15 and search for a dark matter signal”. In: *The Astrophysical Journal* 735.1 (2011), p. 12.

[186] Karl Gebhardt et al. “Fabry-perot observations of globular clusters. III. M15”. In: *Astronomical Journal* 113.3 (1997), pp. 1026–1038.

[187] Masha Baryakhtar et al. “Dark kinetic heating of neutron stars and an infrared window on WIMPs, SIMPs, and pure Higgsinos”. In: *Physical review letters* 119.13 (2017), p. 131801.

[188] Gianfranco Bertone and Malcolm Fairbairn. “Compact stars as dark matter probes”. In: *Physical Review D* 77.4 (2008), p. 043515.

[189] J Palacio, D Navarro-Girones, and J Rico. “Pointing optimization for IACTs on indirect dark matter searches”. In: *Astroparticle Physics* 104 (2019), pp. 84–90.

[190] Ángeles Moliné et al. “Characterization of subhalo structural properties and implications for dark matter annihilation signals”. In: *Monthly Notices of the Royal Astronomical Society* 466.4 (2017), pp. 4974–4990.

[191] JI Read, O Agertz, and MLM Collins. “Dark matter cores all the way down”. In: *Monthly Notices of the Royal Astronomical Society* 459.3 (2016), pp. 2573–2590.

[192] Andrew Pontzen and Fabio Governato. “How supernova feedback turns dark matter cusps into cores”. In: *Monthly Notices of the Royal Astronomical Society* 421.4 (2012), pp. 3464–3471.

[193] JA Sellwood and Stacy S McGaugh. “The compression of dark matter halos by baryonic infall”. In: *The Astrophysical Journal* 634.1 (2005), p. 70.

[194] Christopher Usher et al. “MUSE narrow field mode observations of the central kinematics of M15”. In: *Monthly Notices of the Royal Astronomical Society* (2021).

[195] Andrew M Hoffman et al. “Periods and classifications of RR Lyrae stars in the globular cluster M15”. In: *Monthly Notices of the Royal Astronomical Society* 502.1 (2021), pp. 818–835.

[196] Evan N Kirby et al. “The Stars in M15 Were Born with the r-process”. In: *The Astrophysical Journal Letters* 891.1 (2020), p. L13.

[197] S Ye Claire et al. “Millisecond Pulsars and Black Holes in Globular Clusters”. In: *The Astrophysical Journal* 877.2 (2019), p. 122.